博士論文

Plasmonic channel structure for sensing and photodetection at telecommunication wavelengths

（プラズモニックチャネル構造によるセンシング・通信波長での光検出）

肖　紅彬

Plasmonic channel structure for sensing and photodetection at telecommunication wavelengths

（プラズモニックチャネル構造によるセンシング・通信波長での光検出）

肖　紅彬

Hongbin Xiao

Department of Mechanical Engineering

The University of Tokyo

Professor Hirofumi DAIGUJI

Professor Hitoshi TABATA

Associate Professor Junho CHOI

Associate Professor Takuo TANEMURA

Associate Professor Jean-Jacques DELAUNAY

August, 2020

Dissertation Advisor:
Associate Professor Jean-Jacques DELAUNAY

Submitted by:
Hongbin Xiao

Plasmonic channel structure for sensing and photodetection at telecommunication wavelengths

Abstract

Plasmonic nanostructures have received extensive attention due to their ability to increase the harvesting of incident light from free space and concentrate electromagnetic energy to nanoscale volumes through the excitation of surface plasmons (SPs). With these outstanding properties, plasmonic nanostructures have been widely used to enhance the performance of optoelectronic devices, such as photocatalysis devices, solar energy harvesting devices, lasing devices, and photodetectors. SPs-based photodetectors generally have higher external quantum efficiencies and responsivities than conventional photodetectors because of the enhanced light absorption and the ability to generate hot electrons through the nonradiative decay of SPs. Photodetectors incorporating hot electrons are also referred to as hot electron photodetectors. Photodetection based on hot electrons is attracting interest due to its capability of enabling photodetection at sub-bandgap energies of semiconductor materials. Si-based photodetectors incorporating hot electrons have emerged as one of the most widely studied devices used for near infrared (NIR) photodetection, including antennas, nanorods, nanowires, waveguides, metal gratings, and gratings with the deep trench cavities. Among them, the grating-based structures offer an efficient approach to realize strong light confinements by generating surface plasmon polaritons (SPPs), which results in a resonant photocurrent response with narrow bandwidth. However, most reported Si-based NIR photodetectors have low responsivity and broad bandwidths with responsivities that change slowly with the target wavelength, limiting their practicality as spectrally selective photodetectors.

In this thesis, a Si channel-separated parallel grating structure that exhibits the spectrally selective photodetection in the C-band (1530-1565 nm) is first investigated. The structure efficiently guides and confines incident light at the corners of the Au slabs and the Au/Si interface through exciting the SPP mode. The electric field is strongly enhanced at the Au/Si interface due to the presence of SPP mode, which ensures the generated hot electrons have a low thermalization loss and high transport efficiency across the Au/Si barrier. By taking advantages of the plasmon induced hot electrons, the structure overcomes the native limitations from the bandgap of semiconductors and achieves sub-bandgap photodetection with relative high responsivity and large variation in the C-band. The measured responsivity for the structure with a period of 850 nm shows the spectral selectivity in the C-band and the peak responsivity reaches 72.5 nA/mW at the resonant wavelength of 1538 nm and bias voltage of 1.0 V. The measured responsivity for the structure with a period of 840 nm steadily decreases across the C-band as the wavelength increases. The responsivity drops from 64.5 nA/mW at 1530 nm to 19.0 nA/mW at 1565 nm, representing a variation of 70.5% over the C-band. The measured dark current is smaller than 10 nA at the bias voltage of 1 V. The narrowband, ease of tuning the resonant wavelength, and spectral selectivity of the device not only help bridge the gap between the optical and electrical systems for photodetection but are also beneficial in other potential applications, such as sensing, imaging, and communications systems. Since the proposed structure shows a strong field enhancement at the metal/air interface due to the channel enhanced surface plasmon polariton (SPP) mode, the dip of the reflectance spectrum of the structure is highly sensitive to the minute variation of the refractive index of the surrounding medium and this enables it to be a refractive index sensor. The measured sensitivity of the structure reaches a value as high as 967 nm/refractive index unit (RIU) with the figure of merit (FOM) approaching 60, which are higher than most reported refractive index sensors with plasmonic nanostructures. Additionally, the resonant wavelength of the structure is demonstrated to be readily tuned through changing the Si channel width or the structure period, so that a wider resonant wavelength range can be included for practical applications.

To further increase the responsivity of the Si channel-separated parallel grating structure, the Au grating is changed from the traditionally parallel structure to an interdigitated structure that are separated by U-shaped Si channels. For distinguish purpose, the interdigitated structure is named after Si channel-separated interdigitated grating structure. Since the cross sections of the two structures are the same, the absorptance and electric field distribution in the two structures are the same. The absorptance spectrum of the structure shows a sharp peak with a modulation of 0.81 at the resonant wavelength and the full width at half-maximum (FWHM) is as small as 23 nm. The photocurrent response of the structure reveals a remarkable improvement. The measured responsivity reaches 804 nA/mW at the resonant wavelength of 1550 nm and the bias voltage of 0.08 V, which is 11 times of that of the Si channel-separated parallel grating structure and shows a competitive performance with respect to previously reported Si-based NIR photodetectors. The measured signal to dark current ratio reaches 400 for the bias voltage of 0.08 V, which enables the structure to be an eligible NIR photodetector. Apart from this, a theoretical model is also conducted to evaluate the photocurrent response under light irradiation regarding the optical and electrical properties of the structure. According to the model, the theoretical calculation for the structure reproduces the spectral dependence of responsivity and exhibits the same spectral selectivity with the experiment in the C-band. Additionally, through changing the component material and structure dimensions, these grating-based channel structures are promising for achieving photodetection in the middle infrared (MIR) and even terahertz (THz) ranges.

We also propose a distributed Bragg reflector (DBR)-film structure and a grating-on-DBR structure in this thesis. The DBR-film structure achieves a high absorptance (0.83) at the resonant wavelength (1547 nm). The generation of hot electrons is enhanced by the excitation of Tamm plasmons (TPs) at the metal/DBR interface, facilitating the photocurrent response. The grating-on-DBR structure further increases the absorptance and shows a larger modulation compared with the DBR-film structure and Si-based Au grating structure. The electric field in this structure is strongly enhanced at the metal/DBR interface, which is likely originating from the coupling of FP resonance and TP resonance due to the grating-on-DBR mode. Due to the strong field enhancement at the interface, the generation of hot electrons is

further facilitated and a large photocurrent is produced. The structure also exhibits a narrowband and high responsivity in the NIR, which opens a new way for the TPs based hot electron photodetectors.

Acknowledgements

I am very pleased to take this opportunity to give my thanks to all of those who have supported, helped, guided and motivated me throughout my academic studies and everyday lives in the past years from the bottom of my heart.

First and foremost, I want to thank all of my family members, who have always supported me and helped me but ask for nothing in return. They always encourage and motivate me to achieve greater feats throughout the past years. Without their financial and moral support, it is impossible for me to study overseas, especially in Japan where the tuition fees and living expenses are much higher than most of the foreign countries. I would like to thank my father Shuiqiao Xiao, who always complains about me and my elder sister in the beginning but still supports us in the last. He is always serious to our family members but we both know he loves us deeply, and he shoulders all the responsivities as a filial son, a good father and a devoted husband. To my mother, Qiaorong Zhou, I want to say thank you for always believing in me and always giving me unconditional support whenever I need. You are so brave to share the heavy family burden together with my father during the past years. You did the heavy and boring manual labor in the factory in the daytime and did the housework after work every day. You are so toilsome everyday but you never complain to us and you always keep a smile on your ageing but still beautiful face. During the tough time in Japan, speaking to you has always helped me regain confidence and motivation to keep on moving forward. The warm greetings and career advice from my elder sister, Qin Xiao, has been invaluable for my studies and everyday life. Throughout the past period, she has guided me with her valuable experience and always gives me the considerate suggestions.

I could not successfully finish my Ph.D. studies without the valuable guidance and support from my respectable supervisor, Prof. Jean-Jacques Delaunay. I would like to give my greatest respect to Prof. Delaunay for giving me the valuable chance to join his wonderful research group, where I can learn the knowledge about micro/nano fabrications and silicon and photonics devices, and conduct my research in a nice and friendly environment. I also

appreciate the academic funding that he provided me to conduct my experiments. I could not get the financial support from SEUT in the first year and China Scholarship Council (CSC) in the next two years without his great assistance, which I should also give my greatest respect and thanks to him. I have a very limited knowledge on light science in the beginning and I have no ideas how to process my research in the middle, it was him who carefully and patiently helped me overcome these problems. I made mistakes frequently in the experiment and I even brought troubles to our lab in the first year, but he never lost hopes on me. He is like the godfather of all our lab members.

In addition to the support from Prof. Delaunay, I would also like to acknowledge many other people at the University of Tokyo that have helped me and made friends with me. First, I would like to give a special thanks to assistant Prof. Ya-Lun Ho, who has not only helped me in the research but also in everyday life. He taught me how to read literatures, how to make a report, how to do experiment and how to write papers and thesis. He is such a kind, helpful, patient and respectable guy that everyone in our lab respect him. I would also like to thank Dr. J. Kenji Clark, Dr. Jiaqi Zhang, Dr. Qi Cao, Dr. Jun Yu and Mr. Chih-Zong Deng for their assistances in teaching me how to use various pieces of experimental equipment throughout my Ph.D. studies. I also thank the accompany of my good friends Sicong Chen, Shuo Li, Mohammad Hassan Mirfasih and Steven James Osma. I will never forget you and treasure our valuable friendship forever.

I would also like to thank the finical support from CSC and the scholarship council in The University of Tokyo that offers me the SEUT scholarship. Without their financial supports, I would absolutely fall in financial troubles to go on my studies in Japan.

Finally, I would like to thank The University of Tokyo. Thanks for accepting me and other foreign students to study here. Thanks for offering us such a wonderful place to do our research. I love you.

Table of Contents

Chapter 1 : Introduction

1.1 Hot electron photodetection

1.1.1 Basic theory for hot electron photodetection

Hot electron photodetector is the normal device that is used for achieving hot electron photodetection. For hot electron photodetector, the photocurrent is formed through the generation, transport and collection of hot electrons in plasmonic nanostructures, such as metal/semiconductor (M/S), metal/insulator/metal (M/I/M) and the derived architectures (M/S/M, M/I/Transparent Conducting Oxide (TCO), etc.). Hot electrons with energies higher than the M/S or M/I barrier height can cross the Schottky barrier and be injected into the semiconductor or insulator through an internal photoemission process after their generation in a metal, leading to a photocurrent which can be measured with an external circuit, as shown in figure 1.1(a) [1]. In 1931, Fowler made the earliest attempt to quantitatively describe the photon-induced emission of electrons in metals [2]. Later in 1958, the overall processes including the generation, transport and collection of hot electrons were clarified by Spicer using a continuous 3-step model [3, 4]. First, hot electrons are generated in the metallic layer through absorbing photons' energies. Next, a part of hot electrons reaches the M/S interface by diffusion before thermalization. Last, hot electrons with energies larger than the barrier height and specific momenta are injected into the semiconductor by internal photoemission. Therefore, the photoelectric conversion efficiency of hot electron photodetectors is dependent on the initial distribution of hot electrons, and the transport and collection efficiency of hot electrons. In Fowler's model, it is assumed that the generated hot electrons in the metallic layer have an isotropic momentum distribution and hot electrons can cross the Schottky barrier only if their momenta are within the escape cone of the semiconductor. The internal photoemission efficiency η is expresses as

$$\eta = \frac{(\hbar\omega - \varphi_{\mathrm{b}})^2}{4E_F\hbar\omega}, \tag{1}$$

where $\hbar$ represents the reduced Planck constant, ω represents the photon frequency, φ_{b} represents the barrier height and E_{F} represents the Fermi energy of the metal. The barrier height φ_{b} for the M/S junction can be expressed as $\varphi_{\mathrm{b}} = \varphi_{\mathrm{M}} - \chi_{\mathrm{s}}$, where φ_{M} represents the work function of the metal and χ_{S} represents the electron affinity of the semiconductor. Apart from φ_{M} and χ_{S}, the barrier height is influenced by the fabrication techniques. Table 1 shows the measured barrier heights for typical M/S junctions. A plenty of reported hot electron photodetectors have been demonstrated to follow Fowler's model [5-7]. However, the internal photoemission of hot electrons over the Schottky barrier is usually an inefficient process compared to the generation and separation of electron-hole pairs in semiconductors. The inefficient internal photoemission of hot electrons is mainly due to poor light absorption, broad energy distribution and isotropic momentum distribution of hot electrons [8]. A few years later, researchers found that surface plasmons (SPs) could potentially boost the internal photoemission efficiency by addressing these issues and offer an efficient method for hot electron generation and extraction [9]. In general, SPs exist in two forms. One is the propagating surface plasmon polaritons (SPPs) that are along planar interfaces. The other is the localized surface plasmon resonances (LSPRs) which are confined to the surface of nanoparticles. SPs can be damped easily. The plasmons begin to decay radiatively into photons or non-radiatively into hot electrons via intraband (in the conduction band) or interband (between other band, such as *d* band, and conduction band) transitions only after a short time [1,10–12], as shown in figure 1.1(b). The thermalization loss (energies are transferred to heat) of hot electrons occurs through electron-electron and electron-phonon collisions in the next. For most applications, the radiative decay of plasmons serves as a parasitic process which brings limitations to the performances of the devices [13]. On the contrary, the nonradiative plasmon decay can enhance the generation of photoexcited hot electrons and generate plasmon-induced hot electrons at high efficiencies due to the high-field concentrations and resonant scattering, which results in a large photocurrent. By deliberately engineering the plasmon mode of the structure, the momentum distribution of

hot electrons can also be amended. For example, since the absorption cross section of the plasmonic nanoparticles is much larger than the physical cross section [14], it yields a much more efficient generation of hot electrons in plasmonic nanoparticles than that in the bulk metal. Moreover, hot electrons generated in the plasmonic nanoparticles stay at a higher average energy compared to that in the bulk metals [15-18].

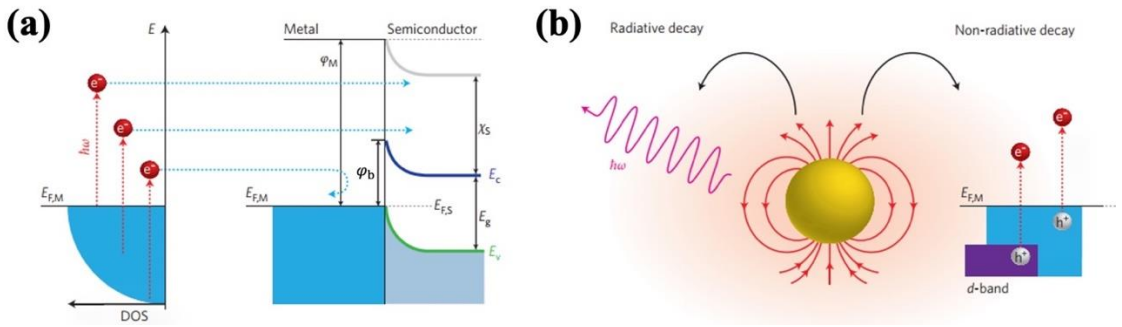

Figure 1.1 (a) The parabolic distribution of density of states (DOS) in the conduction band of plasmonic nanostructures and the energy band diagram for hot electron photodetectors with M/S architecture. Hot electrons are first generated in the metal. Then, hot electrons with energies higher than the Schottky barrier can be injected into the conduction band of the semiconductor and be collected. $E_{\mathrm{F,M}}$ represents the Fermi energy of the metal, $E_{\mathrm{F,S}}$ represents the Fermi energy of the semiconductor, φ_{M} represents the work function of the metal, φ_{b} represents the barrier height between metal and semiconductor, E_{V} represents the valence band of the semiconductor, E_{g} represents the bandgap of the semiconductor, E_{c} represents the conduction band of the semiconductor, and χ_{s} represents the electron affinity of the semiconductor. (b) The localized surface plasmons can decay radiatively into re-emitted photons and it can also decay non-radiatively into hot electrons. In noble metals, the non-radiative decay can occur through intraband excitations in the conduction band or through interband (such as the *d* band) excitations. Figures reproduced with permission from: ref. [1], © 2014 Springer Nature.

Table 1. The measured Schottky barrier height φ_{b} (eV) for typical M/S junctions, which are adapted from refs. [5, 19–27].

	Si	TiO_2	GaAs	Ge	CdSe	CdS
Au	0.80	1.00	1.05	0.59	0.70	0.80
Ag	0.83	0.91	1.03	0.54	0.43	0.56
Al	0.81	Ohmic	0.93	0.48	N/A	N/A
Ti	0.50	Ohmic	0.84	0.53	N/A	0.84
Cu	0.80	0.85	1.08	0.50	0.33	0.50
Pt	0.90	0.73	0.98	0.65	0.37	1.10
Cr	0.60	0.88	0.82	0.59	N/A	N/A

1.1.1.1 Generation of hot electrons

Electrons that are not in the thermal equilibrium with all atoms in the material are normally named as hot electrons. Hot electrons distributions can be fundamentally clarified by the Fermi function under an elevated effective temperature [28]. When light with energetic photons illuminates on the metallic structure, the absorbed photons will transfer their energies to the electrons in the metal, making their energies higher than that at the thermal equilibrium and generating hot electrons. In Chalabi's model [29], he uses an optical model to calculate the hot electron generation rate in the metal contacts in the M/I/M architecture. He first calculates the electric field distribution $E(\vec{r})$ in one periodic unit under light illumination with the photon energy of $\hbar\omega$ by using the Finite Difference Time Domain (FDTD) simulations. The local generation rate of hot electrons $G(\vec{r},\omega)$ is then calculated basing on the local ohmic loss $Q(\vec{r},\omega)$ in the metal as

$$G(\vec{r},\omega)=\frac{Q(\vec{r},\omega)}{\hbar\omega}=\frac{\frac{1}{2}\omega Im(\varepsilon)|E(\vec{r},\omega)|^2}{\hbar\omega}=\frac{Im(\varepsilon)|E(\vec{r},\omega)|^2}{2\hbar}, \quad (2)$$

where $Im(\varepsilon)$ represents the imaginary part of the permittivity of the metal. The generated hot electrons are assumed to have an isotropic momentum distribution and their energies equal to the absorbed photons' energies. The initial energy distribution of hot electrons is expressed with the combination of the electron density of state (EDOS) and the Fermi functions at the initial and final states:

$$D(E) = \frac{\rho(E - h\nu)f(E - h\nu)\rho(E)[1 - f(E)]}{\int_0^\infty \rho(E - h\nu)f(E - h\nu)\rho(E)[1 - f(E)]dE}, \quad (3)$$

where E represents the hot electron energy ($0 < E < h\nu$), $h\nu$ represents the photon energy, $\rho(E-h\nu)$ and $\rho(E)$ represents the EDOS at the initial and final energy levels, respectively, and $f(E-h\nu)$ and $f(E)$ are the Fermi distribution functions at the initial and final energy levels, respectively.

Hot electrons with energies higher than the work function of the material are emitted from the material via the photoelectric effect [30], producing a photocurrent. A small number of hot electrons can escape the metal if the energies of absorbed photons are higher than the work function of metal. Since the photon energy of visible and near infrared (NIR) light is lower than the work function of the metal, the generated hot electrons are kept in the metal. But the decay process occurs very fast through the electron-electron and electron-phonon collisions, which results in a thermalization loss [31]. The first step for the generation of hot electrons is the metal absorbs the photons. The hot electron generation efficiency is very low in planar metal due to the high reflection. SPs can result in rapidly increase of electric field near the metal and photon state density, and therefore improving the absorption efficiency. SPs in the metallic nanostructure decay in the form of radiatively emitting photons or generating hot electron-hole pairs through landau damping [32]. Landau damping is a pure process of quantum mechanics, and a plasma quantum generates an electron-hole pair in 1-100 fs. The distribution of hot electrons is dependent with plasmon's energy, the physical size, the density of state of the metal and the symmetry of the plasmon mode [33]. Since the momentum of photons and SPs can be neglected compared with the lattice momentum of electrons, only hot electron-hole pairs with lattice momentum of 0 can be generated through the direct decay of plasmons in the bulk material. It means that the direct excitation only occurs when photon's energy exceeds the threshold of the electron interband transitions in the metal. Most of hot electrons that are generated through the direct interband transitions originate from the top edge of *d*-band in noble metals, and their energies are all above the Fermi level. If the photon's energy is lower than the threshold of interband transition, the

absorption and emission of phonons can assist the excitation of density of states with different momenta, which is called phonon-assisted interband excitation. The nanostructures can also replace the phonons to excite hot carriers in the conduction band of metals, which is named geometry-assisted intraband excitation. The last excitation method is called multi-plasmon excitation, where hot carriers are generated through multi-plasmon decay under the ultra-strong laser illumination.

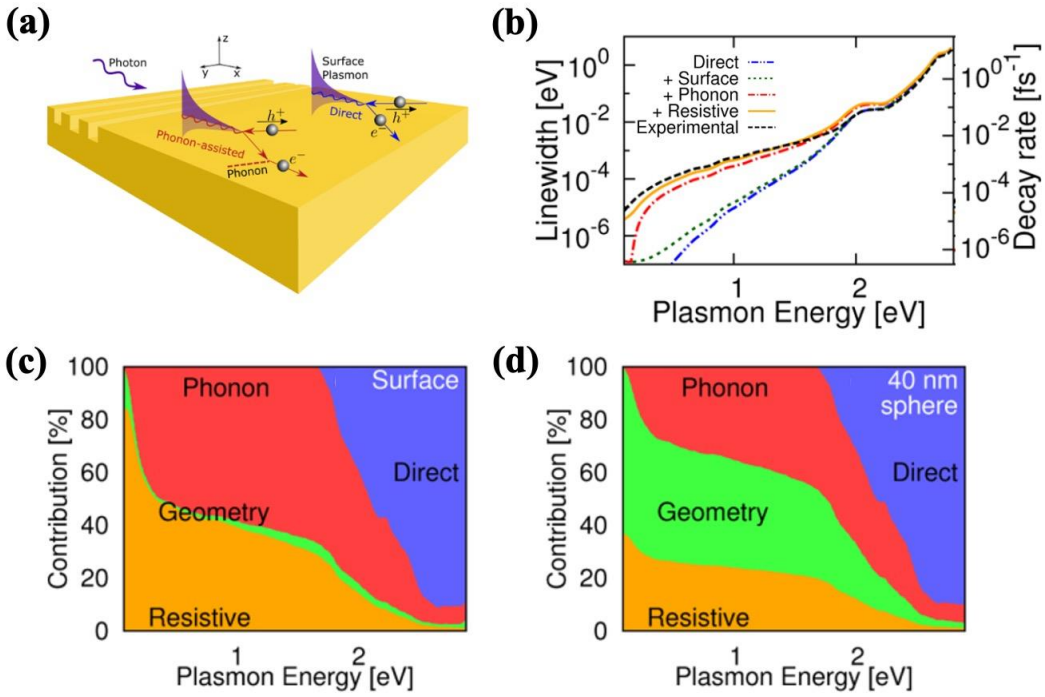

Figure 1.2 (a) Schematic diagram showing the excitation and decay of SPs. SPs that are excited in a grating or prism normally decay through direct transition or phonon-assisted transition to generate hot electrons and holes. (b) Comparison of calculated and experimental linewidth and plasmon decay rate in Au. The theoretical calculation results indicate cumulative contributions from direct transitions (Direct), which includes surface-assisted transition (+Surface), phonon-assisted transitions (+Phonon) and resistive loss (+Resistive). Contributions of resistive loss, geometry-assisted transition, phonon-assisted transition, and direct transition to absorption for (c) semi-infinite surface and (d) Au nanoparticle with a

diameter of 40 nm. Figures reproduced with permission from: ref. [33], © 2016, American Chemical Society.

Figure 1.2(a) gives the schematic for the excitation and decay of SPs through direct and phonon-assisted transitions for the generation of hot electrons and holes [34]. Figure 1.2(b) shows the comparison of calculated and experimental linewidth and plasmon decay rate in Au [34]. The theoretical calculation results show the cumulative contributions from direct transitions (Direct), which includes surface-assisted transition (Surface), phonon-assisted transition (Phonon), and resistive loss (Resistive). It is found that the direct transition dominates above the interband threshold (~1.6−1.8 eV) in Au and the sum of other contributions is smaller than 10%. Figures 1.2(c)-(d) compare the above contributions to the absorption for bulk gold surface and gold nanoparticle with a diameter of 40 nm [34]. It can be seen that the geometry-assisted intraband contribution can be neglected for the bulk gold surface, but it is comparable with respect to the phonon-assisted contribution and resistive contribution for the gold nanoparticle in the below-threshold range.

1.1.1.2 Transport and collection of hot electrons

Hot carriers generated in metals have an initial space and momentum distribution and they transport through the material by scattering through the interaction between electrons, phonons and defects in the metal. The scattering results in a thermalization loss to hot electrons and make their energies below the Fermi level. The energy of generated hot electrons in the metal $E_{k,\mathrm{M}}$ can be expressed as

$$E_{k,\mathrm{M}} = \frac{\hbar^2 k_{\mathrm{M}}^2}{2m}, \tag{4}$$

where k_{M} represents the hot electron momentum in the metal, and *m* represents the effective mass of a hot electron.

Hot electrons can transport in two ways, which are ballistic propagation and diffusion. Since the dimension of the metallic nanostructure gets close to the mean free path of hot

electrons in metal, both of ballistic propagation and diffusion occur in plasmonic nanostructures.

As for the collection process of the photoexcited hot electrons, it is clearly clarified in Scales's theory [35] and further improved in Chalabi's model [29]. As shown in Scales's model (figure 1.3(a)), the photodetection can occur via a 3-step internal photoemission process, which includes the photoexcitation, transport and emission in M/S architectures. Incident photons are absorbed by free electrons in the metal that are in a state below E_F, and then the electron energy is raised to a state above E_F and a free hole is left behind (photoexcitation step). if a hot electron obtains enough energy to cross the Schottky barrier and heads toward the M/S interface (transport step), then it can be injected into the semiconductor (emission step) and collected with an external circuit as a photocurrent. When a hot electron with the momentum of $\hbar k_M$ reaches the M/S interface at an angle of θ, as sketched in the left of figure. 1.3(b), the condition for the emission can be stated explicitly as

$$\frac{\left(\hbar k_{M,x}\right)^2}{2m} > \varphi_b, \tag{5}$$

where $k_{M,x}$ represents the electron's momentum in the x component. The escape momentum $(k_{M,\Omega})_x$ is then defined as

$$\left(k_{M,\Omega}\right)_x = k_M \cos\Omega = \frac{\sqrt{2m\varphi_b}}{\hbar}, \tag{6}$$

which constructs a k-space sphere with a radius of k_M representing the isotropic distribution of possible momenta for the hot electron. The right of figure 1.3(b) shows a cross-sectional sketch in the k_x–k_y plane bisecting the sphere. The rotation of the sketch around the k_x-axis yields a full k-space sphere and the escape cone is subtended by the solid angle Ω. Hot electrons that have a momentum orientation within the solid angle and satisfy $k_{M,x} > (k_{M,\Omega})_x$ can be emitted (i.e., emission is constrained to hot electrons that have a wavevector that terminates on the surface of the spherical cap highlighted in gray).

According to the exponential attenuation model and the assumption that the momentum is isotropous distributed, the probability ($P_1(E,\theta,z)$) for hot electrons reaching the M/S interface with a diffusion angle θ is evaluated by

$$\begin{cases} P_1(E,\theta,z) = \frac{1}{2}\exp\left(-\frac{d(z)}{l_{\mathrm{MFP}}(E)\cos\theta}\right), \text{if } -\frac{\pi}{2} < \theta < \frac{\pi}{2} \\ P_1(E,\theta,z) = 0, \text{otherwise} \end{cases} \tag{7}$$

where d represents the distance from the initial position of the hot electron to the M/S interface and $l_{\mathrm{MFP}}(E)$ represents the energy-dependent mean free path of the hot electron in the metal. The flux $N(E, \theta)$ of hot electrons that reaches the M/S interface with the angle of θ can be given by

$$N(E,\theta) = \int_0^{d_{\mathrm{Au}}} G(z) \times D(E) \times P_1(E,\theta,z)dz\,. \tag{8}$$

To accurately evaluate the injection efficiency of hot electrons, the reflection induced by the momentum mismatch at the M/S interface must be taken into consideration. The transmission probability (T) for hot electrons crossing the M/S interface can be expressed as

$$T = \frac{4\sqrt{\left(k_{\mathrm{M}}^2 - k_y^2\right)\left(k_{\mathrm{S}}^2 - k_y^2\right)}}{\left(\sqrt{k_{\mathrm{M}}^2 - k_y^2} + \sqrt{k_{\mathrm{S}}^2 - k_y^2}\right)^2}. \tag{9}$$

The energy $E_{k,\mathrm{S}}$ of hot electron that is injected into the semiconductor can be expressed as

$$E_{k,\mathrm{S}} = \frac{\hbar^2 k_S^2}{2m}, \tag{10}$$

where k_{s} is the hot electron momentum in the semiconductor. Since the M/S interface is invariant in the y direction, the momentum of hot electrons in this direction is reserved. Therefore, we can get the equation $k_{\mathrm{M},y} = k_{\mathrm{S},y} = k_y$. The injection efficiency $\eta_{\mathrm{inj}}(E)$ of hot electrons across the M/S junction can then be expressed as

$$\eta_{\mathrm{inj}}(E) = \frac{\int_0^{\Omega} 2\pi \sin\theta d\theta \times N(E,\theta) \times T}{\int_0^{\frac{\pi}{2}} 2\pi \sin\theta d\theta \times N(E,\theta)}. \tag{11}$$

Finally, the photocurrent density J can be expressed as

$$J = e \int_{\varphi_{\mathrm{b}}}^{\infty} \int_{-\frac{\pi}{2}}^{\frac{\pi}{2}} N(E,\theta) d\theta \times \eta_{\mathrm{inj}}(E) dE\,. \tag{12}$$

In 2014, Chalabi et al. uses a similar method to describe the photoemission of hot electrons across a M/I/M architecture with a consecutive 5-step process [29], as shown in figure 1.3(c). In the first step, hot electrons are generated in the metallic layers (e.g., top metallic layer) via photon absorption. According to the large momentum mismatch between the wave vectors of light and the generated hot electrons, it is assumed that the initial momenta of generated hot electrons are isotropic and their behaves are the same with free electrons [36,37]. In step 2, half of the generated hot electrons move towards the metal/oxide interface. While there is only a limited number of them can reach the interface without losing their energies through the inelastic collision. In this model, it is assumed that hot electrons that undergo the inelastic collision make no contributions to the formation of photocurrent. In step 3, hot electrons reaching the metal/oxide interface have a specific probability to be injected into the oxide if their energies are higher than the barrier height φ_{b}. Since the reflections naturally occur at the metal/oxide interface due to the large momentum mismatch for electrons in the metal and oxide, the injection probability is usually quite small [38,39]. Figure 1.3(d) shows the energy contours of hot electrons in the top metal and those just cross the Schottky barrier and reach the left side of the oxide [29]. The circles illustrate all the terminations of the allowed electron momenta at the energy E. These contours visualize and describe the ejection process of a hot electron into the oxide barrier. In step 4, hot electrons being injected into the oxide have a certain probability to propagate through the oxide without going through the inelastic collisions. Finally, hot electrons that avoid the reflections at the interface have a certain probability to cross the other side Schottky barrier and be collected by the opposing metallic layer.

The calculation for the photocurrent response of the M/I/M architecture is quite similar to that of the M/S architecture. The first two steps are completely the same (hot electrons' generation and transport to the M/S or M/I interface), but the next steps are a little different. In the following, the calculation for the photocurrent response of the M/I/M architecture is clearly clarified. The probability P_2 for hot electrons crossing the first M/I barrier can be given by

$$P_2 = \int_0^{K_{\mathrm{ol}}(E)} \frac{4\sqrt{(k_{\mathrm{t}}^2 - k_y^2)(k_{\mathrm{ol}}^2 - k_y^2)}}{\left(\sqrt{k_{\mathrm{t}}^2 - k_y^2} + \sqrt{k_{\mathrm{ol}}^2 - k_y^2}\right)^2} \frac{k_y}{2k_{\mathrm{t}}\sqrt{k_{\mathrm{t}}^2 - k_y^2}} dk_y, \tag{13}$$

where k_{t} represents the hot electron momentum in the top metallic layer, k_{ol} represents the hot electron momentum in the left side of the oxide, and K_{ol}(E) represents the maximum of k_{ol}.

After crossing the left M/I barrier, hot electrons will transport from one side to the other side of the oxide. The probability (P_3) for hot electrons transporting through the oxide without scattering and reaching the other side of the oxide is given by

$$P_3 = \exp\left(-\frac{t}{l_{\mathrm{MFP}}}\right), \tag{14}$$

where t represents the thickness of the oxide and l_{MFP} represents the mean free path of hot electrons in the oxide. The probability for hot electrons crossing the second M/I barrier and being collected by the bottom metal P_4 can be given by

$$P_4 = \int_0^{K_{\mathrm{or}}(E)} \frac{4\sqrt{(k_{\mathrm{b}}^2 - k_y^2)(k_{\mathrm{or}}^2 - k_y^2)}}{\left(\sqrt{k_{\mathrm{b}}^2 - k_y^2} + \sqrt{k_{\mathrm{or}}^2 - k_y^2}\right)^2} \frac{k_y}{2k_{\mathrm{or}}\sqrt{k_{\mathrm{or}}^2 - k_y^2}} dk_y, \tag{15}$$

where k_{b} represents the hot electron momentum in the bottom metallic layer, k_{or} represents the hot electron momentum in the right side of the oxide, and K_{or}(E) represents the maximum

of k_{or}. The total probability P_{tot} for hot electrons crossing the left M/S barrier, transporting through the oxide, crossing the right M/S barrier and being collected by the bottom metal is given by

$$P_{\text{tot}} = P_2 \times P_3 \times P_4. \tag{16}$$

The net photocurrent density J_{net} can be lastly calculated according to the forward ($N_{\text{top}\rightarrow\text{bot}}$) and backward ($N_{\text{bot}\rightarrow\text{top}}$) fluxes and the total probability

$$J_{\text{net}} = e\left(\int N_{\text{top}\rightarrow\text{bot}}(E) \times P_{\text{tot}} dE - \int N_{\text{bot}\rightarrow\text{top}}(E) \times P_{\text{tot}} dE\right). \tag{17}$$

Chalabi's model based on M/I/M architecture conceptually follows Scales's model that is developed for hot electron emission in the M/S architecture, but it adds additional physics with regard to electron reflections at the metal/oxide boundary [38,39].

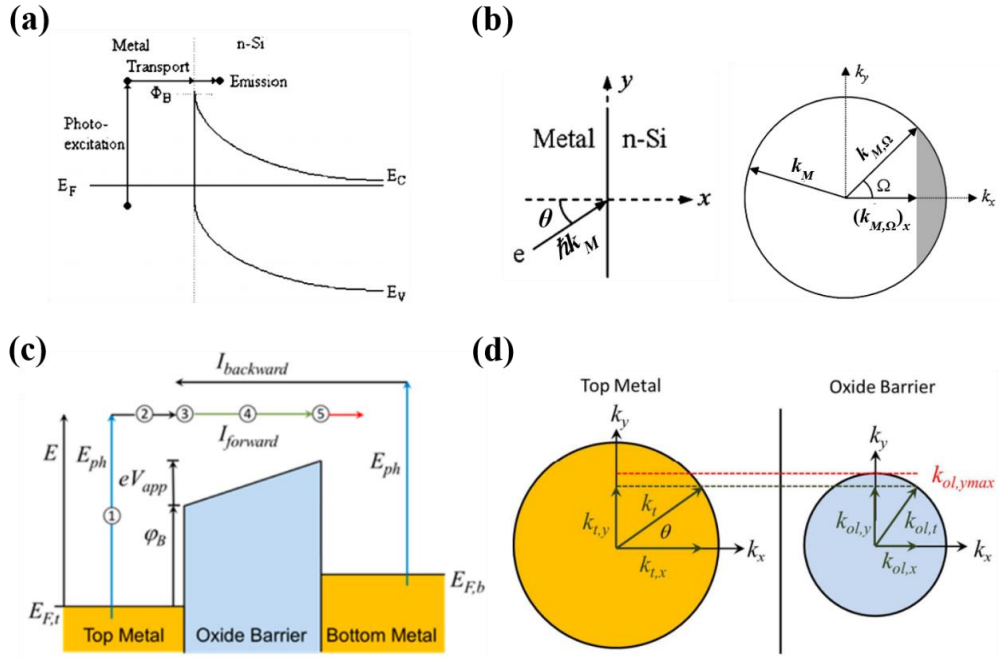

Figure 1.3 (a) Emission of a hot electron over the Schottky barrier in the M/S architecture. (b) The cross-section in the k_x–k_y plane of the k-space emission cone. The rotation about the k_x-axis yields the full cone. Emission is constrained to carriers having a wavevector that

terminates on the surface of the spherical cap (highlighted in gray). (c) Band diagram for the metal/oxide/metal (M/I/M) architecture. The Fermi levels for the top (left) and bottom (right) metals are $E_{F,t}$ and $E_{F,b}$, respectively. The barrier height for the metal/oxide junction is φ_B. When a positive (negative) bias voltage V_{app} is applied to the top metal, the barrier is tilted up (down). Since hot electrons are simultaneously generated in the top and bottom metals, they can generate the forward photocurrent $I_{forward}$ and backward photocurrent $I_{backward}$ that run in the opposite directions. The net photocurrent is $I_{forward}$ - $I_{backward}$. (d) The constant energy contours of hot electrons that are in the top metal and the left side of the oxide barrier. The circles illustrate all terminations of the allowed electron momenta at the energy E. These contours are used in the visualization and description of the ejection of a hot electron into the oxide barrier. Figures reproduced with permission from: (a)-(b) ref. [35], © 2010 IEEE; (c)-(d) ref. [29], © 2014 American Chemical Society.

1.1.2 Present research situation and prospect for hot electron photodetection

The history for photodetectors using internal photoemission can date back to a semicentury ago. Peter et.al firstly achieve NIR photodetection that is below the bandgap of semiconductors through using the Schottky junction formed at M/S interface in 1967 [40]. The absorbed photos transfer their energies to free electrons in the metal and those electrons will cross the M/S barrier once their energies are higher than the barrier height of the Schottky junction. Since the energies of these electrons are higher than the normal ones, these electrons are named as hot electrons. The transport of hot electrons from metal to semiconductor generates a photocurrent which can be measured with an external circuit. Since hot electron photodetectors operate at room temperature, they don't ask for subzero refrigeration. Moreover, they are able to detect NIR light that is below the bandgap of semiconductors, avoiding the usage of the expensive III−V or II−VI compound-based photodetectors, such as the GaSb, InAs, GaAs, HgCdTe and InGaAs based photodetectors. Additionally, the resonant wavelength, bandwidth and polarization dependence can all be modified through controlling the dimensions of the structures. However, the photoelectric conversion efficiency for the planar system is commonly very low due to the high reflectance of metals and the low

generation rate of hot electrons. In the following years, it is found that the structure absorptance and the conversion efficiency can be effectively improved through the light/matter interaction with SPs structures [41].

Hot electrons can also be collected using metal/insulator/metal (M/I/M) architecture apart from the M/S architecture. The generated hot electrons in one side metal go across the insulator layer (the thickness is commonly less than 10 nm) and be collected by the opposite metal, resulting in a photocurrent. The insulator can also be replaced by a semiconductor, which forms the metal/semiconductor/metal (M/S/M) architecture. The mechanisms for the M/I/M architecture and M/S/M architecture are the same, hot electrons are both extracted through the Schottky junction [42]. The M/I/TCO architecture is a derived structure for the M/I/M architecture. Since the absorption coefficient for TCO is small, the absorption of the metal can be increased and therefor improving the photoelectric conversion efficiency [43,44]. Additionally, a planar distributed Bragg reflector (DBR) structure is also reported for hot electron photodetection. Since the Tamm plasmons (TPs) are generated at the metal/DBR interface which facilitates the generation of hot electrons, the structure also exhibits a large photoresponsivity [45]. The present research situation for hot electron photodetectors with M/S architecture, M/I/M architecture and its derivative, and TPs based architecture are introduced detailedly in the following.

1.1.2.1 Metal/semiconductor architecture

In 2011, Knight et al. demonstrated a compact and wavelength-resonant hot electron photodetector with the photocurrent response below the bandgap of the semiconductor [46], as shown in figure 1.4(a). The nanoantenna of this structure not only acts as the light collector but also the electron emitter. Photons of incident light can be first coupled into the nanoantenna and excite resonant SPs. The SPs can then directly decay into energetic hot electrons. After that, these plasmon-induced hot electrons can cross the Schottky barrier formed at the nanoantenna/semiconductor interface, leading to a photocurrent. Moreover, the absorption and photoresponsivity spectra can both be modified by tuning the geometry of the nanoantenna. The plasmonic grating structure can achieve narrowband hot electron

photodetection [47], as shown in figure 1.4(b). The light irradiation strongly couples to surface plasmon polaritons (SPPs) that propagate along the periodically distributed slits in the grating, leading to a narrowband and resonant photoresponse in NIR, which is limited by the Schottky barrier height instead of the bandgap of silicon. The structure exhibits a responsivity of 0.6 mA/W with an internal quantum efficiency (IQE) of 0.2%, which is more than twentyfold of the previously reported nanoantenna-based device. The structure also shows more than threefold narrower photocurrent response than the nanoantenna-based device. Li et al. demonstrated the use of metamaterial perfect absorbers (MPAs) that are made up of ultrathin plasmonic nanostructures can obtain near-unity light absorption [48], as shown in figure 1.4(c). The structure achieves a perfect absorption of light by coupling the localized surface plasmon resonance (LSPR) with the Fabry-Perot (FP) resonance. The structure owns two advantages. The first one is that hot electrons are efficiently and substantially generated attributing to the perfect absorption. The second one is that most of the generated hot electrons are close to the M/S interface, which ensures a low thermalization loss and high transport efficiency. The photocurrent responsivity of this MPA hot electron photodetector is demonstrated to be more than 3 mA/W that is among the highest level yet reported. Additionally, the bandwidth of the photocurrent responsivity spectrum can be broadened through coupling multiple resonators and manipulated via deliberately engineering the geometry. It is known that only a limited number of hot electrons are generated and permitted to cross the Schottky barrier when the plasmonic structure is located on the top surface of the semiconductor. While Knight et al. demonstrated that the hot electron generation and emission can be greatly increased through embedding the plasmonic structure into the semiconductor in 2013 [49], as shown in figure 1.4(d). The embedding can form a 3D Schottky barrier on the vertical sides of the structure, facilitating more emissions of hot electrons across the Schottky barrier into the semiconductor than the planar Schottky barrier and therefore increasing the internal quantum efficiency (IQE) for photodetection. The measured responsivity for the fully embedded device with the embedding depths of 5 nm increases more than 25 times compared to the planar diodes. Even though the concept of using LSPR based nanoantenna for hot electron photodetection below the bandgap of

semiconductor has been demonstrated, the LSPR based structures still cannot meet the practical requirements for the photodetection. In 2014, Lin et al. proposed the deep-trench/thin metal (DTTM) active antenna which couples the surface plasmon resonance (SPR) with the three-dimensional (3D) cavity effects to generate and collect the plasmon-induced hot electrons in the M/S architecture and thereby increase the photocurrent [50], as shown in figure 1.4(e). The DTTM active antenna greatly improves the photocurrent response throughout a broad wavelength range and shows a polarization-independent photodetection. The measured responsivity of the DTTM active antenna are hundreds of times larger than that of the previously reported LSPR-based nanoantennas. The structure also exhibits superior photoelectron conversion efficiency, high degrees of detection linearity for both low (1 $pW/\mu m^2$) and high (4000 W/cm^2) intensity light and the image detection capability for both visible and IR light. In 2019, Feng et al. developed an all-Si based hot electron photodetector, which consists of a deliberately designed metasurface that integrates the antenna with the Si nanowire array [51], as shown in figure 1.4(f). The optical measurement exhibits that an absorption of 90% occurs at the resonant wavelength of 1050 nm. The electrical measurements show that the photocurrent responsivity can reach 94.5 mA/W at the resonant wavelength of 1150 nm with a bandwidth of 480 nm, and the detectivity can reach 4.38×10^{11} $cm \cdot Hz^{1/2}/W$. Such a high responsivity and detectivity in the NIR are comparable with respect to that of previously reported III–V and II–VI compound photodetectors [52-54]. The outstanding performance of the structure results from the increased IQE in the one-dimensional (1D) conduction channels, which accommodates the generated hot electrons for high conduction in Si nanowires.

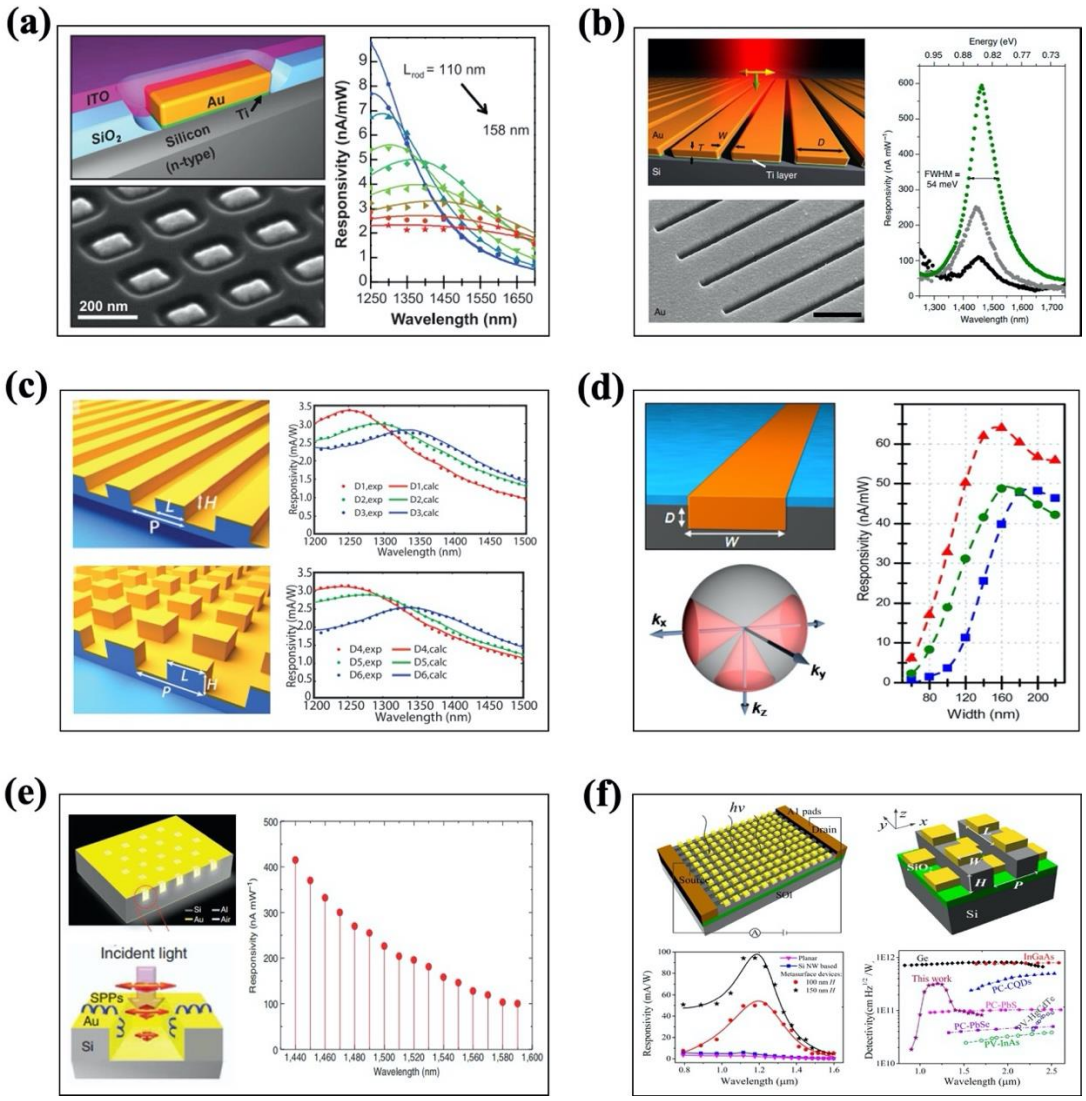

Figure 1.4 Hot electron photodetectors with M/S architecture. (a) Top left: illustration of the optical nanoantenna structure. Bottom left: SEM image of the structure. Right: measured photocurrent responsivity (points) for Au antenna with different lengths (L_{rod}), the solid lines represent the fitting curves. (b) Top left: schematic diagram of an Au grating on a silicon substrate. Bottom left: SEM image of the structure. Right: the measured photocurrent responsivity of the structure for the Au layer thickness of 93 nm (black), 170 nm (grey) and 200 nm (green). (c) Top left: schematic diagram of the MPA photodetector. Top right: comparison of the calculated (line) and measured (circle) photocurrent responsivity spectra

for the MPA photodetector. Bottom left: schematic diagram of the polarization-independent MPA photodetector. Bottom right: comparison of the calculated (line) and measured (circle) photocurrent responsivity spectra for the polarization-independent MPA photodetector. (d) Top left: schematic diagram of the fully embedded plasmonic structure. Bottom left: illustration of the emission cone where hot electrons are permitted to be injected into the semiconductor. Right: the measured responsivities of the structure for the embedding depths of 5 nm (blue), 15 nm (green), and 25 nm (red) at the wavelength of 1500 nm. (e) Left: schematic diagram of the DTTM active antenna structure. Right: photocurrent responsivity of the DTTM structure in the wavelength range of 1440 to 1590 nm. (f) Top: Schematic diagram of the all-Si based hot electron photodetector, which consists of a deliberately designed metasurface that integrates the antenna with the Si nanowire array on a SOI substrate. Bottom left: the measured photocurrent responsivity spectra for the TM polarization. Bottom right: comparison of detectivity among this all-Si based hot electron photodetector and previously reported ones that use the III–V and II–V compounds. Figures reproduced with permission from: (a) ref. [46], © 2011 American Association for the Advancement of Science; (b) ref. [47], © 2013 Springer Nature; (c) ref. [48], © 2014 American Chemical Society; (d) ref. [49], © 2013 American Chemical Society; (e) ref. [50], © 2014 Springer Nature; (f) ref. [51], © 2019 American Chemical Society.

1.1.2.2 Metal/insulator/metal and the derived architectures

In 2014, Chalabi et al. proposed the Au-Al_2O_3-Au (M/I/M) plasmonic structure that reshapes the top metallic layer into nanostripe antennas [29], as show in figure 1.5(a). The measured spectral-dependence, voltage-dependence and polarization-dependence of photocurrent demonstrate that the SPs excitations can lead to a favorable redistribution of electric field in the nanostripe that enhances the photocurrent. By replacing the insulator with semiconductor in the M/I/M architecture, the derived architecture metal/semiconductor/metal (M/S/M) is obtained. Figure 1.5(b) shows the Au-ZnO-Au (M/S/M) photodetector with conformal metallic grating that is proposed by Wu et al. in 2015 [55]. In comparison with the traditional grating structure, the multilayer conformal grating structure shows bigger advantages in both

optical absorption and photocurrent responsivity. The simulation result shows that the multilayer conformal grating structure obtains a strong and asymmetrical light absorption and the absorptance of the top metal exceeds 99%. The photocurrent responsivity of the structure is also predicted to be approximately 3 times of the traditional grating structure due to the extremely high light absorptance and relatively low M/S barrier height.

The use of transparent conducting oxide (TCO) to extract hot electrons for photodetection has also been reported as the derived architecture of the M/I/M architecture, including the M/I/TCO architecture [56] that is shown in figure 1.5(c) and the M/S/TCO architectures [57, 58] that is shown in figure 1.5(d). Since the absorption coefficient of TCO is small, light is mostly absorbed by the metal and the M/I or M/S interface, which results in efficient and asymmetric hot electron generation [56]. The TCO also offers efficient collection of hot electrons, which results in a large net photocurrent. As for the photoresponse speed, recent study on hot electron relaxation dynamics [59] demonstrated that the relaxation time of hot electrons can reach as short as 45 fs. In addition, the photoresponse speed can be controlled through tailoring the geometry of the plasmonic structure since it is strongly affected by the local field enhancement. But more work is still required for fully understanding the mechanism of the photoresponse time of hot electron photodetectors.

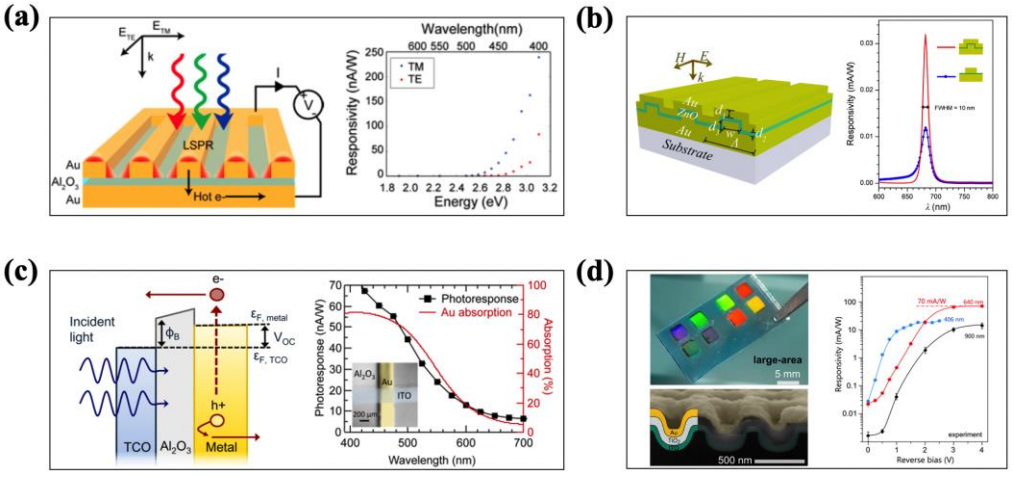

Figure 1.5 Hot electron photodetectors with M/I/M and the derived architectures. (a) Left: schematic illustration of the Au-Al_2O_3-Au (M/I/M) plasmonic nanostripe antenna. Right:

variation of the photocurrent responsivity of the structure with the photon energy for TE and TM polarized light. (b) Left: schematic diagram of the Au-ZnO-Au (M/S/M) photodetector with conformal metallic grating. Right: comparison of responsivity spectrum between the traditional grating structure and the multilayer conformal grating structure. (c) Left: schematic diagram illustrating the generation and collection of hot carriers across the M/I Schottky barrier in the metal-Al_2O_3-TCO (M/I/TCO) structure. Right: photocurrent responsivity and absorptance spectra of the structure with respect to the light wavelength. The inset shows the device cross-junction using a monochrome charge coupled device (CCD). (d) Left: the photo and SEM image of the Au-TiO_2-ITO (M/I/TCO) crystal photodetector. Right: relationship between the responsivity and the applied reverse bias for three different light wavelengths. Figures reproduced with permission from: (a) ref. [29], © 2014 American Chemical Society; (b) ref. [55], © 2015 Springer Nature; (c) ref. [56], © 2014 American Chemical Society; (d) ref. [57], © 2015 American Chemical Society.

1.1.2.3 Tamm plasmons-based architecture

Hot electron photodetectors with M/S, M/I/M and the derived architectures enhance photocurrent through the excitation of SPs. Another kind of hot electron photodetector that enhances the photocurrent through the excitation of Tamm plasmons (TPs) has also been reported currently. TPs are also referred to as optical Tamm states and they exist at the metal/distributed Bragg reflector (DBR) interface. At the resonant wavelength for TPs, the electromagnetic surface waves that propagate along the metal/DBR interface are strongly confined around the interface, resulting in high absorption in the metallic film. This kind of hot electron photodetectors consist of alternating multilayers (DBR) with different refractive index and metallic film. Since the TPs-based architecture exhibits a relatively large photoresponse and does not ask for complicated fabrication techniques, such as electron-beam (EB) lithography, reactive ion etching (RIE) and EB evaporation, hot electron photodetectors with TPs-based architecture dramatically simplify the traditional SPs-based architectures and open the pathway for achieving low-cost and high-responsivity hot electron photodetection. Figure 1.6(a) shows a planar hot electron photodetector that is made up of a

thin metallic layer and a DBR [60]. The absorptance of the structure almost reaches 0.93, leading to a high generation rate of hot electrons that is more than 34-fold of the planar M/S architecture without a DBR. The electric field increases with the penetration depth of light in the metal, which results in a strongly concentrated hot electron generation at the DBR/metal interface. The measured responsivity of the structure is over 30 times of the conventional grating structure. Additionally, the structure exhibits a facile tunability of the resonant wavelength from visible to NIR range, sustained performance at oblique incidence and multiband photodetection. TPs are also used to enhance the generation rate of hot electrons in the M/S/M architecture and therefore improve the photocurrent, as shown in figure 1.6(b) [61]. Results show that the top Au layer absorbs over 87% of light due to the excitation of TPs at the DBR/metal interface. Such a high absorptance leads to a large and unidirectional photocurrent, and the photocurrent responsivity of the structure is much higher than the conventional nanostructures. Additionally, the structure exhibits a narrowband and readily tunable TP resonance and polarization-independent of photocurrent. Zhang et al. proposed a planar microcavity-integrated structure for hot electron photodetection in 2016, in which the M/S/TCO architecture and a buffer layer are sandwiched by two asymmetrical DBRs [62], as shown in figure 1.6(c). The simulation results show that both the absorption efficiency and the resonant wavelength of the structure can be readily manipulated through tailoring the thickness of the buffer layer and the pairs of the top DBR. The absorptance in the metal can reach 0.92 at the resonant wavelength, which is more than 21 times of the structure without a microcavity. The theoretical calculations exhibit that the photocurrent responsivity of the structure can reach 239 nA/mW at 0 V, which is twice of the structure without a microcavity. By replacing the metallic film in conventional TP structure with a M/S/TCO architecture, Wang et al. proposed a wavelength-selective photodetector around the wavelength of 1550 nm [63], as shown in figure 1.6(d). The structure exhibits a sharp and narrow reflectance spectrum with the bandwidth of 43 nm attributing to the excitation of TPs at the DBR/metal interface. The measured photocurrent responsivity reaches the peak with a value of 8.26 nA/mW and the responsivity variation is more than 80% when the light wavelength only

changes 52 nm (from 1581 to 1529 nm), thus leading to a wavelength-selective photodetection in the near infrared.

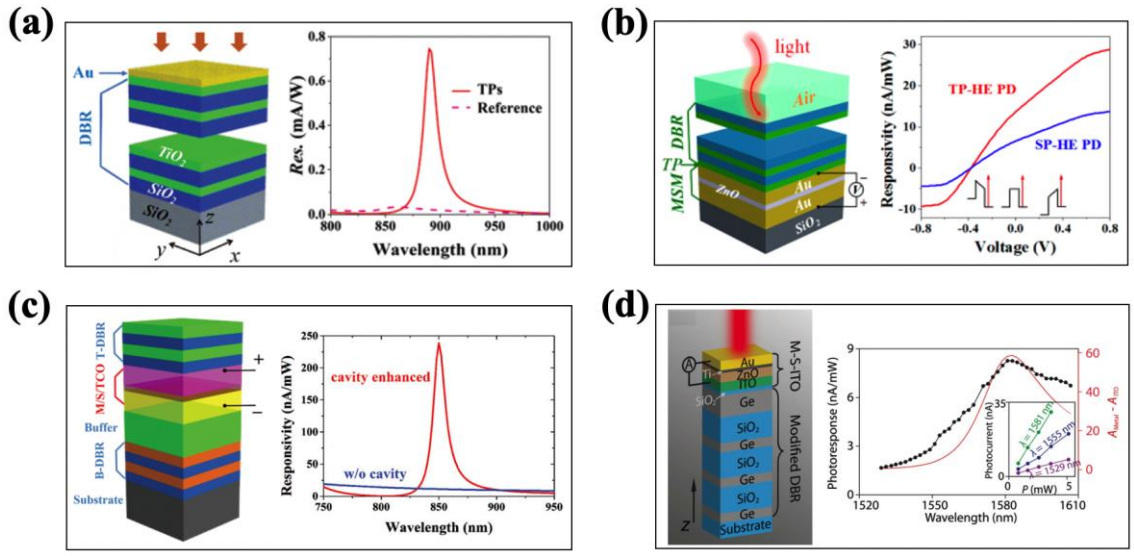

Figure 1.6 Hot electron photodetectors with TPs-based architecture. (a) Left: schematic diagram of the planar DBR-based Au/TiO_2 Schottky photodetector. Right: comparison of the calculated responsivity between the proposed structure and the reference (planar Au/TiO_2 structure without DBR). (b) Left: schematic diagram of the DBR-MSM hybrid structure. Right: the calculated responsivities for the TPs hot electron photodetector (TP-HE PD) and surface plasmon hot electron photodetector (SP-HE PD) as a function of the applied voltage. (c) Left: schematic illustration of the planar microcavity-integrated hot electron photodetector. Right: comparison of the calculated responsivity between the proposed structure and the reference without the microcavity. (d) Left: schematic illustration of the DBR-based M/S/ITO hot electron photodetector. Right: the measured photocurrent responsivity of the proposed structure (black points) at 0 V and the absorptance spectrum difference (red curve) between the metallic layer (A_{Metal}) and the ITO layer (A_{ITO}). The inset shows the relationship between the measured photocurrent and the incident power of light. Figures reproduced with permission from: (a) ref. [60], © 2019 The Royal Society of Chemistry; (b) ref. [61], © 2017 American Chemical Society; (c) ref. [62], © 2016 The Royal Society of Chemistry; (d) ref. [63], © 2019 The Royal Society of Chemistry.

1.2 Refractive index sensing

1.2.1 Basic theory for refractive index sensing

Refractive index (RI) sensing is a technique that uses RI sensors to monitor the refractive index variation of the dielectric medium. Sensitivity (*S*) and figure of merit (FOM) are two important values to estimate the performance of RI sensors. Sensitivity (*S*) is defined as the ratio of the change in output (e.g., resonant wavelength, resonant angle or intensity) to the variation of RI of the surrounding medium. For example, if the output of a RI sensor is resonant wavelength, the sensitivity (*S*) can be calculated by

$$S = \frac{\Delta\lambda}{\Delta n} = \frac{\lambda_2 - \lambda_1}{n_2 - n_1}, \tag{18}$$

where λ represents the resonant wavelength of the RI sensor, *n* represents the refractive index of the surrounding dielectric medium, λ_1 represents the resonant wavelength corresponding to the refractive index of n_1, and λ_2 represents the resonant wavelength corresponding to the refractive index of n_2, as shown in figure 1.7(a). FOM is a gauge for the minimal detectable variation of the refractive index and it can be evaluated by

$$\mathrm{FOM} = \frac{S}{\mathrm{FWHM}}, \tag{19}$$

where FWHM represents the fullwidth at half-maximum and the definition is shown in figure 1.7(b). RI sensors with large sensitivity and FOM simultaneously are desirable for real applications.

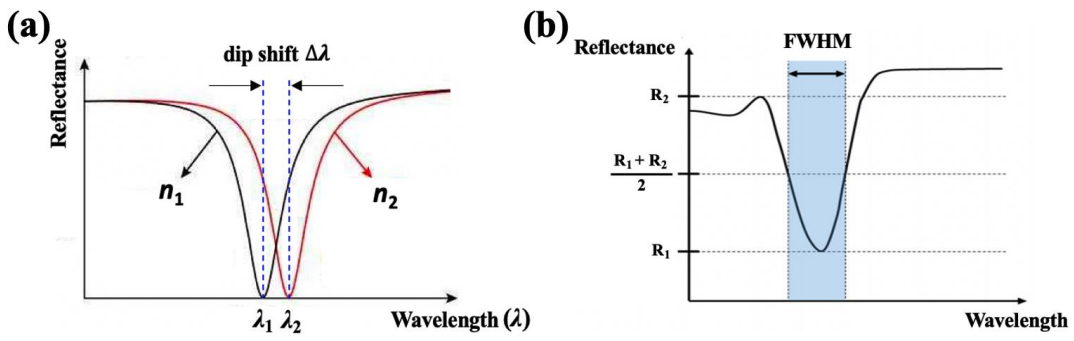

Figure 1.7 (a) Schematic shows the reflectance spectrum variation with the change of refractive index of the surrounding dielectric medium for RI sensors. (b) Schematic shows the definition of FWHM.

Metal-based plasmonic RI sensor and dielectric-based photonic RI sensor are two main types of RI sensors. In this thesis, we focus on the investigation of metal-based plasmonic RI sensor. Basing on whether the excited plasmon is localized to a metallic nanostructure or oscillates at the metal/dielectric interface, metal-based plasmonic RI sensor can be separated to localized surface plasmon resonance (LSPR) based sensor and surface plasmon polariton (SPP) based sensor.

LSPR represents the collective electron charge oscillations in metallic nanostructures, such as metallic nanoparticles. At the resonance condition, the electric field is strongly enhanced and highly localized around the nanostructure, resulting in the output (e.g., resonant wavelength, resonant angle or intensity) to be sensitive to the variation of the surrounding dielectric medium. Nanoparticle-based and nanohole-based architectures are two main architectures for LSPR-based RI sensors. LSPR-based RI sensors have the advantages of simplicity, low-cost and easy for integration. But LSPR-based RI sensors typically have a broad bandwidth and exhibit a low FOM due to the strong radiative damping.

SPP based RI sensors typically achieve larger sensitivities than LSPR based RI sensors due to the longer plasmon decay length [64,65] and bigger interaction volume between the propagating wave and the sample. SPP is a nonradiative electromagnetic surface wave that propagates along the metal/dielectric interface. The oscillations of electron charges at the

metal/dielectric interface are very sensitive to the minute change of the surrounding dielectric medium. SPP cannot be excited at a planar metal/dielectric interface by direct illumination. The exciting wave must have specific momentum for the excitation of SPP. To fulfill the momentum requirement, four types of SPP based RI sensors have been reported, which are prism-coupled SPP based RI sensor, grating-coupled SPP based RI sensor, waveguide-coupled SPP based RI sensor and fiber-coupled SPP based RI sensor [66]. The schematics of the four types of SPP based RI sensor are shown in figure 1.8. Prism-coupled SPP based RI sensor is the first developed and most widely used for RI sensing. The Kretschmann configuration [67], as shown in figure 1.8(a), and the Otto configuration [68] are the two configurations for prism-coupled SPP based RI sensors. Both of them are made up of a prism with high refractive index (n_{p}), a thin metallic film and a dielectric layer (surrounding dielectric medium) with a relatively lower refractive index (n_{d}) than the prism. The evanescent wave generated by the incident light at the prism/metal interface with total reflection penetrates into the metal layer with a certain dipth and excites SPP propagating along the metal/dielectric interface when the phases of the evanescent wave and the SPP are matched, which is shown as [69]

$$k_0 n_{\mathrm{p}} \sin\theta = \mathrm{R_e}\{\beta_{\mathrm{SP}}\} = \mathrm{R_e}\left\{k_0 \sqrt{\frac{\varepsilon_{\mathrm{m}} n_{\mathrm{d}}^2}{\varepsilon_{\mathrm{m}} + n_{\mathrm{d}}^2}}\right\}, \tag{20}$$

where k_0 represents the wavenumber in free space, θ represents the incident angle of light, β_{SP} represents the propagation constant of SPP, ε_{m} represents the permittivity of metal which can be shown as $\varepsilon_{\mathrm{m}} = \varepsilon_{\mathrm{mr}} + \mathrm{i}\varepsilon_{\mathrm{mi}}$. A variation in the RI of the dielectric layer leads to a change in the wave phase and results in a variation in the spectral response of the sensor. The diffracted light waves in the metal grating can couple to SPP for the grating-coupled SPP based RI sensors, as shown in figure 1.8(b), when the following coupling condition is satisfied [69]

$$k_0 n_{\mathrm{d}} \sin\theta + m\frac{2\pi}{\Lambda} = \pm\mathrm{R_e}\{\beta_{\mathrm{SP}}\} = \pm\mathrm{R_e}\left\{k_0 \sqrt{\frac{\varepsilon_{\mathrm{m}} n_{\mathrm{d}}^2}{\varepsilon_{\mathrm{m}} + n_{\mathrm{d}}^2}}\right\}, \tag{21}$$

where *m* is an integer that represents the diffraction order and Λ is the period of the diffraction grating. The advantage of the waveguide-coupled SPP based RI sensor is miniatured structure dimensions and easy for integration. As shown in figure 1.8(c), the guided transverse magnetic (TM) polarized light first propagates through the waveguide, then penetrates into the metal strip evanescently and last the SPP is excited at the metal/superstrate interface [70]. The coupling between the incident light and the SPP for waveguide-coupled SPP based RI sensor is similar with the prism-coupled SPP based RI sensor. For fiber-coupled SPP based RI sensor, the fiber core works as the prism in the Kretschmann configuration. To achieve high performance with the fiber-coupled SPP based RI sensor, some modifications are required to the optical fibers for the coupling of the core-guided light and SPP, such as strip the fiber cladding completely and deposit metal layers on the fiber core [71], as shown in figure 1.8(d). Fiber-coupled SPP based RI sensors exhibit some advantages over the prism-coupled SPP based RI sensors, such as small footprint, low cost and remote sensing ability.

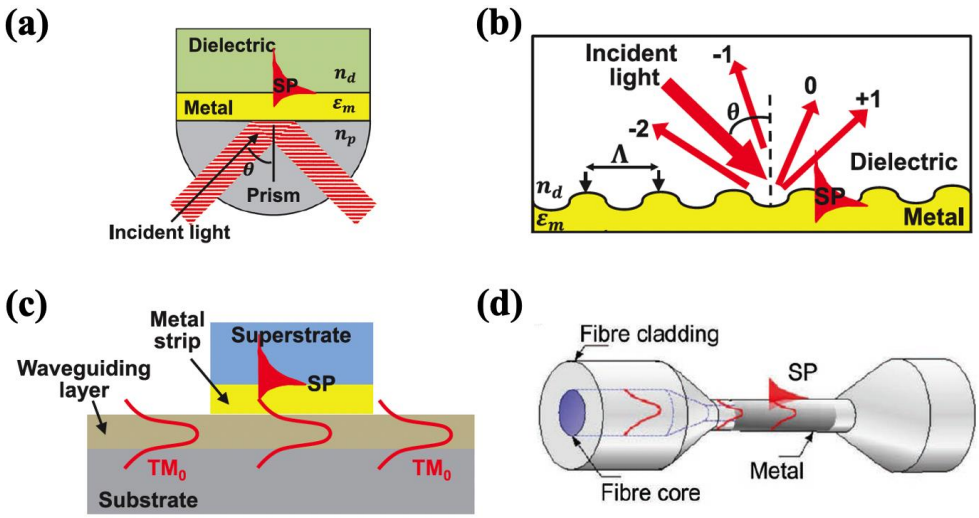

Figure 1.8 The schematics of the four types of SPP based RI sensor: (a) prism-coupled SPP based RI sensor, (b) grating-coupled SPP based RI sensor, (c) waveguide-coupled SPP based RI sensor and (d) fiber-coupled SPP based RI sensor. Figures are redrawn from ref. [70].

1.2.2 Present research situation and prospect for refractive index sensing

LSPR based RI sensors mainly consists of LSPR sensor based on nanoparticle and LSPR sensor based on nanoholes. As shown in figure 1.9(a), LSPR sensors based on nanoparticle have different configurations, such as nanosphere (i), nanocube (ii), nanorod (iii) and nanoprism (iV). The corresponding SEM images for these configurations are shown in figure 1.9(b). Khan et al. demonstrated that the aspect ratio (R) of the nanoparticle, defined by $R = L/d$, plays the key role in determining the sensitivity of LSPR sensors based on nanoparticles, regardless of the composition, shape, dimension, and cross-sectional area [72]. The measured sensitivities (S) for LSPR sensors based on different nanoparticles exhibit a linear relationship with the aspect ratio (R), as shown in figure 1.9(c). A linear relationship between the sensitivity and the initial resonant wavelength $\lambda_{\mathrm{LSPR,0}}$ can be also obtained when $\lambda_{\mathrm{LSPR,0}}$ is smaller than 1000 nm, as shown in figure 1.9(d). The sensitivity splits when $\lambda_{\mathrm{LSPR,0}}$ exceeds 1000 nm, which indicates the sensitivity of LSPR sensor based on nanoparticle depends more linearly on the aspect ratio than the initial resonant wavelength. Up to now, the reported highest sensitivity and FOM for LSPR sensor based on nanoparticle are 1816 nm/RIU [73] and 23 RIU^{-1} [74].

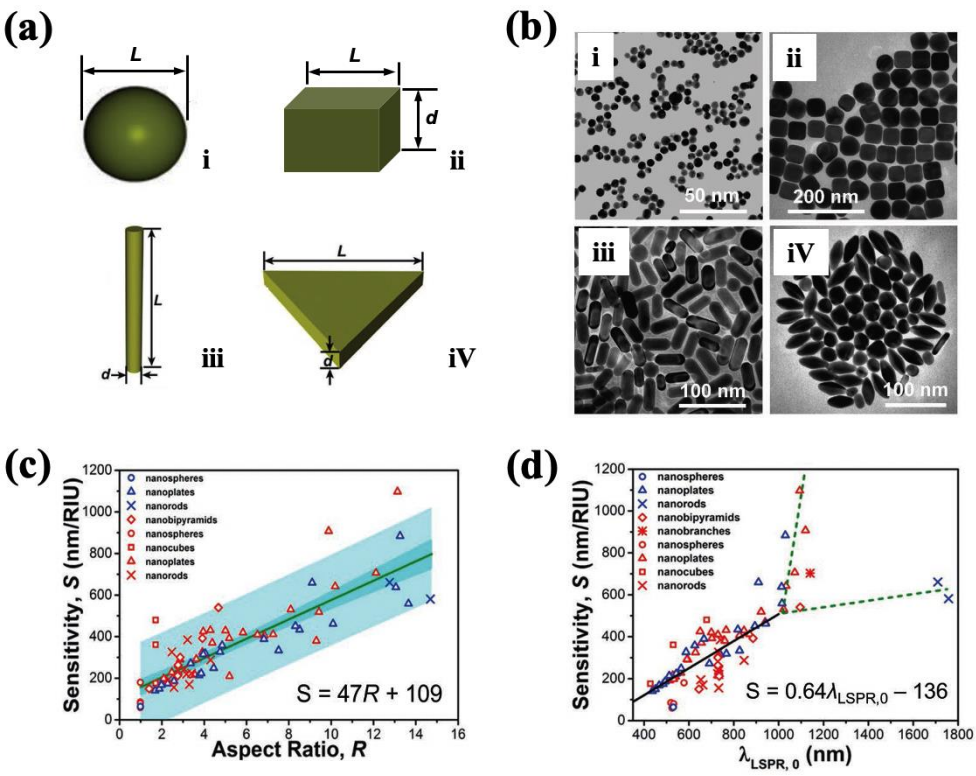

Figure 1.9 (a) LSPR sensors based on nanoparticles with the shapes of i: nanosphere, ii: nanocube, iii: nanorod and iV: nanoprism. (b) SEM images for i: Au nanospheres, ii: Au nanocubes, iii: Au nanorod and iV: Au nanoprism. (c) The measured sensitivity for LSPR sensors based on nanoparticles as a function of (c) aspect ratio (*R*), and (d) resonant wavelength ($\lambda_{LSPR,0}$). Figures reproduced with permission from ref. [72], © 2016 American Chemical Society.

LSPR sensors based on nanoholes generally show a similar sensitivity with LSPR sensors based on nanoparticles, but they usually have a higher FOM attributing to the excitation of Bloch wave SPP [75] or Fano resonance [76] which shows a smaller FWHM than LSPR [77–79]. The template stripped Ag nanohole array is one of the typical architectures for LSPR sensors based on nanoholes, as shown in figure 1.10(a) [80]. Liu et al. proposed a LSPR sensors made up of an Ag nano-Lycurgus cup (NLC) array in 2013, where the sidewall of NLC was decorated with Ag nanoparticles, as shown in figure 1.10(b) [81]. The measured average sensitivity of this sensor reaches as high as 8066 nm/RIU with the FOM of 179 RIU^{-1}.

Such a high FOM has exceeded the theoretical limit (108 RIU^{-1}) of standard Au based SPP sensors [82]. Nanohole-based 3D structures have also been used for RI sensing [83–85]. As shown in figure 1.10(c), the Ag disk-in-volcano array exhibits a sensitivity more than 900 nm/RIU [86].

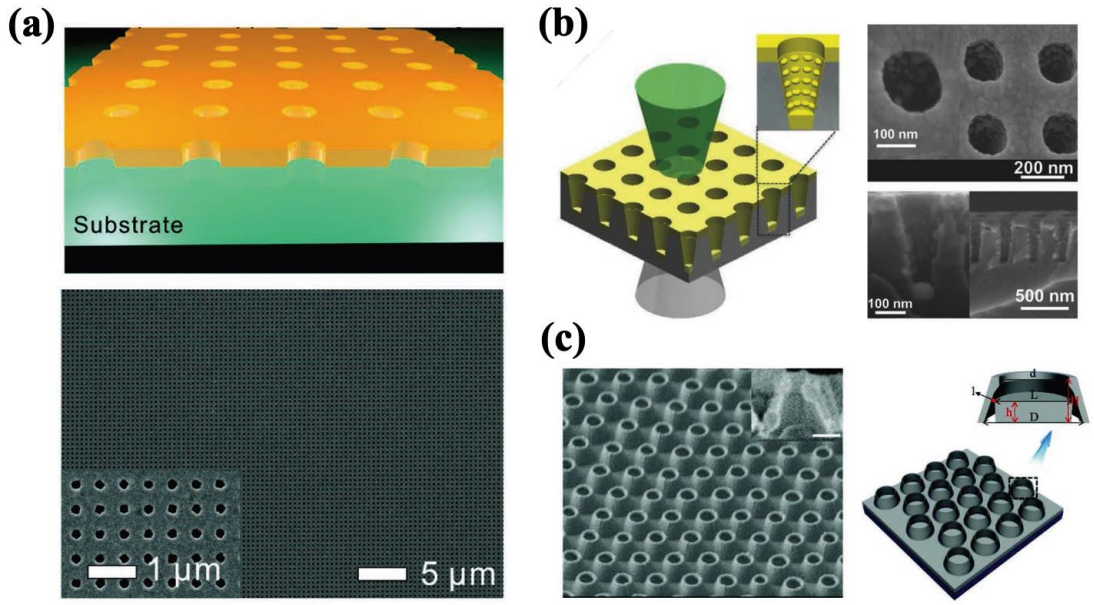

Figure 1.10 LSPR sensors based on nanoholes. The schematic and SEM images of the LSPR sensor based on: (a) template stripped Ag nanohole array, (b) nano Lycurgus cup array and (c) disk-in-volcano array. Figures reproduced with permission from: (a) ref. [80], © 2011 American Chemical Society; (b) ref. [81], © 2013 WILEY‐VCH Verlag GmbH & Co. KGaA, Weinheim; (c) ref. [86], © 2015 The Royal Society of Chemistry.

SPP based RI sensors are commercially available now due to the high sensitivity and FOM. SPP based RI sensors can be separated into prism-coupled SPP based RI sensor, grating-coupled SPP based RI sensor, waveguide-coupled SPP based RI sensor and fiber-coupled SPP based RI sensor [66]. The reports show that the sensitivities of prism-coupled SPP based RI sensors can easily exceed 1000 nm/RIU with the Kretschmann configuration [66]. The sensitivity can even reach 31400 nm/RIU for the Au-coated prism-coupled SPP sensor [87]. The prism-coupled multichannel SPP based sensors have also been proposed [88,89]. As

shown in figure 1.11(a), a 8-channel SPP based RI sensor combing the traditionally channel with the wavelength division multiplexing was proposed by Homola in 2005 [88]. This sensor is able to obtain two SPP dips in the transmission spectrum. The sensitivity of it reaches 8800 nm/RIU with simultaneous detection of multiple analytes. Grating-coupled SPP based RI sensors also have different architectures, such as 1D metal grating and 2D metal grating. The Au-covered TiO_2 1D grating based sensor exhibits a sensitivity around 940 nm/RIU with a FOM of 62.5 RIU^{-1} [90]. Homola et al. reported a 1D grating-coupled SPP sensor with SPR coupler and disperser [91], as shown in figure 1.11(b). The sensitivity of this sensor achieves more than 600 nm/RIU. SPP based RI sensors with 2D gratings, such as nanopyramidal gratings [92], nanotrench gratings [93] and crossed gratings [94], are demonstrated to have improved the sensitivity and FOM compared with the 1D grating based sensors. Waveguide-coupled SPP based sensors are reported to have similar sensitivity with prism-coupled SPP based sensors [95]. As shown in figure 1.11(c), a Cu-coated polymer waveguide-coupled SPP sensor exhibits the coupling of the core mode of the waveguide and the SPP mode, resulting in a sensitivity over 48600 nm/RIU with the FOM of 160 RIU^{-1} [96]. The waveguide-coupled SPP sensors with symmetrical metal-cladding architectures have also been reported for RI sensing [97,98]. Fiber-coupled SPP based RI sensors with different architectures have also been demonstrated, such as the geometry-modified fibers, grating-assisted fibers and specialty fibers. As shown in figure 1.11(d), the metallic grating on fiber surface (i) [99] and U-shaped fiber (ii) [100] are two common geometry-modified fibers for RI sensing. Grating-assist fiber sensors make gratings in fiber cores instead of on the fiber surface. Long period fiber grating and short period fiber grating are two types of grating-assisted fibers according to the period of the grating. The short period fiber grating usually refers to fiber Bragg grating (FBG), as shown in (iii) of figure 1.11(c) [100]. Some specialty fibers have also been proposed for RI sensing besides the traditional fibers, such as the hollow fiber [101], as shown in (iV) of figure 1.11(c), the microstructured optical fiber [102] and polarization-maintaining fiber [103].

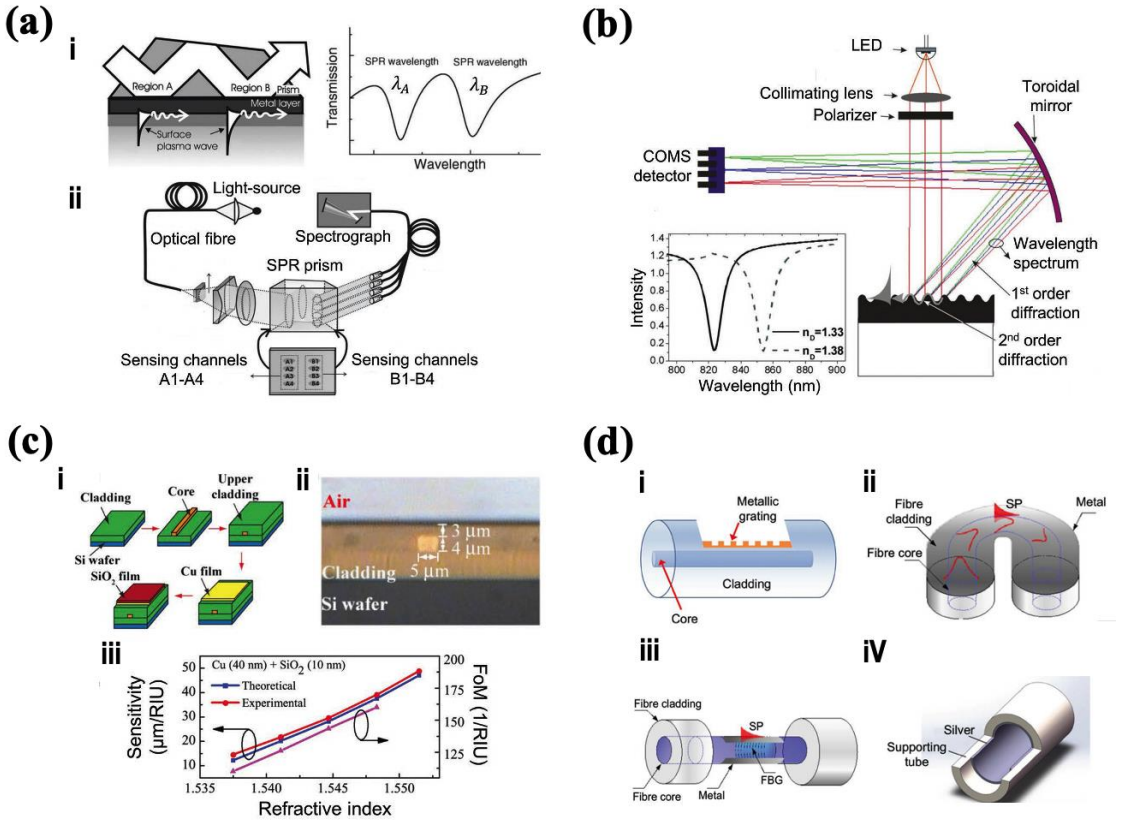

Figure 1.11 (a) Prism-coupled SPP based RI sensor with multichannel. i: working principle, ii: the experimental setup of the SPP sensor with 8 channels. (b) Grating-coupled SPP based RI sensors with the SPR coupler and disperser. (c) Cu-coated polymer waveguide-coupled SPP based RI sensor. i: the fabrication process, ii: the microscope image of the end of the face, iii: the sensitivity and FOM of the sensor. (d) Schematics of fiber-coupled SPP based RI sensors with different configurations: i: metal grating on fiber, ii: U-shaped fiber, iii: fiber Bragg grating (FBG), iV: hollow fiber. Figures reproduced with permission from: (a) ref. [88], © 2005 Elsevier B.V.; (b) ref. [91], © 2008 Elsevier B.V.; (c) ref. [96], © 2016 IEEE; (d) i: ref. [99], © 2013 IEEE; ii-iii: ref. [100], © 2017 MDPI; iV: ref. [101], © 2015 MDPI.

1.3 Thesis overview

1.3.1 Research purpose and significance

The research purposes for this thesis are: (1) studying the mechanisms for hot electron photodetectors (chapter 1), (2) designing and fabricating hot electron photodetectors with excellent spectral-selectivity, narrow bandwidth, and high responsivity in the telecommunication C-band. To achieve this goal, we propose the deliberately designed hot electron photodetectors which are Si channel-separated parallel grating structure (chapter 2), Si channel-separated interdigitated grating structure (chapter 3), DBR-film structure and grating-on-DBR structure (chapter 4), (3) building a theoretical model to quantify the photocurrent response in terms of the optical and electrical properties of hot electron photodetectors and finding solutions for improving the photocurrent response according to the model. (4) designing a RI sensor using new architecture to achieve RI sensing with high sensitivity and figure of merit.

Even though a plenty of hot electron photodetectors with different plasmonic structures have been reported till now, the low generation efficiency of hot electrons, low internal quantum efficiency, and small photocurrent responsivity limit their actual applications. Therefore, the investigation on how to increase the photoelectric conversion efficiency of hot electron photodetectors is urgently needed. The emergence of SPs-based hot electron photodetector enhances the generation efficiency of hot electrons and facilitates the photocurrent. But more SPs-based hot electron photodetectors with different architectures (M/S, M/I/M, M/S/M, M/I/TCO, M/S/TCO, etc.) are still required to further improve the photocurrent responsivity. At the same time, it is also of crucial importance to increase the photoresponse speed of hot electron photodetectors. As for RI sensing, it is important to propose new metal-based plasmonic RI sensors with new architectures to achieve high sensitivity and figure of merit simultaneously. To achieve this goal, the plasmon mode should be deliberately designed to get stronger electric field enhancement at the metal/dielectric interface besides the conventional pure LSPR mode and SPP mode.

1.3.2 Research content

In this thesis, we explore the mechanism for hot electron photodetectors, and propose a Si channel-separated parallel grating structure, a Si channel-separated interdigitated grating structure, a DBR-film structure and a grating-on-DBR structure. The first two structures exhibit a spectrally selective photodetection with relatively high responsivity and narrow bandwidth in the telecommunication C-band. The DBR-film structure excites the TPs to facilitate the photocurrent responsivity. The grating-on-DBR structure further improves the generation of hot electrons and facilitates the photocurrent responsivity attributing to the grating-on-DBR mode. The theoretical calculations of the generation, transport and collection of hot electrons, and the photocurrent responsivity of the proposed structures are also investigated.

In chapter 1, the basic theory for hot electron photodetectors is introduced, including the generation, transport and collection process of hot electrons. The formation of photocurrent in hot electron photodetectors is also clearly clarified. The present research situations for hot electron photodetectors with M/S architecture, M/I/M and the derived architectures, and the TPs-based architecture are also introduced. Lastly, the overview for this thesis, including the research purpose and significance, and the research content, is clearly clarified.

In chapter 2, a Si channel-separated parallel grating structure is proposed and investigated. Due to the strong field enhancement at the metal/air interface and tunable resonant wavelength with the change of refractive index (RI) of the surrounding medium, the structure shows a high potential for the application of refractive index sensing in the near infrared. The structure exhibits a strong capacity to trap and confine light with different plasmon modes. The channel enhanced surface plasmon polariton (SPP) mode enhances the electric field at the metal/air interface at normal incidence, resulting in the reflectance dip highly sensitive to the change of refractive index of the surrounding medium. The linear fitting sensitivity corresponding to this mode reaches as high as 775 nm/refractive index unit (RIU) with the figure of merit (FOM) approaching 48, which is competitive with previously

reported RI sensors with plasmonic nanostructures. The electric fields at the metal/air interface and the top-surface of Si channels are also strongly enhanced attributing to the coupling of SPP mode and channel mode when the incident light is tilted, exhibiting a high sensitivity to the refractive index variation of the surrounding medium. The linear fitting sensitivity corresponding to this mode at the incident angle of 3° reaches 753 nm/RIU with a FOM of 13. The reflectance dip shows no shift to the change of the surrounding medium for the SPP mode that propagates along the M/S interface because of the weak field enhancement at the Au/air interface. However, by taking advantage of the SPP induced hot electrons, the structure overcomes the native limitations from the bandgap of semiconductors and achieves sub-bandgap photodetection with relative high responsivity. The measured responsivity for the structure with the period of 850 nm shows the spectral selectivity in the C-band with the peak responsivity of 72.5 nA/mW at the resonant wavelength of 1538 nm. The measured responsivity for the structure with a period of 840 nm steadily decreases across the C-band as the wavelength increases. The responsivity variation within the C-band reaches as high as 70.5%, demonstrating the excellent spectral selectivity in the C-band. With these outstanding properties, the proposed structure is promising for numerous applications that require narrowband and spectrally selective detection.

In chapter 3, a Si channel-separated interdigitated grating structure is investigated both theoretically and experimentally. The structure efficiently guides and confines light in the structure through the excitation of SPPs at the M/S interface, leading to strongly resonant and narrowband optical response and strong field enhancements. By taking advantage of the narrowband optical response and the enhanced generation of hot electrons, the structure achieves spectrally selective photodetection with high responsivity in the C-band. The measured full-width at half maximum (FWHM) reaches as narrow as 23 nm and the measured responsivity reaches as high as 804 nA/mW at the resonant wavelength of 1550 nm and the bias voltage of 0.08 V, showing a competitive performance with respect to previously reported Si-based NIR photodetectors. The responsivity represents a large variation of 59% when the light wavelength is varied by only 20 nm, from 1550 nm to 1530 nm. A theoretical model is also performed to quantify the photocurrent response in terms of

the optical and electrical properties of the structure. The strongly resonant and narrowband photocurrent response and readily tunable resonant wavelength not only enable the structure to achieve spectrally selective photodetection in the near-infrared but also make it amenable to the application of sensing devices, imaging devices and other optoelectronic devices working in the sub-bandgap regime of semiconductor materials.

In chapter 4, we propose a DBR-film structure and a grating-on-DBR structure. The DBR-film structure consists of 5 pairs of alternating SiO_2/Si layers and an ultrathin Au film on the top. It achieves a high absorptance of 0.83 at the resonant wavelength of 1547 nm. The generation of hot electrons is enhanced by the excitation of TPs at the metal/DBR interface, which facilitates the photocurrent response. The grating-on-DBR structure further increases the absorptance in the C-band and shows a larger modulation (relative to the incident wave) compared with the DBR-film structure and Si-based Au grating structure. The distribution of electric field in the structure is strongly enhanced at the metal/DBR interface, which is likely originating from the coupling of FP resonance and TP resonance due to the grating-on-DBR mode. Due to the strong field enhancement at the metal/DBR interface, the generation of hot electrons in the metal is greatly facilitated and a large photocurrent is produced. The two structures both exhibit a narrowband and high photocurrent responsivity in the near-infrared, which opens a new way for the TPs-based hot electron photodetectors.

In chapter 5, the conclusions for the research on hot electron photodetectors and the plan for the future work are clarified.

References

[1] C. Clavero, "Plasmon-induced hot-electron generation at nanoparticle/metal-oxide interfaces for photovoltaic and photocatalytic devices," *Nat. Photonics* **8**, 95-103 (2014)

[2] R. H. Fowler, "The analysis of photoelectric sensitivity curves for clean metals at various temperatures," *Phys. Rev.* **38**, 45–56 (1931)

[3] W. Spicer, "Photoemissive, photoconductive, and optical absorption studies of alkali-antimony compounds," *Phys. Rev.* **112**, 114–122 (1958)

[4] W. E. Spicer, "Negative affinity 3-5 photocathodes: their physics and technology," *Appl. Phys*. **12**, 115–130 (1977)

[5] M. W. Knight, H. Sobhani, P. Nordlander, and N. J. Halas, "Photodetection with active optical antennas," *Science* **332**, 702–704 (2011)

[6] W. Li, and J. Valentine, "Metamaterial perfect absorber based hot electron photodetection," *Nano Lett.* **14**, 3510–3514 (2014)

[7] Y. K. Lee, C. H. Jung, J. Park, H. Seo, G. A. Somorjai, and J. Y. Park, "Surface plasmon-driven hot electron flow probed with metal semiconductor nanodiodes," *Nano Lett.* **11**, 4251–4255 (2011)

[8] T. P. White, and K. R. Catchpole, "Plasmon-enhanced internal photoemission for photovoltaics: theoretical efficiency limits," *Appl. Phys. Lett.* **101**, 073905 (2012)

[9] P. Narang, R. Sundararaman, and H. A. Atwater, "Plasmonic hot carrier dynamics in solid-state and chemical systems for energy conversion," *Nanophotonics* **5**, 96–111 (2016)

[10] C. Sönnichsen, T. Franzl, T. Wilk, G. von Plessen, and J. Feldmann, "Drastic reduction of plasmon damping in gold nanorods," *Phys. Rev. Lett.* **88**, 077402 (2002)

[11] J. Endriz, and W. Spicer, "Surface-plasmon-one-electron decay and its observation in photoemission," *Phys. Rev. Lett.* **24**, 64–68 (1970)

[12] T. Inagaki, K. Kagami, and E. Arakawa, "Photoacoustic observation of nonradiative decay of surface plasmons in silver," *Phys. Rev. B* **24**, 3644–3646 (1981)

[13] J. B. Khurgin, "How to deal with the loss in plasmonics and metamaterials," *Nat. Nanotechnol.* **10**, 2–6 (2015)

[14] C. F. Bohren, "How can a particle absorb more than the light incident on it?" *Am. J. Phys.* **51**, 323 (1983)

[15] A. O. Govorov, H. Zhang, and Y. K. Gun'ko, "Theory of photo injection of hot plasmonic carriers from metal nanostructures into semiconductors and surface molecules," *J. Phys. Chem. C* **117**, 16616–16631 (2013)

[16] A. Manjavacas, J. G. Liu, V. Kulkarni, and P. Nordlander, "Plasmon induced hot carriers in metallic nanoparticles," *ACS Nano* **8**, 7630–7638 (2014)

[17] B. Y. Zheng, H. Zhao, A. Manjavacas, M. McClain, P. Nordlander, and N. J. Halas, "Distinguishing between plasmon-induced and photoexcited carriers in a device geometry," *Nat. Commun.* **6**, 7797 (2015)

[18] A. O. Govorov, and H. Zhang, "Kinetic density functional theory for plasmonic nanostructures: breaking of the plasmon peak in the quantum regime and generation of hot electrons," *J. Phys. Chem. C* **119**, 6181–6194 (2015)

[19] F. Wang, and N. A. Melosh, "Power-independent wavelength determination by hot carrier collection in metal-insulator-metal devices," *Nat. Commun.* **4**, 1711 (2013)

[20] H. Lee, Y. K. Lee, E. Hwang, and J. Y. Park, "Enhanced surface plasmon effect of Ag/TiO_2 nanodiodes on internal photoemission," *J. Phys. Chem. C* **118**, 5650–5656 (2014)

[21] S. M. Sze, and K. K. Ng, "Physics of semiconductor devices, 3rd ed," *New Jersey: John Wiley, Sons, Inc.* p. 682 (2007)

[22] H. Xue, W. Y. Chen, C. X. Liu, X. Z. Kong, P. F. Qu, Z. R. Liu, J. R. Zhou, L. Shen, Z. C. Zhong, and S. P. Ruan, "Fabrication of TiO_2 Schottky barrier diodes by RF magnetron sputtering," *3rd IEEE International Conference on Nano/Micro Engineered and Molecular Systems*, pp. 108–11 (2008)

[23] J-J. Huang, C-W. Kuo, W-C. Chang, and T-H. Hou, "Transition of stable rectification to resistive-switching in Ti/TiO_2/Pt oxide diode," *Appl. Phys. Lett.* **96**, 262901 (2010)

[24] D. L. Carroll, M. Wagner, M. Rühle, and D. A. Bonnell, "Schottky-barrier formation at nanoscale metal-oxide interfaces," *Phys. Rev. B* **55**, 9792–9799, (1997)

[25] X. T. Wang, C. H. Liow, D. P. Qi, B. W. Zhu, W. R. Leow, H. Wang, C. Xue, X. D. Chen, and S. Z. Li, "Programmable photo-electrochemical hydrogen evolution based on multi-segmented CdS-Au nanorod arrays," *Adv. Mater.* **26**, 3506–3512 (2014)

[26] R. R. Lieten, V. V. Afanas'ev, N. H. Thoan, S. Degroote, W. Walukiewicz, and G. Borghs, "Mechanisms of Schottky barrier control on n-type germanium using Ge_3N_4 interlayers," *J. Electrochem. Soc.* **158**, H358 (2011)

[27] C. Henkel, S. Abermann, O. Bethge, G. Pozzovivo, S. Puchner, H. Hutter, and E. Bertagnolli, "Reduction of the PtGe/ Ge electron Schottky-barrier height by rapid thermal diffusion of phosphorous dopants," *J. Electrochem. Soc.* **157**, H815 (2010)

[28] A. D. Semenov, G. N. Gol'tsman, and R. Sobolewski, "Hot-electron effect in superconductors and its applications for radiation sensors," *Supercond. Sci. Technol*. **15**, R1 (2002)

[29] H. Chalabi, D. Schoen, and M. L. Brongersma, "Hot-electron photodetection with a plasmonic nanostripe antenna," *Nano. Lett*. **14**, 1374-1380 (2014)

[30] H. Hertz, "Ueber einen Einfluss des ultravioletten Lichtes auf die electrische Entladung," *Ann. Phys.* **267**, 983–1000 (1887)

[31] M. L. Brongersma, N. J. Halas, and P. Nordlander, "Plasmon-induced hot carrier science and technology," *Nat. nanotech.* **10**, 25 (2015)

[32] A. O. Govorov, H. Zhang, H. V. Demir, and Y. K. Gun'ko, "Photogeneration of hot plasmonic electrons with metal nanocrystals: Quantum description and potential applications," *Nano Today*, **9**, 85-101 (2014)

[33] R. Sundararaman, P. Narang, A. S. Jermyn, W. A. Goddard III, and H. A. Atwater, "Theoretical predictions for hot-carrier generation from surface plasmon decay," *Nat. Commun*. **5**, 1-8 (2014)

[34] A. M. Brown, R. Sundararaman, P. Narang, W. A. Goddard III, and H. A. Atwater, "Nonradiative plasmon decay and hot carrier dynamics: effects of phonons, surfaces, and geometry," *ACS Nano*, **10**, 957-966 (2016)

[35] C. Scales, and P. Berini, "Thin-film Schottky barrier photodetector models," *IEEE J. Quantum. Elect.* **46**, 633-643 (2010)

[36] E. O. Kane, "Simple model for collision effects in photoemission," *Physical Review*, **147**, 335 (1966)

[37] V. L. Dalal, "Simple model for internal photoemission," *Journal of Applied Physics*, **42**, 2274-2279 (1971)

[38] T. K. Gaylord, and K. F. Brennan, "Electron wave optics in semiconductors," *Journal of applied physics*, **65**, 814-820 (1989)

[39] I. Goykhman, B. Desiatov, J. Shappir, J. B. Khurgin, and U. Levy, "Model for quantum efficiency of guided mode plasmonic enhanced silicon Schottky detectors". *arXiv preprint arXiv,***1401**, 2624 (2014)

[40] D. W. Peters, "An infrared detector utilizing internal photoemission," *Proceedings of the IEEE*, **55**, 704−705 (1967)

[41] W. Li, and J. G. Valentine, "Harvesting the loss: surface plasmon-based hot electron photodetection," *Nanophotonics* **6**, 177−191 (2017)

[42] C. Zhang, K. Wu, V. Giannini, and X. F. Li "Planar hot-electron photodetection with Tamm plasmons," *ACS Nano* **11**, 1719−1727 (2017)

[43] T. Gong, and J. N. Munday, "Angle-independent hot carrier generation and collection using transparent conducting oxides," *Nano Lett.* **15**, 147−152 (2014)

[44] F. P. García de Arquer, A. Mihi, G. Konstantatos. "Large-area plasmonic-crystal–hot-electron-based photodetectors," *ACS Photonics* **2**, 950−957 (2015)

[45] R. Li, C. Zhang, and X. Li, "Schottky hot-electron photodetector by cavity-enhanced optical Tamm resonance," *Appl. Phys. Lett.* **110**, 013902 (2017)

[46] M. W. Knight, H. Sobhani, P. Nordlander, and N. J. Halas, "Photodetection with active optical antennas," *Science* **332**, 702−704 (2011)

[47] A. Sobhani, M. W. Knight, Y. Wang, B. Zheng, N. S. King, L. V. Brown, Z. Fang, P. Nordlander and N. J. Halas, "Narrowband photodetection in the near-infrared with a plasmon-induced hot electron device," *Nat. Commun*. **4**, 1643 (2013)

[48] W. Li, and J. Valentine, "Metamaterial perfect absorber based hot electron photodetection," *Nano Lett.* **14**, 3510−3514 (2014)

[49] M. W. Knight, Y. Wang, A. S. Urban, A. Sobhani, B. Y. Zheng, P. Nordlander, and N. J. Halas, "Embedding plasmonic nanostructure diodes enhances hot electron emission," *Nano Lett*. **13**, 1687−1692 (2013)

[50] K. T. Lin, H. L. Chen, Y. S. Lai, and C. C. Yu, "Silicon-based broadband antenna for high responsivity and polarization-insensitive photodetection at telecommunication wavelengths," *Nat. Commun.* **5**, 3288 (2014)

[51] B. Feng, J. Zhu, B. Lu, F. Liu, L. Zhou, and Y. Chen, "Achieving Infrared detection by all-Si plasmonic hot-electron detectors with high detectivity," *ACS Nano* **13**, 8433-8441 (2019)

[52] R. R. Lapierre, M. Robson, K. M. Azizur-Rahman, and P. Kuyanov, "A Review of III-V Nanowire Infrared Photodetectors and Sensors," *J. Phys. D: Appl. Phys.* **50**, 123001 (2017)

[53] J. Bullock, M. Amani, J. Cho, Y. Z. Chen, G. H. Ahn, V. Adinolfi, V. R. Shrestha, Y. Gao, K. B. Crozier, Y. L. Chueh, and A. Javey, "Polarization-Resolved Black Phosphorus/Molybdenum Disulfide Mid-Wave Infrared Photodiodes with High Detectivity at Room Temperature," *Nat. Photonics* **12**, 601−607 (2018)

[54] T. D. Nguyen, J. O. Kim, Y. H. Kim, E. T. Kim, Q. L. Nguyen, and S. J. Lee, "Dual-Color Short-Wavelength Infrared Photodetector Based on InGaAsSb/GaSb Heterostructure," *AIP Adv*. **8**, 025015 (2018)

[55] K. Wu, Y. Zhan, C. Zhang, S. Wu, and X. Li, "Strong and highly asymmetrical optical absorption in conformal metal-semiconductor-metal grating system for plasmonic hot-electron photodetection application," *Sci. Rep*. **5**, 14304 (2015)

[56] T. Gong, and J. N. Munday, "Angle-independent hot carrier generation and collection using transparent conducting oxides," *Nano Lett.* **15**, 147–152 (2015)

[57] F. P. Garcia de Arquer, A. Mihi, and G. Konstantatos, "Large-area plasmonic-crystal hot-electron based photodetectors," *ACS Photonics* **2**, 950–957 (2015)

[58] J. B. Chou, X-H. Li, Y. Wang, D. P. Fenning, A. Elfaer, J. Viegas, M. Jouiad, S-H. Yang, and S-G. Kim, "Surface plasmon assisted hot electron collection in wafer-scale metallic-semiconductor photonic crystals," *Opt Express* **24**, A1234–1244 (2016)

[59] H. Harutyunyan, A. B. Martinson, D. Rosenmann, L. K. Khorashad, L. V. Besteiro, A. O. Govorov, and G. P. Wiederrecht, "Anomalous ultrafast dynamics of hot plasmonic electrons in nanostructures with hot spots," *Nat Nanotechnol* **10**, 770–774 (2015)

[60] T. Yu, C. Zhang, H. Liu, J. Liu, K. Li, L. Qin, S. Wu and X. Li, "Planar, narrowband, and tunable photodetection in the near-infrared with Au/TiO_2 nanodiodes based on Tamm plasmons," *Nanoscale* **11**, 23182-23187 (2019)

[61] C. Zhang, K. Wu, V. Giannini, and X. Li, "Planar hot-electron photodetection with Tamm plasmons," *ACS Nano* **11**, 1719-1727 (2017)

[62] C. Zhang, K. Wu, Y. Zhan, V. Giannini, and X. Li, "Planar microcavity-integrated hot-electron photodetector," *Nanoscale* **8**, 10323-10329 (2016)

[63] Z. Wang, J. K. Clark, Y-L. Ho, and J. J. Delaunay, "Hot-electron photodetector with wavelength selectivity in near-infrared via Tamm plasmon," *Nanoscale* **11**, 17407-17414 (2019)

[64] L. S. Jung, C. T. Campbell, T. M. Chinowsky, M. N. Mar, S. S. Yee, Langmuir 1998, 14, 5636.

[65] A. J. Haes, S. Zou, G. C. Schatz, R. P. Van Duyne, J. Phys. Chem. B 2004, 108, 109.

[66] Optical Refractive Index Sensors with Plasmonic and Photonic Structures: Promising and Inconvenient Truth

[67] E. Kretschmann, H. Raether, Z. Naturforsch. A 1968, 23, 2135.

[68] A. Otto, Z. Phys. 1968, 216, 398.

[69] J. Homola, Chem. Rev. 2008, 108, 462.

[70] J. Homola, Surface Plasmon Resonance Based Sensors, Springer, New York 2006.

[71] R. Jorgenson, S. Yee, Sens. Actuators B 1993, 12, 213.

[72] A. U. Khan, S. Zhao, G. Liu, J. Phys. Chem. C 2016, 120, 19353.

[73] Y. Zhang, D. E. Charles, D. M. Ledwith, D. Aherne, S. Cunningham, M. Voisin, W. J. Blau, Y. K. Gun'ko, J. M. Kelly, M. E. Brennan-Fournet, RSC Adv. 2014, 4, 29022.

[74] W. Kubo, S. Fujikawa, Nano Lett. 2011, 11, 8.

[75] T. Sannomiya, O. Scholder, K. Jefimovs, C. Hafner, A. B. Dahlin, Small 2011, 7, 1653.

[76] A. A. Yanik, A. E. Cetin, M. Huang, A. Artar, S. H. Mousavi, A. Khanikaev, J. H. Connor, G. Shvets, H. Altug, Proc. Natl. Acad. Sci. USA 2011, 108, 11784.

[77] Y. Gu, Q. Li, J. Xiao, K. Wu, G. P. Wang, J. Appl. Phys. 2011, 109, 023104.

[78] M. P. Jonsson, P. Jönsson, A. B. Dahlin, F. Höök, Nano Lett. 2007, 7, 3462.

[79] J. Prikulis, P. Hanarp, L. Olofsson, D. Sutherland, M. Käll, Nano Lett. 2004, 4, 1003.

[80] H. Im, S. H. Lee, N. J. Wittenberg, T. W. Johnson, N. C. Lindquist, P. Nagpal, D. J. Norris, S. H. Oh, ACS Nano 2011, 5, 6244.

[81] M. R. Gartia, A. Hsiao, A. Pokhriyal, S. Seo, G. Kulsharova, B. T. Cunningham, T. C. Bond, G. L. Liu, Adv. Opt. Mater. 2013, 1, 68.

[82] K. A. Tetz, L. Pang, Y. Fainman, Opt. Lett. 2006, 31, 1528.

[83] Y. Shen, X. Chen, Z. Dou, N. P. Johnson, Z. K. Zhou, X. Wang, C. Jin, Nanoscale 2012, 4, 5576.

[84] Y. Li, J. Pan, P. Zhan, S. Zhu, N. Ming, Z. Wang, W. Han, X. Jiang, J. Zi, Opt. Express 2010, 18, 3546.

[85] M. E. Stewart, N. H. Mack, V. Malyarchuk, J. A. Soares, T. W. Lee, S. K. Gray, R. G. Nuzzo, J. A. Rogers, Proc. Natl. Acad. Sci. USA 2006, 103, 17143.

[86] B. Ai, L. Wang, H. Möhwald, Y. Yu, G. Zhang, Nanoscale 2015, 7, 2317.

[87] Z. Chen, L. Liu, Y. He, H. Ma, Appl. Opt. 2016, 55, 884.

[88] J. Dostàlek, H. Vaisocherovà, J. Homola, Sens. Actuators B 2005, 108, 758.

[89] B. Sutapun, A. Somboonkaew, R. Amrit, N. Houngkamhang, T. Srikhirin, Sens. Actuators B 2011, 156, 312.

[90] B. Choi, X. Dou, Y. Fang, B. M. Phillips, P. Jiang, Phys. Chem. Chem. Phys. 2016, 18, 26078.

[91] M. Piliarik, M. Vala, I. Tichy`, J. Homola, Biosens. Bioelectron. 2009, 24, 3430.

[92] H. Gao, J.-C. Yang, J. Y. Lin, A. D. Stuparu, M. H. Lee, M. Mrksich, T. W. Odom, Nano Lett. 2010, 10, 2549.

[93] J. Guo, Z. Li, H. Guo, Opt. Express 2016, 24, 17259.

[94] S. Nair, C. Escobedo, R. G. Sabat, ACS Sens. 2017, 2, 379.

[95] J. Homola, S. S. Yee, G. Gauglitz, Sens. Actuators B 1999, 54, 3.

[96] S. K. Mishra, B. Zou, K. S. Chiang, IEEE Photonics Technol. Lett. 2016, 28, 1835.

[97] Y. Wang, H. Li, Z. Cao, T. Yu, Q. Shen, Y. He, Appl. Phys. Lett. 2008, 92, 061117.

[98] X. Wang, C. Yin, J. Sun, H. Li, Y. Wang, M. Ran, Z. Cao, Opt. Express 2013, 21, 13380.

[99] H. T. Yan, Q. Liu, Y. Ming, W. Luo, Y. Chen, Y. Q. Lu, IEEE Photonics J. 2013, 5, 4800706.

[100] E. Klantsataya, P. Jia, H. Ebendorff-Heidepriem, T. M. Monro, A. François, Sensors 2017, 17, 12.

[101] P. Chen, Y. J. He, X. S. Zhu, Y. W. Shi, Sensors 2015, 15, 27917.

[102] E. Klantsataya, A. François, H. Ebendorff-Heidepriem, P. Hoffmann, T. M. Monro, Sensors 2015, 15, 25090.

[103] M. Piliarik, J. Homola, Z. Manìkovà, J. C.ˇtyroky`, Sens. Actuators B 2003, 90, 236.

Chapter 2 : Spectrally selective photodetection and refractive index sensing in the near infrared using a Si channel-separated parallel grating structure

2.1 Introduction

2.1.1 Photodetection

Plasmonic nanostructures have received extensive attention due to their ability to increase the harvesting of incident light from free space and concentrate electromagnetic energy to nanoscale volumes through the excitation of surface plasmons (SPs). With this outstanding property, plasmonic nanostructures have been widely used to enhance the performance of optoelectronic devices, such as photocatalysis devices [1, 2], solar energy harvesting devices [3, 4], lasing devices [5, 6], imaging devices [7], monitoring devices [8], and photodetectors [9-14]. SP-based photodetectors generally have higher external quantum efficiencies and responsivities than conventional photodetectors because of the enhanced light absorption and the ability to generate hot electrons through the nonradiative decay of SPs [15, 16]. Photodetectors incorporating hot electrons are also being referred to as hot electron photodetectors. In hot electron photodetectors, hot electrons with energies exceeding the barrier height can cross the barrier before thermalization and be injected into the conduction band of the semiconductor/insulator, resulting in a photocurrent that can be detected with an external circuit. The most frequently discussed configurations of hot electron photodetectors are metal-insulator-metal (MIM) configuration, metal-semiconductor (MS) configuration and metal-semiconductor-metal (MSM) configuration. For MIM configuration, one of its biggest drawbacks comes from the low efficiency of hot electron generation and propagation across the high M/I barrier [16, 17]. Due to the high M/I barrier, the probability of hot electrons excited by low-frequency photons crossing the barrier is low, and this limits the

photodetection in the ultraviolet (UV) and visible ranges [16, 18-20]. The emergence of MS and MSM configurations has resolved the high barrier problem as they have a relatively lower barrier height compared to the MIM configuration. Hot electron photodetectors with these two configurations overcome the native limitations from the bandgap of semiconductors, enabling the selective detection of photons whose energy ($h\nu$) is higher than the barrier height (φ_b) but lower than the bandgap (E_g) (i.e., $\varphi_b < h\nu < E_g$). Therefore, hot electron photodetectors with MS and MSM configurations are capable of achieving photodetection at sub-bandgap energies of semiconductors, extending the photodetection to the near infrared (NIR) range [12, 13, 21, 22].

In hot electron photodetectors with MS configurations, such as antennas [21, 22], metamaterial perfect absorbers [23], Au gratings [24, 25], nanowires [26-28], waveguides [29, 30], and deep-trench/ thin-metal structures [31], hot electrons are generated in a single metallic layer and produce a unidirectional photocurrent. In MSM configurations, the semiconductor component is commonly sandwiched between two opposite metallic layers, such as top/bottom or left/right metallic layers, resulting in hot electrons being generated in both metals and transporting in opposite directions. A net photocurrent in the MSM configuration can be generated by creating an asymmetrical absorption in the two metallic layers by using different structures or different materials. Another way to obtain a net photocurrent is to apply a bias voltage to produce asymmetrical Schottky junctions in the structure. An increasing number of hot electron photodetectors with MSM configurations have been reported in recent years, including Au nanodipole arrays [32], waveguide-based Al/p-Si/Cu structure [33], and conformal Au/ZnO/Au grating [34]. In both MS and MSM configurations, the grating-based structures usually offer strong light confinement and the resonant wavelength is readily tuned over a wide range by adjusting the period of the structure or the incident angle of light. In this chapter, we propose a Si channel-separated parallel grating structure (MSM configuration) by integrating a subwavelength Au grating with Si channel arrays. The structure takes advantage of the MSM configuration and combines the features of plasmonic gratings with hot electrons for spectrally selective

photodetection at telecommunication wavelengths. The insights gained from this study can help aid the realization of ultracompact and efficient hot electron photodetectors.

2.1.2 Refractive index sensing

The refractive index (RI) sensor with plasmonic nanostructures has attracted intensive attentions since the excited surface plasmons are sensitive to the minute variation of the refractive index of the surrounding dielectric medium, which enables it to be a label-free biochemical sensor with extremely high sensing performances [35-39]. The localized surface plasmon resonance (LSPR) based sensor and surface plasmon resonance (SPR) based sensor are two kinds of RI sensors with plasmonic nanostructures, basing on whether the excited plasmon is localized to a metallic nanostructure or oscillates at the metal/dielectric interface. In the past decades, LSPR-based RI sensors have drawn much attention with the advantages of simplicity, low-cost and readiness for integration. However, LSPR-based sensors typically have a broad bandwidth and exhibit a low figure of merit (FOM), a gauge for the minimal detectable variation of the refractive index, due to the strong radiative damping. This shortage has triggered substantial efforts aiming to enhance the performances of LSPR-based sensors. Some efforts have been payed to reduce the full-width at half-maximum (FWHM) of LSPR-based sensors and therefore increase the FOM values [40-43]. One effective approach is to couple the LSPR with other plasmon mode which owns a smaller FWHM, like the split ring resonator-bar structure [44], nanocross-nanobar structure [45], cavity-coupled nanorod array [46] and plasmonic gold mushroom array [47]. Another reported scheme is generating lattice plasmon resonances whose FWHM is below 10 nm using periodically metallic nanoparticle arrays [48-50]. The other method is to increase the interface between the metallic nanostructure and the surrounding medium as much as possible, for example, lifting the metallic nanoparticles above the substrate by nanopillars to decrease the overlap between the substrate and the enhanced field [51]. Despite the aforementioned efforts, there is still a long way for the LSPR-based RI sensors to outpace the SPR-based RI sensors [52,53]. The SPR-based RI sensors typically generate an evanescent field due to the collective oscillations of electrons at the metal-dielectric interface. The rapid decay of evanescent field enables the

SPR-based RI sensors exploit a high sensitivity to the minute change of refractive index of the surrounding medium. SPR-based RI sensors commonly utilize a standard prism that couples to a metallic surface, like the Kretschmann configuration, or diffraction grating to compensate the momentum mismatch to excite the SPR. The prism-excited SPR-based RI sensors have been deeply studied in the past years [54-56] and are commercialized nowadays with a considerable sensitivity and FOM values. The diffraction grating-excited SPR is also substantial utilized in the optical fiber grating RI sensors [57-59] and the metallic grating RI sensors [60-64]. But the sensitivity and FOM values of the diffraction grating-excited SPR RI sensors are much lower compared with prism-excited SPR-based RI sensors [65,66]. To improve the sensing performance of the diffraction grating-excited SPR sensors, we propose a Si channel-separated parallel grating structure with the excitation of channel enhanced SPP mode in this chapter. The proposed structure exhibits a sensitivity as high as 775 nm/refractive index unit (RIU) with the FOM approaching 48, demonstrating the potential as a qualified RI sensor.

2.2 Experiment and simulation results

2.2.1 Structure diagram and fabrication process

Figure 2.1(a) shows a schematic diagram of the proposed Si channel-separated parallel grating structure, which consists of an n-type Si substrate and Au slabs separated by Si channels. A bias voltage is applied on the leftmost and rightmost Au slabs of the grating. The cross-section of one periodic unit of the structure is shown in figure 2.1(b). The width (w) and height (h) of the Si channel, the thickness of the Au slab (t), the period of the structure (p), and the incident angle (θ) of light are all indicated. A linear polarizer is used to polarize normally incident light either along the direction of the Si channels (transverse electric, TE) or orthogonal to them (transverse magnetic, TM). The dimensions of the structure are w = 270 nm, h = 200 nm and t = 40 nm. p ranges from 820 to 880 nm. The fabrication process of the structure is illustrated in figure 2.1(c). First, the electron-beam (EB) resist (ZEP520A, Zeon Corporation, Tokyo, Japan) was coated on the Si substrate by spin coating.

Subsequently, the coated EB resist was patterned through EB lithography (F7000S-VD02, Advantest, Tokyo, Japan). Following this, a reactive ion etching (RIE) system (Plasmalab 80 Plus, Oxford Instruments, Abingdon-on-Thames, UK) was used to etch the Si substrate. A 2-nm thick Ti layer was deposited before the Au deposition using EB evaporation (Peva-400E, Advanced System Technology Co., Tokyo, Japan). The function of the Ti layer is to increase the adhesion between the Si substrate and the Au layer. Without an adhesion layer the Au layer may detach easily from the Si substrate during the lift-off process. Lastly, the EB resist and the top Au layer were removed by lift-off in a dimethylacetamide ultrasonic bath at 60℃.

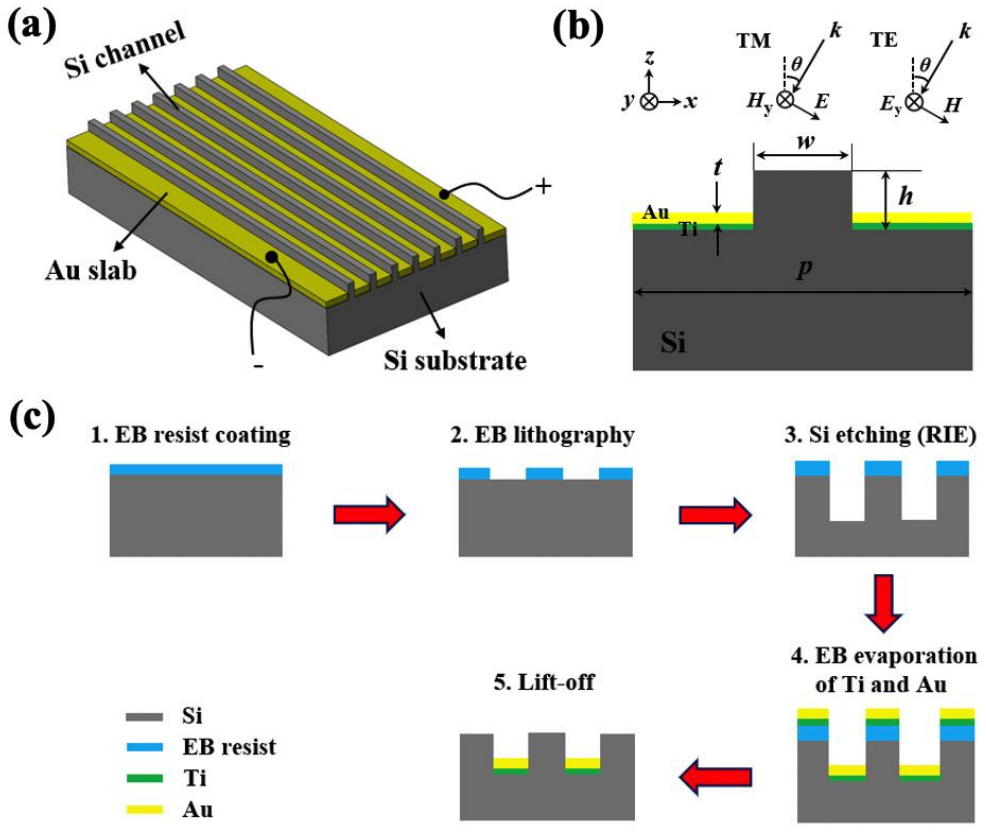

Figure 2.1 (a) The schematic diagram of the Si channel-separated parallel grating structure. The bias voltage is applied to the leftmost and rightmost of the Au slabs. (b) The illustration of a periodic unit of the cross-section of the structure. The width and height of the Si channel are *w* and *h*, respectively. The thickness of the Au slab is *t*, the period of the structure is *p* and the incident angle of light is θ. *k* represents the Poynting vector of incident light, *E*

represents the electric field and *H* represents the magnetic field. (c) The fabrication process for the Si channel-separated parallel grating structure, including EB resist coating, EB lithography, Si etching by RIE, Au deposition by EB evaporation, and lift-off.

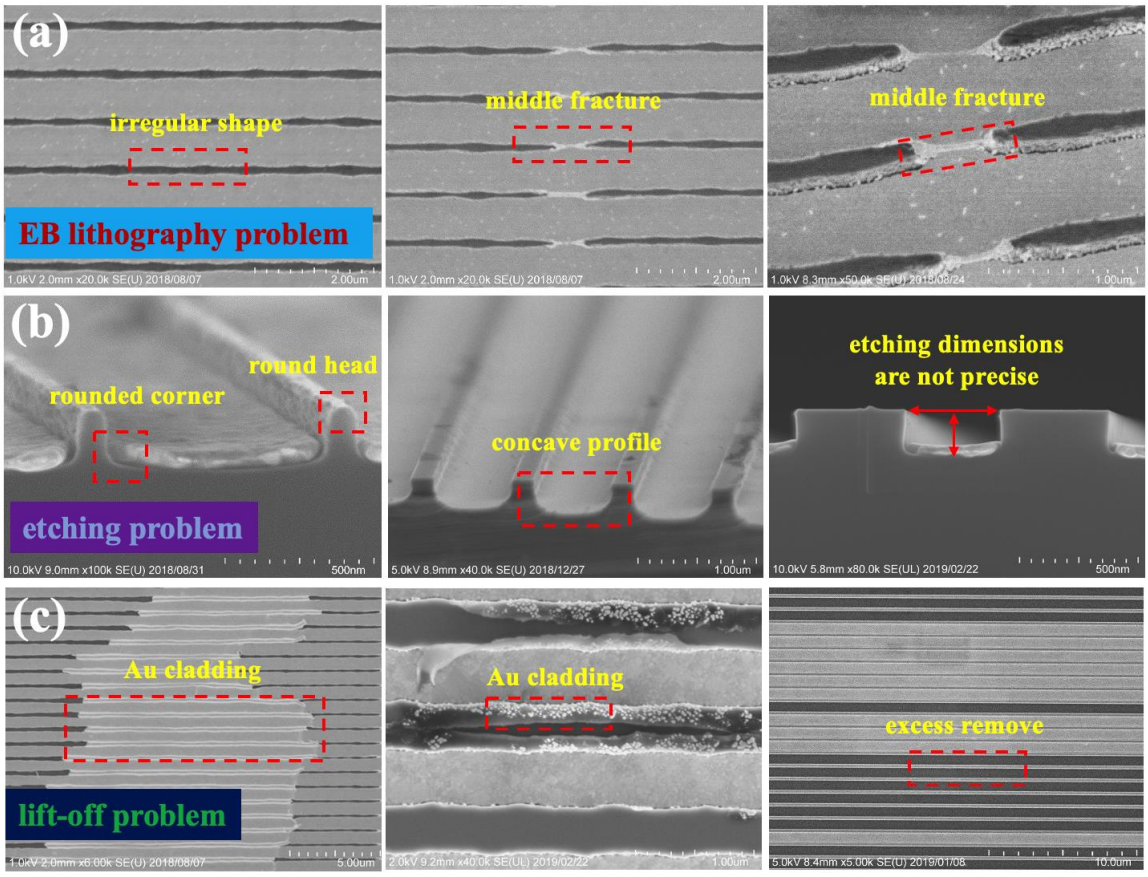

Figure 2.2 SEM images for the fabricated Si channel-separated parallel grating structure with different imperfections: (a) EB lithography problem, (b) etching problem and (c) lift-off problem.

Due to the incorrect operations and inaccurate parameters, some unsatisfying samples with different imperfections are fabricated as shown in figure 2.2. Figure 2.2(a) shows the scanning electron microscope (SEM) images of the fabricated samples that have EB lithography problems. It is seen that the Si channels are in irregular shapes and the channel width is much narrower than the designed value (280 nm). The middle fracture even occurs

in some Si channels. The RIE technique also brings etching problems to the fabrication, such as the formations of round head in the top of Si channel and rounded corners in the bottom. The etching depth and width of Si are also hard to control. The EB resist and Au layer on the top of Si channels are not completely removed and leads to Au cladding if the lift-off process is not accurately performed, as show in figures 2.2 (c). Moreover, inappropriate lift-off can lead to excess remove of Au from the substrate.

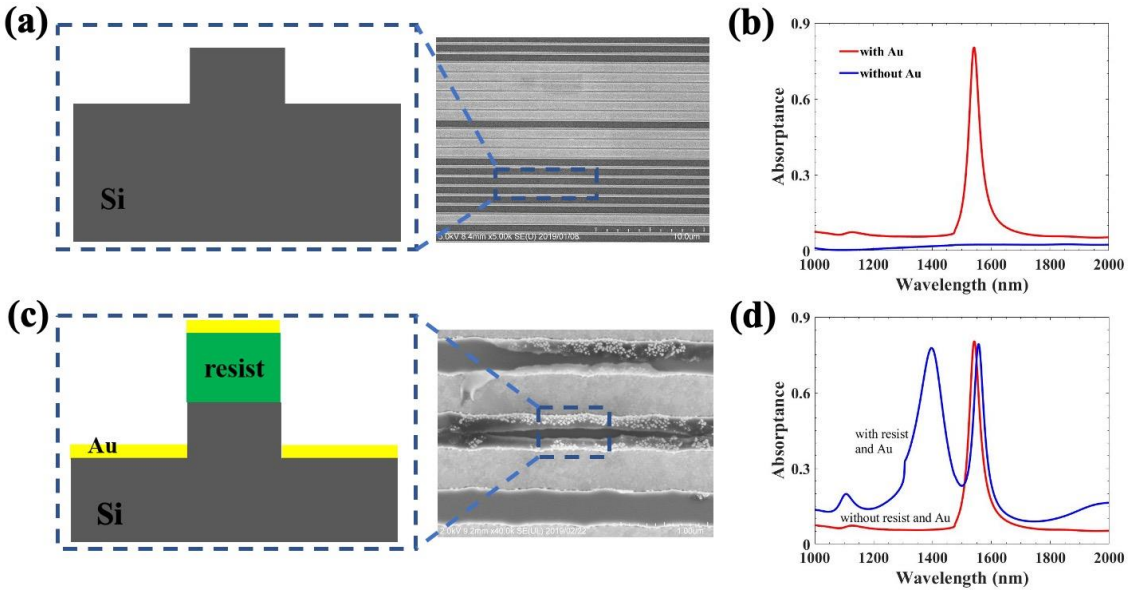

Figure 2.3 (a) left: schematic diagram shows some Au layers are excessively removed from the substrate after lift-off, right: the corresponding SEM image, (b) influence of removing Au layer from the substrate on structure absorptance, (c) left: schematic diagram shows that both the EB resist and Au layer are kept on the top of Si channels after lift-off, right: the corresponding SEM image, (d) influence of the residual EB resist and Au layer on top of Si channels after lift-off on structure absorptance.

The influences of these imperfections on the structure absorptance are further investigated. Figure 2.3(a) illustrates the schematic diagram (left) and SEM image (right) showing some Au layers are excessively removed from the substrate after inappropriate lift-off. The influence of removing Au layer from the substrate on structure absorptance is shown

in figure 2.3(b). The absorptance spectrum exhibits a narrowband and high absorptance at the resonant wavelength for the structure with Au layer between adjacent Si channels. In contrast, the absorptance spectrum exhibits a very low absorptance (almost 0) across the wavelength range of 1000-2000 nm for the structure without Au layer between adjacent Si channels. The schematic diagram (left) and SEM image (right) showing the residual EB resist and Au layer on top of Si channel after lift-off is given in figure 2.3(c). The influence of the residual EB resist and Au layer on structure absorptance is shown in figure 2.3(d). The absorptance peak corresponding to the structure with the residual EB resist and Au layer exhibits a small redshift compared with the structure without the residuals, and an another absorptance peak with a broad bandwidth occurs at a short wavelength.

During the EB evaporation of Au, the Au layer is easily deposited on the sidewalls of Si channels, as shown in the schematic diagram (left) and SEM image (right) of figure 2.4(a). The influence of the thickness of Au layer on the sidewalls of Si channel on structure absorptance is investigated as shown in figure 2.4(b). The absorptance spectrum exhibits a narrowband and high absorptance at the resonant wavelength for the structure with no deposition (0 nm) of Au layer on the sidewalls of Si channel. When the thickness of Au layer on the sidewalls of Si channel increases to 5 nm and 10 nm, the peak absorptance shows a rapid decrease and the bandwidth increases. Additionally, the resonant wavelength shows a small blueshift with the increase of the thickness of Au layer on the sidewalls. Actually, the deposition of Au layer on the sidewalls of Si channels mainly attribute to the use of all-directional deposition techniques, such as the magnetron sputtering, as shown in figure 2.4(c). Since the emitted metal atoms are generated through the collision with the incident argon ions in magnetron sputtering, these metal atoms reach the substrate with all directions and lead to a nondirective deposition. In contrast, the metal atoms can achieve unidirectional deposition if we use the electron-beam evaporation technique, as shown in figure 2.4(d). We can avoid the deposition of Au layer on the sidewalls of Si channels when the sample is put right underneath the target, as shown in position *a* in the figure.

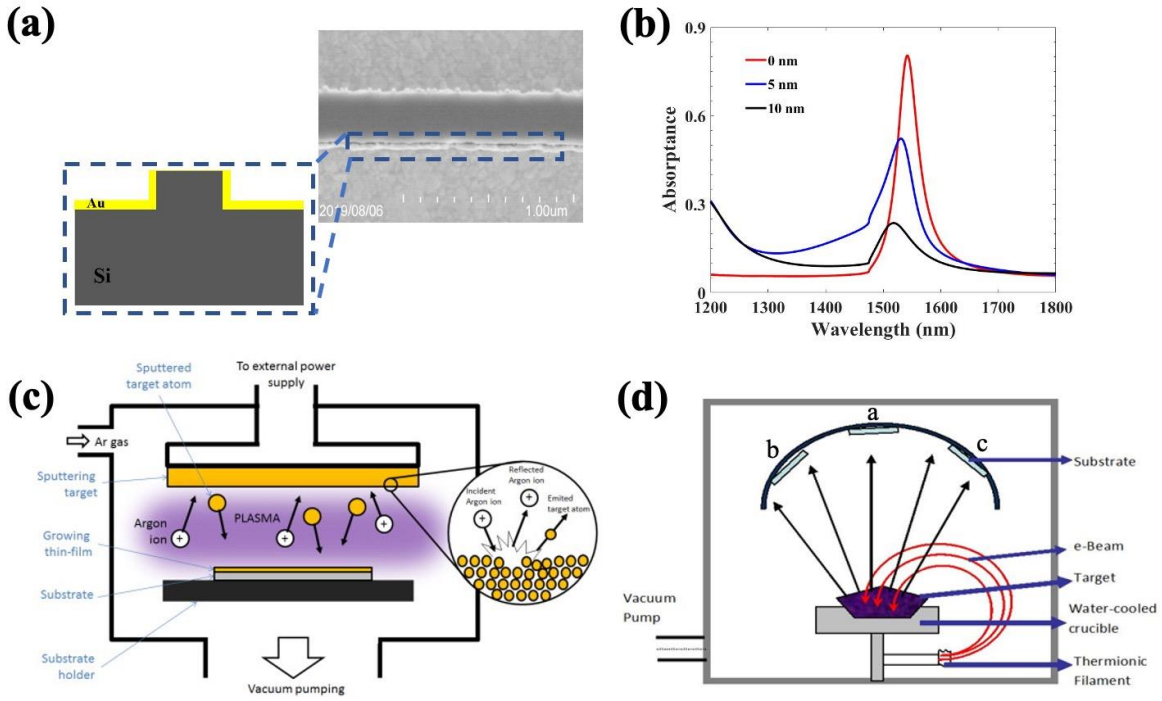

Figure 2.4 (a) Schematic diagram (left) and SEM image (right) shows the undesired deposition of Au layers on the sidewalls of Si channel. (b) Influence of the thickness of Au layer on the sidewalls of Si channel on structure absorptance. (c) Schematic diagram of the magnetron sputtering. (d) Schematic diagram of the electron-beam evaporation.

The fabricated sample with small imperfections is shown in figure 2.5. Figures 2.5(a) and (b) show the top-view of the left and right parts of the structure, respectively. Figure 2.5(c) displays the magnified top-view of the structure. The tilted magnified top-view of the structure is shown in figure 2.5(d).

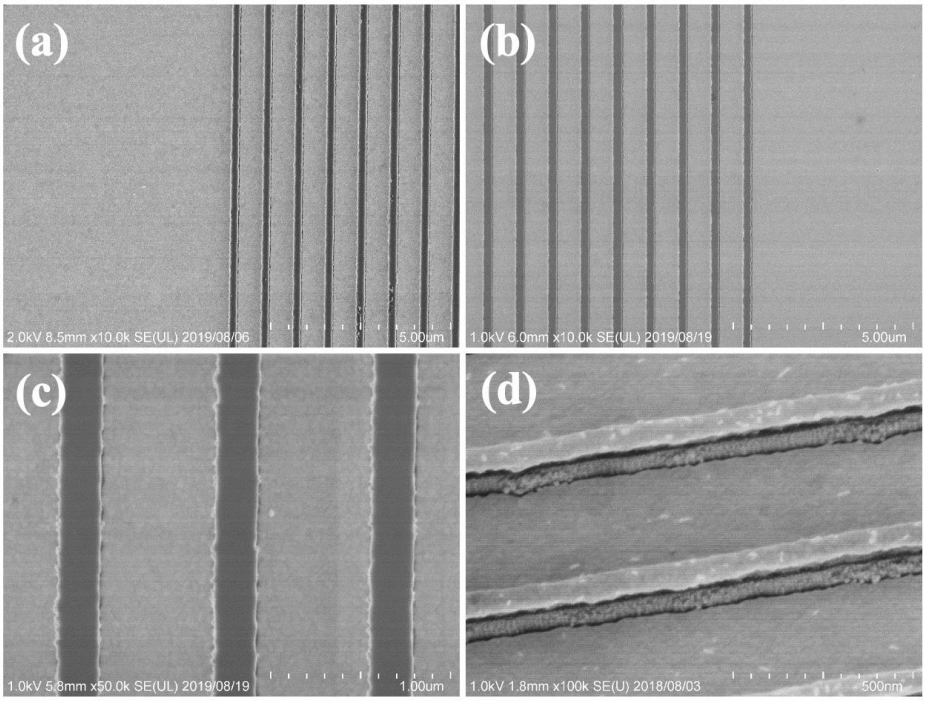

Figure 2.5 SEM images for the fabricated Si channel-separated grating structure with small imperfections: (a) top-view of the left part of the structure, (b) top-view of the right part of the structure, (c) magnified top-view of the structure and (d) magnified tilted view of the structure.

2.2.2 Optical properties

2.2.2.1 Strong light confinement and field enhancement due to the SPP mode

To investigate the optical properties of the Si channel-separated parallel grating structure, the simulated reflectance (R_{sim}), transmittance (T_{sim}) and absorptance (A_{sim}) spectra of the structure, computed with the rigorous coupled-wave analysis (RCWA, DiffractMOD, Rsoft Design Group, Ossining, NY, USA), are first examined, as shown in figure 2.6(a). The light is normally incident with TM-polarization, and the period of the structure (p) is 840 nm. The absorptance peak (point B) reaches 0.8 at the resonant wavelength of 1524 nm. The measured reflectance (R_{exp}) spectrum, characterized by the FT-IR spectrometer (VIR-300, JASCO, Tokyo, Japan), exhibits a full-width at half maximum (FWHM) as narrow as 24 nm. The

measured and simulated reflectance spectra are not perfectly matched due to imperfections in the fabrication, including the undesired deposition of a thin Au layer (about 2 nm in thickness) on the sidewalls of Si channels during the EB evaporation, the formations of trapezoidal sidewalls and bottom rounded corners in Si channels during the Si etching, etc. Figure 2.6(b) illustrates the definition of FWHM, which is the width of a reflectance spectrum measured between two points on the reflectance-axis with the amplitude of $(R_{max} + R_{min}) / 2$, where R_{max} and R_{min} represent the maximum and minimum reflectance, respectively. In order to investigate the origin of the strong and narrowband absorption of the structure at the resonant wavelength (points B), the simulated electric field distributions in the *x*- (E_x) and *z*-direction (E_z), computed with the finite-difference time-domain technique (FullWave, Rsoft Design Group, Ossining, NY, USA), are provided in figure 2.6(c). The perfectly matched layer (PML) boundary conditions are applied in the *z*-direction at the top and bottom of the simulation domain, and the periodic boundary condition is applied in the *x*-direction. For comparison purposes, the simulated electric field distributions at point A (λ = 1300 nm), as defined in figure 2.6(a), are also given in figure 2.6(c). It is seen that the electric fields of E_x and E_z are both quite weak at the non-resonant wavelength (point A). In contrast, the electric field at the resonant wavelength (point B) exhibits strong enhancements at the corners of the Au slabs and the Au/Si interface as a result of the excitation of the surface plasmon polariton (SPP) at the Au/Si interface.

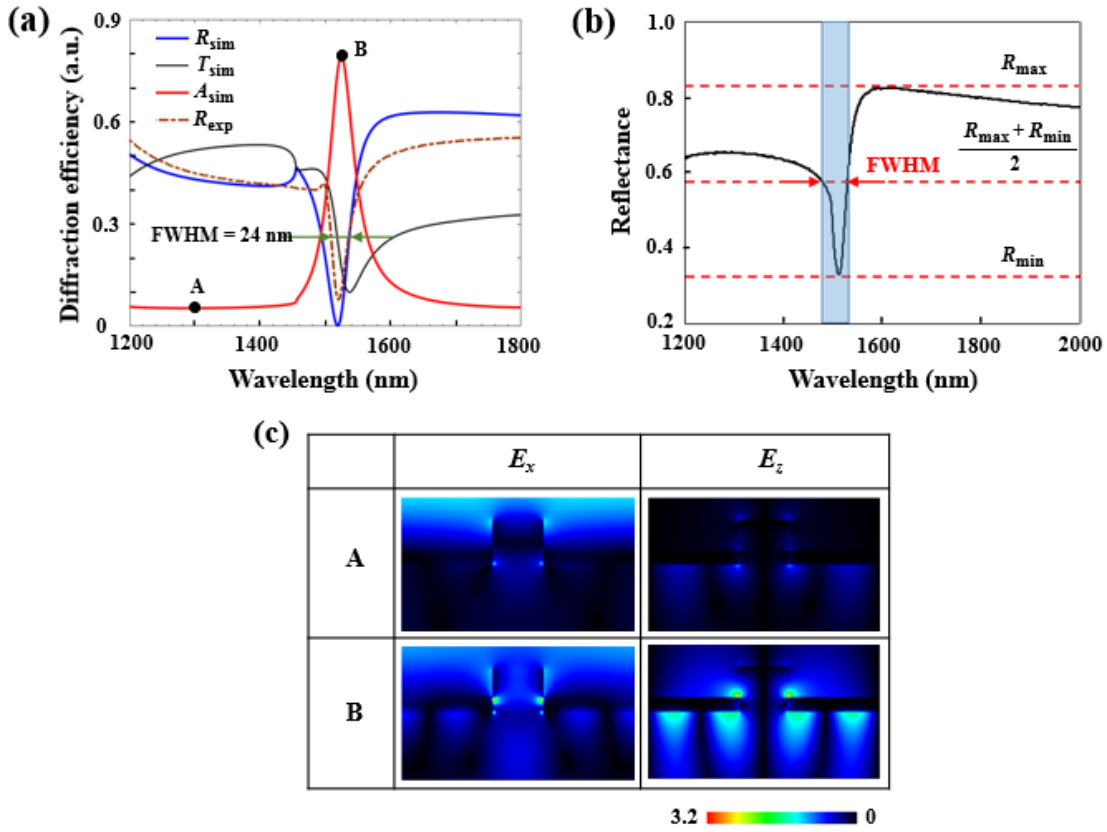

Figure 2.6 The optical properties of the Si channel-separated parallel grating structure. The light is normally incident and TM-polarized, and the period of the structure is 840 nm. (a) The simulated reflectance (R_{sim}), transmittance (T_{sim}) and absorptance (A_{sim}) spectra of the structure. The measured reflectance (R_{exp}) spectrum is represented by the brown dashed line. (b) The definition for FWHM. (c) The simulated electric field distributions in the *x*- (E_x) and *z*-direction (E_z) for points A and B, as defined in (a).

To study the properties of the SPP mode excited at the Au/Si interface, the dependence of reflectance on the period of the structure and the incident angle of light are investigated. The simulated (Sim) and measured (Meas) reflectance variation with light wavelength under different periods (p) of the structure is given in figure 2.7(a). Both the simulated and measured reflectance dip exhibit a redshift when the period increases from 820 to 880 nm, demonstrating the facile tunability of the resonant wavelength. This property is further demonstrated in figure 2.7(b), which shows the simulated reflectance variation with light

wavelength and period of the structure. The resonant wavelength of the SPP mode redshifts linearly with the period, matching well with the experiment result. Figure 2.7(c) shows the simulated (Sim) and measured (Meas) reflectance spectra at different incident angles (θ) of light. Only one reflectance dip occurs at the resonant wavelength when the light is normally incident (0°), while the reflectance dip splits when the incident angle increases to 3° and 6°. Moreover, the distance between the two dips increases with the incident angle. This splitting of the resonance is due to the strong angular dependence of the SPP mode, which is indicated in figure 2.7(d) where the simulated reflectance variation with light wavelength and the incident angle of light is shown. The reflectance splits when the incident angle increases from 3° to 25°, and the resonance gradually becomes weaker and lastly disappears when the incident angle is even larger.

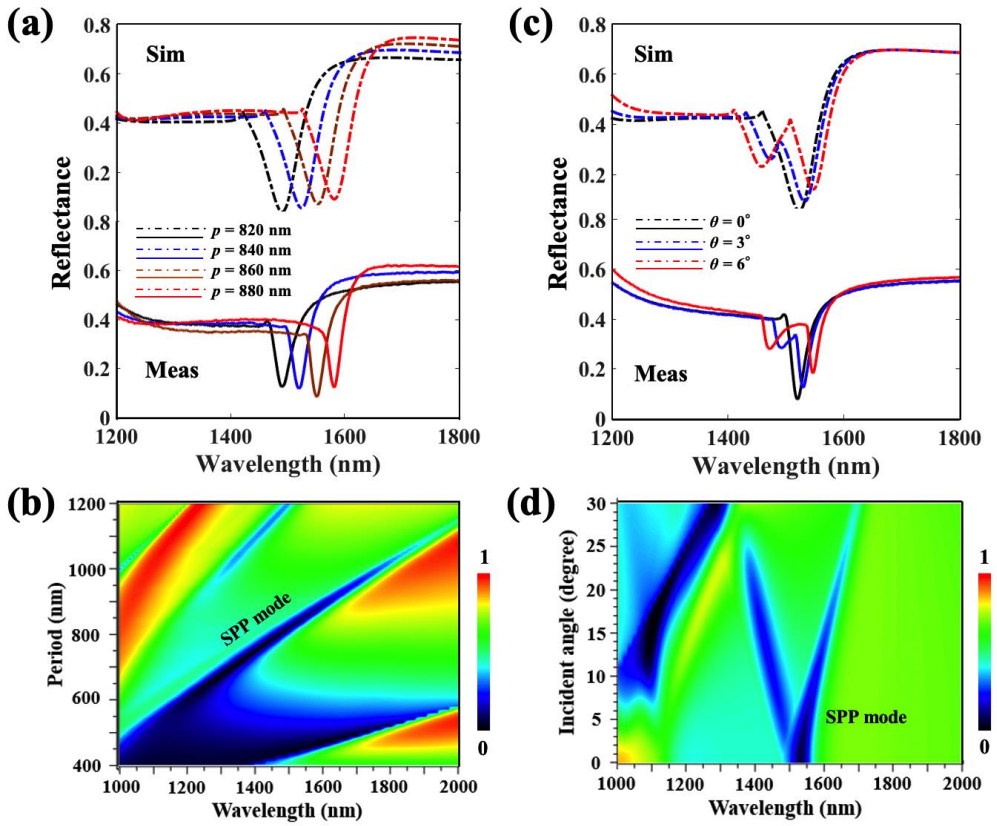

Figure 2.7 The optical properties of the Si channel-separated parallel grating structure. The light is TM-polarized. (a) The measured (Meas) and simulated (Sim) reflectance spectra for

different periods (p) of the structure. The light is normally incident. (b) The simulated reflectance variation with light wavelength and period of the structure. The light is normally incident. (c) The measured (Meas) and simulated (Sim) reflectance spectra at different incident angles (θ) of light. The period of the structure is 840 nm. (d) The simulated reflectance variation with light wavelength and the incident angle of light. The period of the structure is 840 nm.

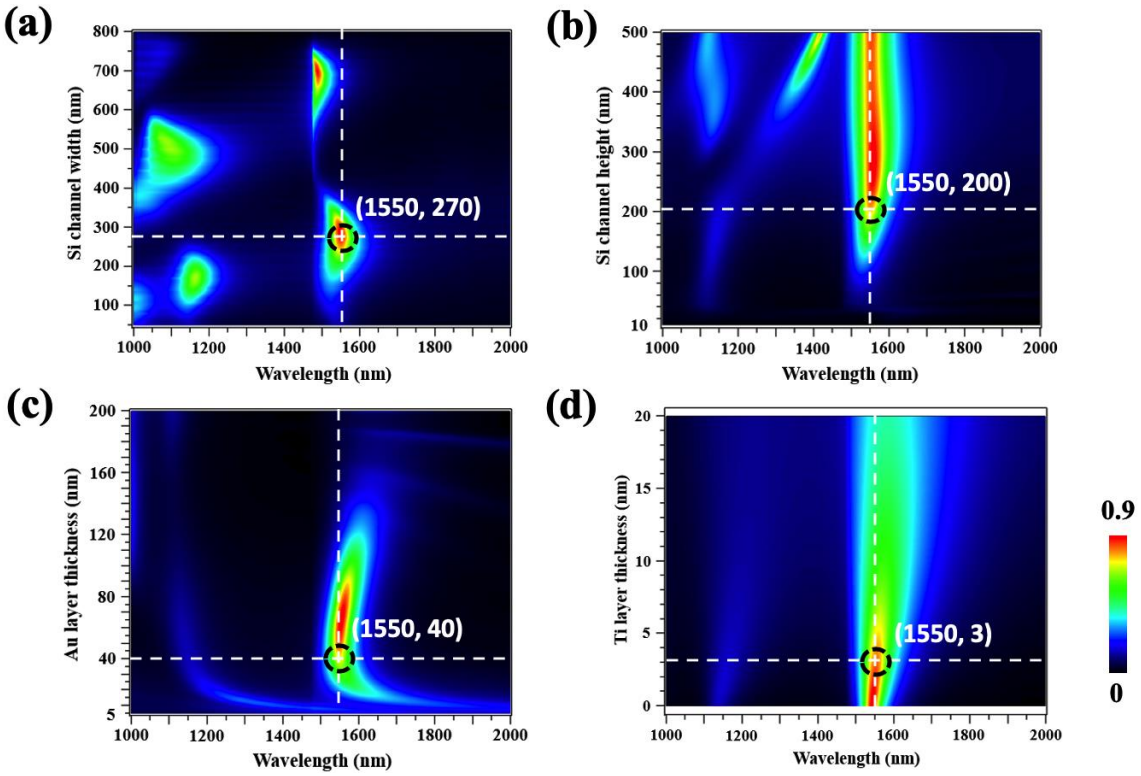

Figure 2.8 (a) The simulated absorptance variation with Si channel width (w) and light wavelength. (b) The simulated absorptance variation with Si channel height (h) and light wavelength. (c) The simulated absorptance variation with Au layer thickness (t) and light wavelength. (d) The simulated absorptance variation with Ti layer thickness and light wavelength. Unless otherwise noted, the structure dimensions are w = 270 nm, h = 200 nm and p = 860 nm. The light is normally incident with TM-polarization.

The influence of the structure dimensions on the absorptance is also investigated. The effect of Si channel width (*w*) on the structure absorptance is shown in figure 2.8(a). The structure exhibits strong plasmon resonances at the resonant wavelength of 1500 nm when *w* is 700 nm, and 1550 nm when *w* is 270 nm. Since the absorptance changes rapidly with the variation of *w*, it asks for a strict control of *w* in the fabrication. The influence of the Si channel height (*h*) on the structure absorptance is shown in figure 2.8(b). The structure exhibits a strong plasmon resonances when *h* exceeds 200 nm. Moreover, the resonant wavelength shows no shift with the increase of *h*. According to the simulated absorptance variation with Au layer thickness (*t*) and light wavelength as shown in figure 2.8(c), the strong plasmon resonances are observed when the Au layer thickness ranges between 40 to 90 nm. Additionally, the resonant wavelength slightly shifts with an increase of the Au layer thickness. The influence of the Ti layer thickness on the absorptance is shown in figure 2.8(d). The increase of Ti layer thickness not only weakens the plasmon resonances but also broadens the resonance bandwidth. According to the absorptance variation with the sweep of the structure dimensions, it demonstrates that the optimized parameters for the generation of plasmon resonances at the wavelength of 1550 nm are: w = 270 nm, h = 200 nm, t = 40 nm and p = 860 nm.

2.2.2.2 Tunable resonant wavelength for refractive index sensing

The Si channel-separated parallel grating structure also exhibits other optical behaviors besides the SPP mode. Figure 2.9(a) shows the reflectance variation with light wavelength and incident angle of light in air using the rigorous coupled wave analysis (RCWA). Unless otherwise noted, the structure dimensions are h = 150 nm, t = 65 nm, p = 860 nm and w ranges from 185 nm to 225 nm in this section, and the light is normally incident with TM-polarization. According to the reflectance variation and the electric field distribution (further clarified in figure 2.9(c)), the channel enhanced SPP mode propagating along the Au/air interface, channel mode, the coupling of SPP mode and channel mode, and the SPP mode propagating along the Au/Si interface are observed. Point A_1 is defined at the channel enhanced SPP mode propagating along the Au/air interface with the resonant wavelength

around 830 nm under normal incidence. Point A_2 is defined at the channel mode with the resonant wavelength around 1150 nm under normal incidence. Point A_3 defined at the SPP mode with the resonant wavelength around 1520 nm under normal incidence. Point A_4 is defined at the coupling of SPP mode and channel mode with the resonant wavelength around 975 nm under the incident angle of 3°. The measured reflectance spectra for different incident angles of light in air for the structure are shown in figure 2.9(b). The reflectance dip A_1 (λ = 850 nm), dip A_2 (λ = 1100 nm) and dip A_3 (λ = 1514 nm) are observed when the incident angle is 0°, which match well with the simulation results shown in figure 2.9(a). The reflectance dip A_4 occurs at the resonant wavelength around 980 nm when the incident angle of light increases to 3° and 6°. Additionally, dip A_1 shows a blueshift, dip A_2 nearly keeps stable and dip A_3 splits when the incident angle of light increases from 0° to 6°. The measured reflectance spectrum matches well with the simulation result for the incident angle of 0° and 3°, as illustrated in figure 2.9(c) and (d), respectively.

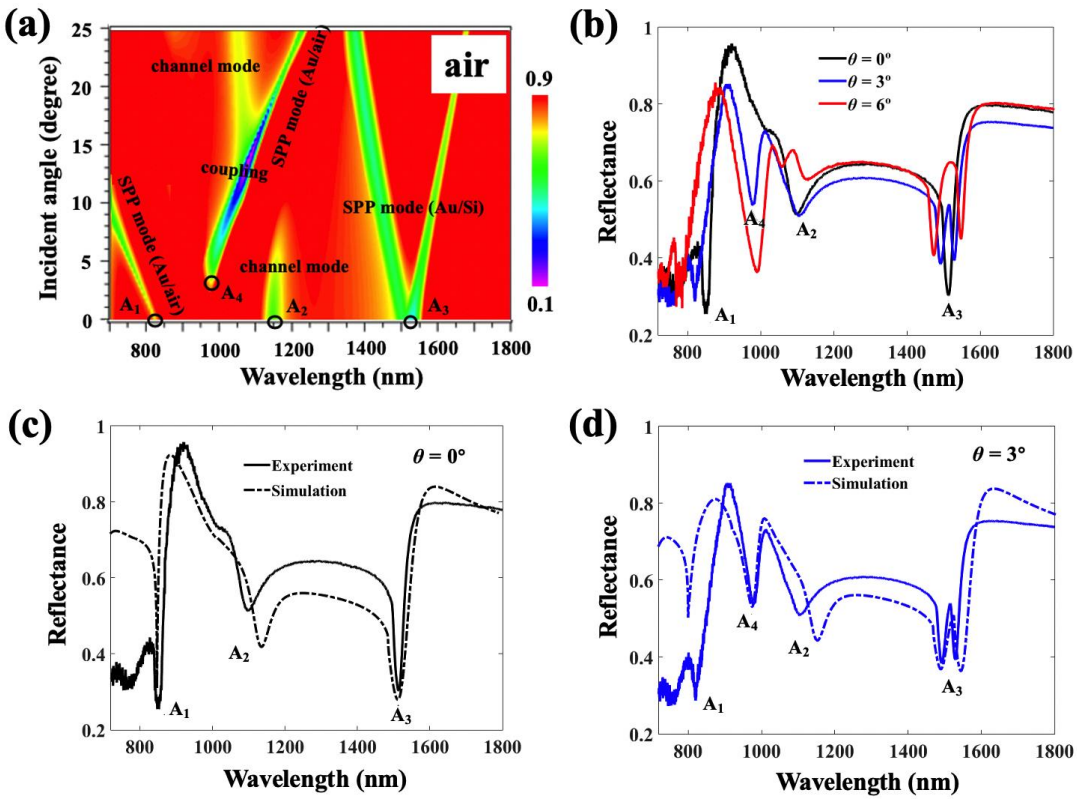

Figure 2.9 The optical properties of the Si channel-separated parallel grating structure for the structure dimension of h = 150 nm, t = 65 nm, p = 860 nm and w = 185 nm in air. The light is normally incident with TM-polarization. (a) The simulated reflectance variation with light wavelength and the incident angle of light. The surrounding medium is air. (b) The measured reflectance spectra for different incident angles of light. The experimental and simulated reflectance spectra for the incident angle (θ) of (c) 0° and (d) 3°.

To demonstrate the potential of the Si channel-separated parallel grating structure for the application of refractive index sensing, the simulated reflectance variation with light wavelength and the incident angle of light in deionized (DI) water is first investigated, as shown in figure 2.10(a). In comparison with the reflectance variation in air (figure 2.9(a)), the resonant wavelength corresponding to the channel enhanced SPP mode propagating along the Au/water interface (point A_1) and the coupling of SPP mode and channel mode (point A_4) in DI water both exhibit a redshift. While the SPP mode propagating along the Au/Si interface (point A_3) shows no shift when the surrounding medium changes from air to DI water. The channel mode corresponding to point A_2, as shown in figure 2.9(a), disappears when the surrounding medium turns to DI water. Point A_0 is defined at the non-resonant wavelength (λ = 1700 nm) with normal incidence for reference. The measured reflectance spectra for incident angle of 0°, 3° and 6° in DI water are shown in figure 2.10(b), matching well with the simulation results shown in figure 2.10(a). Two reflectance dips (points A_1 and A_3) are observed when light is normally incident (θ = 0°). When the incident angle of light increases to 3° and 6°, the reflectance dip A_3 splits and the reflectance dip A_4 appears. The reflectance dip A_1 disappears with the increase of incident angle of light due to the decrease of light confinement.

In order to further unveil the plasmon resonance conditions in the structure when the surrounding medium turns to DI water, the electric field distributions in x- (E_x) and z-direction (E_z) for points A_0, A_1, A_3 and A_4 are calculated by the FDTD technique, as shown in figure 2.10(c). At non-resonant wavelength (point A_0), the electric field E_x and E_z are both quite weak. For point A_1, the simulated electric field distribution demonstrates the presence

of SPP mode propagating along the Au/water interface. Since the electric filed is further enhanced by the Si channel, the plasmon mode corresponding to point A_1 is defined as channel enhanced SPP mode. Since the electric field is strongly enhanced at the Au/water interface, the reflectance dip A_1 is likely sensitive to the variation of the surrounding medium. The electric field distribution corresponding to point A_3 exhibits strong field enhancements at the corners of the Au slabs and the Au/Si interface due to the excitation of SPP mode propagating along the Au/Si interface. Since the field enhancement at the Au/water interface is weak at this mode, reflectance dip A_3 tends to be insensitive to the variation of the surrounding medium. For point A_4, the electric field is strongly enhanced at the top-surface of the Si channel and the Au/water interface due to the coupling of channel mode and SPP mode propagating along the Au/water interface. The reflectance dip A_4 is also likely sensitive to the variation of the surrounding medium since the electric field is strongly enhanced at the Au/water interface.

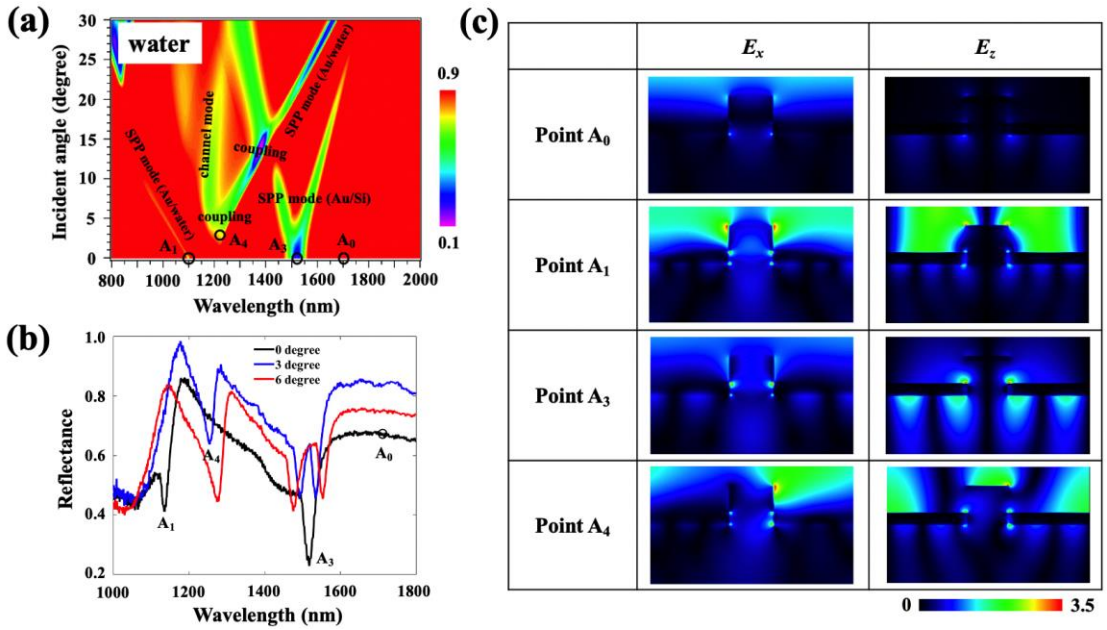

Figure 2.10 (a) The simulated reflectance variation with light wavelength and the incident angle of light for the structure immersed in DI water. (b) The measured reflectance spectra

in DI water for incident angles of 0°, 3° and 6°. (c) The electric field distributions in the *x*-(E_x) and *z*-direction (E_z) for points A_0, A_1, A_3 and A_4, as defined in (b).

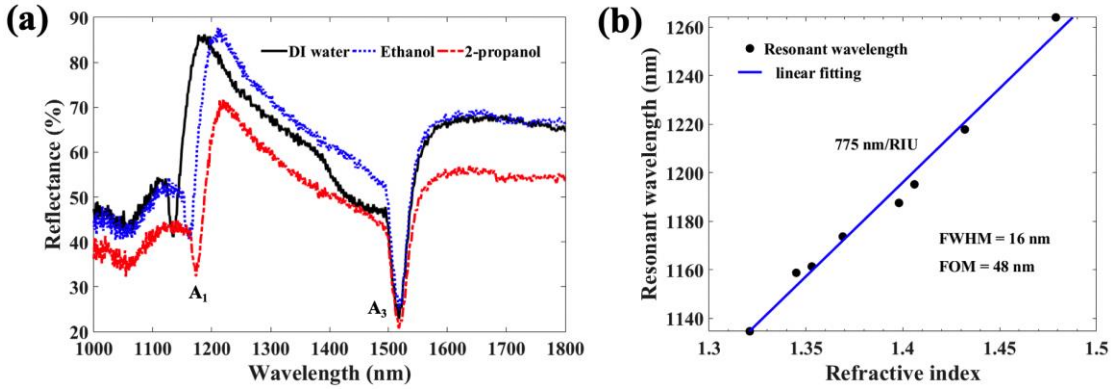

Figure 2.11 (a) The measured reflectance spectra at normal incidence of the Si channel-separated parallel grating structure immersed in the solvent of DI water, ethanol and 2-propanol. (b) Relationship between the measured resonant wavelength corresponding to dip A_1 and the refractive index of the surrounding medium.

Evaluation of the refractive index sensing ability of the Si channel-separated parallel grating structure is first investigated by changing the surrounding medium from DI water to ethanol and 2-propanol. The measured reflectance spectra in DI water, ethanol and 2-propanol are shown in figure 2.11(a). The light is normally incident (θ = 0°). It is seen that the reflectance dip A_1 exhibits a redshift gradually when the surrounding medium changes from DI water (n = 1.321) to ethanol (n = 1.353) and 2-propanol (n = 1.369), which attributes to the channel enhanced SPP mode that propagates along the Au/air interface. On the contrary, the reflectance dip A_3 shows no changes to the variation of the surrounding medium since there is no electric field enhancement at the Au/air interface corresponding to this SPP mode.

To quantificationally examine the refractive index sensing ability of the reflectance dip A_1, the sensitivity *S*, defined as $S = \triangle\lambda / \triangle n$, where λ represents resonant wavelength and *n* represents refractive index, and the figure of merit FOM, defined as FOM = *S* / FWHM, are used for the characterization of the sensing capacity. The relationship between the resonant

wavelength corresponding to reflectance dip A_1 and the refractive index of the surrounding medium is shown in figure 2.11(b). The resonant wavelength exhibits a linear relationship with the refractive index with the linear-fitting sensitivity of 775 nm/RIU and FOM of 48, demonstrating the potential for refractive index sensing application. The sensitivity and FOM values of the Si channel-separated parallel grating structure are compared with the reported RI sensors with plasmonic nanostructures, as shown in Table 1. It is seen that our proposed structure exhibits relatively high sensitivity and FOM values simultaneously, showing a competitive performance with respect to previously reported RI sensors and indicating a great potential for refractive index sensing.

Table 1. Summary of the sensitivity and FOM values of reported RI sensors with plasmonic nanostructures

Nanostructure [reference]	Resonant wavelength (nm)	FWHM (nm)	Sensitivity (nm/RIU)	FOM
Nanoparticle array [67]	700	14	365	21.5
Nanodisk clusters [68]	750	N/A	900	5.7
Split ring resonator-bar [44]	1450	121	1225	10.1
"XI" structure [45]	1305	145	685	4.7
Au nanorings [69]	980	23	380	16.5
Au mushroom arrays [47]	1250	10	1010	108.0
Cavity-coupled nanorod array [46]	1300	90	303	3.4
U-cavity [38]	845	24	807	57.0
Fabry-Pérot cavity with Au nanoparticle array [70]	920	21.2	600	28.0
Dielectric patch array backed by a metal plane [71]	1270	10	840	3.2
1D Au grating [64]	680	N/A	524	N/A
Metal-covered PMMA grating with metallic sidewalls [72]	480	150	458	N/A
Si channel-separated parallel grating structure (This work)	**1135**	**16**	**775**	**48.0**

The measured reflectance spectra of the Si channel-separated parallel grating structure immersed in the solvent of DI water, ethanol and 2-propanol at the incident angle of 3°, 6° and 9° are illustrated in figures 2.12(a)-(c), correspondingly. The reflectance dip A_4 always exhibits a redshift when the surrounding medium changes from DI water to ethanol and 2-propanol for all the incident angles of 3°, 6° and 9°. While the splitting reflectance dip A_3 shows no shifts to the change of the surrounding medium. Figure 2.12(d) gives the sensitivity and FOM variations for reflectance dip A_4 with respect to the change of incident angle of light and Si channel widths (w). Both the sensitivity and FOM values for reflectance dip A_4 fall down with the increase of incident angle, but the values increase when the Si channel width increases from 185 to 225 nm.

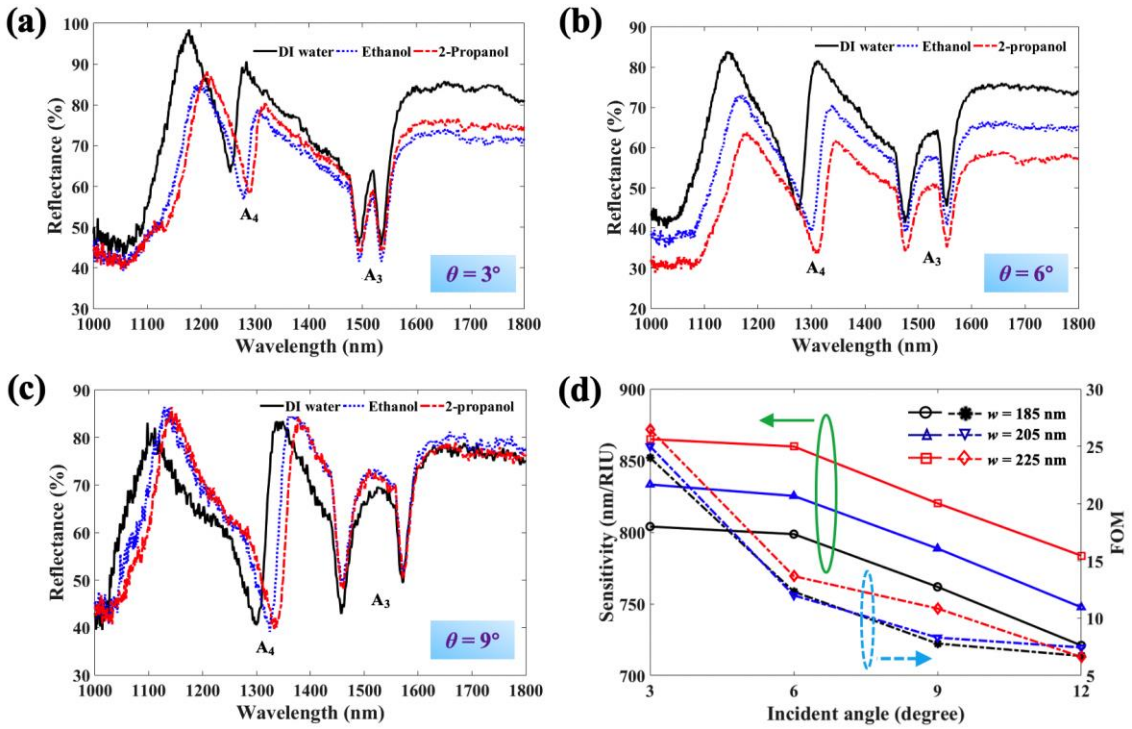

Figure 2.12 The measured reflectance spectra of the Si channel-separated parallel grating structure immersed in the solvent of DI water, ethanol and 2-propanol at the incident angle of (a) 3°, (b) 6° and (c) 9°. (d) Sensitivity and FOM variations for reflectance dip A_4 with the

incident angle of light when the surrounding medium changes from DI water to ethanol. The Si channel width (*w*) increases from 185 to 225 nm.

The measured reflectance spectra in a series of surrounding media for reflectance dip A_4 at the incident angle of 3° are given in figure 2.13(a). The reflectance dip A_4 shows a redshift with the refractive index, increasing from 1274 nm at n=1.321 to 1397 nm at n=1.479. The relationship between the resonant wavelength corresponding to reflectance dip A_4 and the refractive index of the surrounding medium is shown in figure 2.13(b). The resonant wavelength shows a linear relationship with the refractive index. The linear fitting sensitivity and FOM for reflectance dip A_4 are 753 nm/RIU and 13, respectively, which are relatively smaller compared with the reflectance dip A_1.

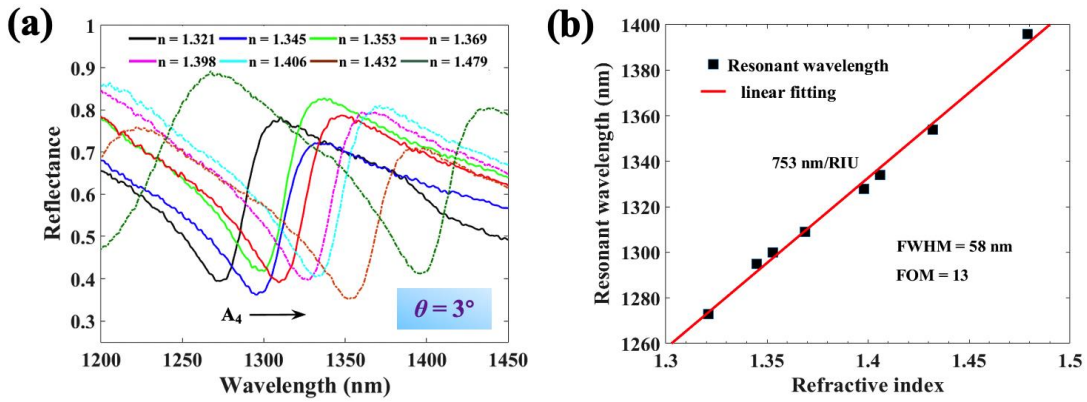

Figure 2.13 (a) The measured reflectance spectra when the structure is immersed in 8 different solvent. The incident angle of light is 3°. (b) Relationship between the measured resonant wavelength corresponding to reflectance dip A_4 and the refractive index of the surrounding medium. The incident angle of light is 3°.

2.2.3 Photocurrent response

2.2.3.1 Generation and transport of hot electrons

To obtain a better understanding of the behavior of hot electrons and the process governing the photocurrent, a band diagram illustrating the generation and transport processes of hot

electrons in one periodic unit of the Si channel-separated Au grating structure is shown in figure 2.14(a). The Fermi level of the positive Au slab is E_f and the Fermi level of the negative Au slab is $E_f + qV_a$ upon the application of a bias voltage V_a on the adjacent Au slabs. Since the photon energy ($h\nu$) within the C-band is higher than the Au/Si barrier height (φ_b = 0.75 eV) [34] and lower than the bandgap of Si (E_g = 1.12 eV), electron-hole pairs cannot be directly generated in the Si from light absorption. Therefore, only hot electrons generated in the Au slabs contribute to the photocurrent. Hot electrons with an energy exceeding the barrier height can go across the Au/Si Schottky barrier into the conduction band of the Si. As hot electrons are simultaneously generated in the negatively and positively biased Au slabs, they can generate the forward ($i_{forward}$) and backward photocurrents ($i_{backward}$) that flow in the opposite directions. These two opposite photocurrents produce a net photocurrent $i_{ph} = |i_{forward} - i_{backward}|$ that depends on the properties of the metal, the barrier height and the bias voltage [15]. In order to examine the spatial distributions of energy and generated hot electrons in the structure, the distributions of normalized absorbed power density and hot electron generation rate in one periodic unit of the structure is simulated, as shown in figure 2.14(b). The absorbed power density P_{abs} is linked to the local Ohmic loss in the metal, and hot electron generation rate G is based on one absorbed photon excites one hot electron, which is expressed as [16]

$$P_{\text{abs}} = \frac{\varepsilon_i \omega \left|\vec{E}(\vec{r},\omega)\right|^2}{2}, \tag{1}$$

$$G = \frac{P_{\text{abs}}}{\hbar\omega} = \frac{\varepsilon_i \left|\vec{E}(\vec{r},\omega)\right|^2}{2\hbar}, \tag{2}$$

where ε_i is the imaginary part of the permittivity of Au, ω is the angular frequency of incident light, $\vec{E}(\vec{r},\omega)$ is the electrical field density at the position $\vec{r}$, and $\hbar$ is the reduced Planck constant. It is seen that the Au slabs absorb almost all the power of the incident light. From the distribution of the normalized hot electron generation rate, it is found that most of hot electrons are generated in the vicinity of the Au/Si interface, which ensures the generated hot electrons have a low thermalization loss and high transport efficiency.

To further investigate the electrical properties of the structure, the electric potential distribution in the structure is simulated, as shown in figure 2.14(c). The period number is simplified to 5 and the bias voltage V_a is applied on the leftmost and rightmost Au slabs in the simulation. The electric potential in the structure drops from V_a at the positive slab (leftmost side) to 0 V at the grounded slab (rightmost side). As such, the electric field directions represented with the arrows are unified to point from the horizontal-left to the horizontal-right. The arrow indicates the direction of the electric field and the arrow length represents its intensity. The current density distribution and the current flow direction in the structure are further simulated, as shown in figure 2.14(d). The arrows indicate the direction of current flow and the arrow length represents its intensity. Seen from the simulation, the current density is concentrated in the Au slabs. Since the electric field directions are unified to point from the horizontal-left to the horizontal-right in the structure, the current formed by hot electrons transport flows horizontally in the structure.

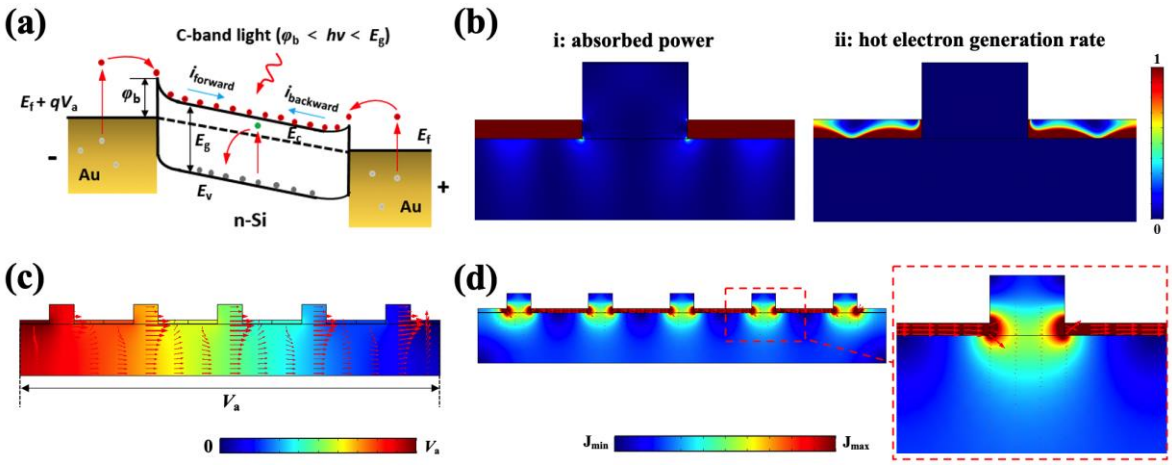

Figure 2.14 (a) The band diagram for the Si channel-separated parallel grating structure. E_v and E_c represent the valence band and conduction band energies of n-Si, respectively. E_g represents the bandgap energy of n-Si. Electron-hole pairs cannot be directly generated because the energy of the C-band light is lower than the bandgap of Si. The Fermi level of the positive Au slab is E_f and the Fermi level of the negative Au slab is $E_f + qV_a$ upon the application of a bias voltage V_a on the Au slabs. Hot electrons transporting from the negative

Au slab to the positive Au slab generate a forward current ($i_{forward}$) and the reverse transport generates a backward current ($i_{backward}$). The net photocurrent (i_{ph}) is $|i_{forward} - i_{backward}|$. (b) The distributions of (i) normalized absorbed power density and (ii) hot electron generation rate in one periodic unit of the structure. (c) The electric potential distribution in the structure at the bias voltage of V_a. The arrow indicates the direction of the electric field and the arrow length represents its intensity. (d) The simulated current density distribution in the structure and an enlarged view of one periodic unit. The arrow indicates the direction of the current flow and the arrow length represents its intensity.

2.2.3.2 Spectrally selective photodetection in the near infrared

To evaluate the photocurrent response of the structure under illumination, the responsivity (R) is calculated by $R = (i_{ph} - i_d) / P_{in}$, where i_{ph} represents the photocurrent, i_d represents the dark current and P_{in} represents the effective power of light illuminated on the structure. In our experiment, the center of the structure was illuminated at normal incidence by a C-band wavelength tunable laser source (TLG-210, Alnair Labs Corporation, Tokyo, Japan). The effective area of the structure under illumination was 0.785 mm^2. A photodiode amplifier (PDA200C, Thorlabs, New Jersey, US) was used to supply a bias voltage (1 V) on the structure. It is noted that since the structure is highly symmetrical, hot electrons transports generate an equal forward and backward photocurrent at the bias voltage of 0 V and this leads the corresponding photocurrent to be 0 A. Therefore, the proposed structure can only work under the bias condition. When the bias voltage V satisfies the requirement $eV > h\nu$, the backward current ($i_{backward}$) is zero and hence the photocurrent ($i_{forward} - i_{backward}$) is maximal. In this chapter, we mainly explore the photocurrent response of the proposed structure in the telecommunication C-band (1530-1565 nm) so that the photon energy $h\nu$ is in the range of 0.793~0.811 eV. To satisfy $eV > h\nu$, the applied bias voltage to the structure is 1 V in the experiment.

The experiment setup for measuring the photocurrent under irradiation is shown in figure 2.15, which includes a bias module (power supply, model PDA200C, Thorlabs, New

Jersey, US), a lock-in amplifier (model LI5640Y, NF Corporation, Yokohama, Japan), a optical chopper (model MC1F10, Thorlabs, New Jersey, US) and a C-band wavelength tunable laser source (model TLG-210, Alnair Labs Corporation, Tokyo, Japan). Unless otherwise noted, the light is normally incident and TM-polarized with a light intensity of 10 mW, and the effective area of the structure under illumination is about 0.785 mm^2.

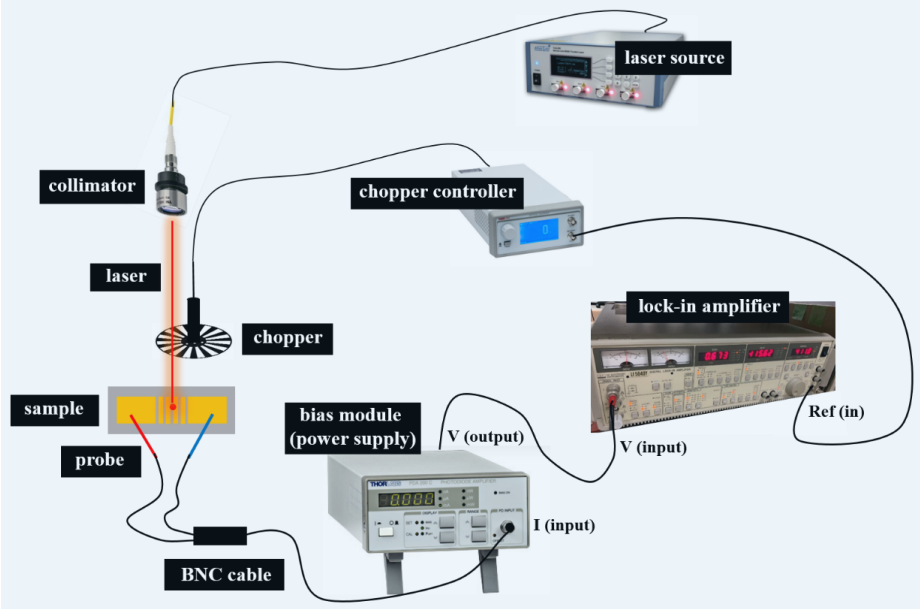

Figure 2.15 The experiment setup for measuring the photocurrent under light irradiation.

The measured responsivity for the structure with a period of 850 nm and the corresponding reflectance spectrum are given in figure 2.16(a). The responsivity exhibits spectral selectivity in the C-band with a peak value reaching 72.5 nA/mW at the resonant wavelength of 1538 nm. The responsivity variation is opposite to the variation of the reflectance over the C-band, suggesting the photocurrent is directly proportional to the absorptance of the structure. It is noted that the absorptance and reflectance of the structure have opposite behaviors in the C-band, as indicated in figure 2.6(a). The measured responsivity for the structure with a period of 840 nm and the corresponding reflectance spectrum are shown in figure 2.16(b). Through decreasing the period of the structure, the resonant wavelength is blue-shifted to 1520 nm. The responsivity steadily decreases across

the C-band as the wavelength increases, dropping from 64.5 nA/mW (R_1) at 1530 nm to 19.0 nA/mW (R_2) at 1565 nm. The responsivity variation within the C-band $(R_1\text{-}R_2)/R_1 \cdot 100\%$ reaches as high as 70.5%, demonstrating the excellent spectral selectivity in the C-band.

The reasons why the responsivity is measured only for the period of 840 nm and 850 nm are twofold: (1) The responsivity variation for the period of 850 nm spans the complete reflectance dip over the C band and therefore both an increase and a decrease in the responsivity can be observed (figure 2.16(a)). This peak in responsivity demonstrates that the observed response is due to hot electrons and not to a drift in the system such as the thermal effect, which should produce a slow and steady variation due to the increase of the sample temperature. The thermal effect is also discussed in the end of this chapter. (2) To increase the spectral selectivity of the structure in the C-band (1530 nm to 1565 nm), the responsivity should exhibit a large steady variation over the complete range of wavelengths in the C band. In other words, the reflectance variation in the C-band should be steady (monotonic function) and so we selected the sample with the reflectance dip corresponding to the lower bound (1530 nm) of the C band. For the sample with a period of 840 nm, the dip of the reflectance spectrum is at 1520 nm and the reflectance is steadily decreasing across the C-band, so that the responsivity variation exhibits an excellent spectral selectivity behavior (figure 2.14(b)).

In order to investigate the polarization dependence of photocurrent of the structure, the photocurrents under different polarization angles are measured, as shown in figure 2.16(c). The period of the structure is 850 nm, and the light wavelength is 1538 nm. 0° is defined as the electric field direction pointing along the Si channels. The measurement results show that the Si channel-separated Au grating structure is strongly polarization-dependent. The generation of hot electrons is strongly enhanced at TM polarization (90°, 270°) and a large photocurrent is produced, whereas fewer hot electrons are generated at TE polarization (0°, 180º, 360°) and therefore it produces a small photocurrent. The ratio of photocurrent at TM polarization to that at TE polarization reaches as high as 26:1. The insets show the normalized electric field distributions in one periodic unit of the structure at TE and TM polarizations. For TE polarization, the electric field is quite weak and there is only minimal enhancement

of the electric field at the bottom of Si channels. On the contrary, for TM polarization, the electric field is strongly enhanced at the corners of the Au slabs and the bottom Au/Si interface, indicating the presence of SPP. Figure 2.16(d) shows the photocurrent variation with the light intensity at the wavelengths of 1530, 1538 and 1546 nm. The period of the structure is 850 nm. The photocurrent shows a linear dependence on the light intensity, confirming the generation of hot electrons mainly results from the single photon-hot electron interaction [11]. Since the resonant wavelength is 1538 nm, the measured photocurrent at this wavelength is much larger than any other wavelength.

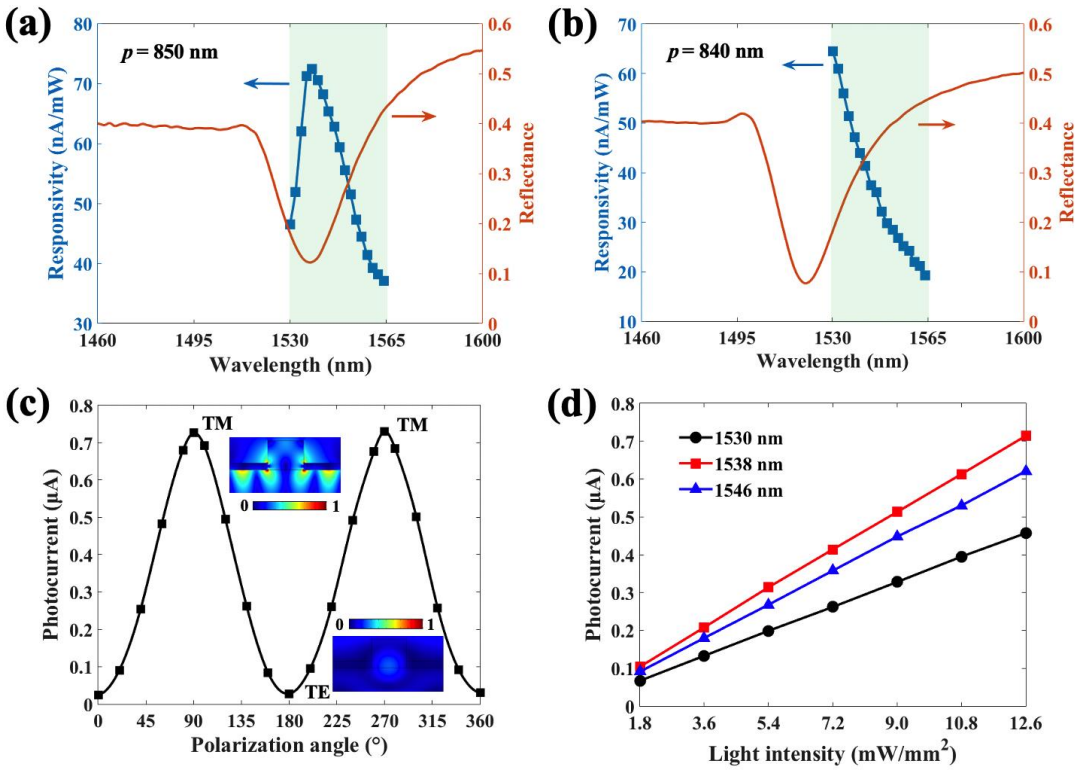

Figure 2.16 The electrical properties of the Si channel-separated parallel grating structure under illumination. The light is normally incident, and the applied bias voltage on the structure is kept at 1.0 V. The measured responsivities and the reflectance spectra for the structure period of (a) 850 nm and (b) 840 nm. The light is TM polarized with an intensity of 12.7 mW/mm^2. (c) The dependence of the measured photocurrent on the polarization angle of light. The period of the structure is 850 nm, and the light wavelength is 1538 nm with an

intensity of 12.7 mW/mm^2. The polarization angle of 0º is defined as the electric field direction pointing along the Si channels. The two insets show the electric field distributions at TE and TM polarization. (d) The measured photocurrent variation with the light intensity at the wavelengths of 1530, 1538 and 1546 nm. The period of the structure is 850 nm, and the light is TM-polarized.

The temporal photoresponse of the structure upon periodic illumination was recorded with an oscilloscope and a mechanical shutter. The measured temporal photoresponse of the structure upon the periodic illumination is shown in figure 2.17(a). The period of the structure is 850 nm, and the light is TM polarized with an intensity of 12.7 mW/mm^2. To evaluate the photoresponse speed, the rise time (t_r) is defined as the time required for photocurrent to increase from 10% to 90% of the saturation value, and the fall time (t_f) is the time required for photocurrent to decrease from 90% to 10% of the saturation value. According to the definition, the calculated t_r and t_f upon the periodic illumination of the structure are 150 and 166 ms, respectively, as shown in figures 2.17(b) and (c).

The photoresponse speed of MSM photodetectors with interdigitated electrodes are primary limited by the transit time (t_{tr}) of photocarriers travelling across the active region and the resistance-capacitance (RC) time constant (t_{RC}).[73-77] A simplified approximation to the overall response time (t) of the photodetector can be calculated by $t = \sqrt{t_{tr}^2 + t_{RC}^2}$.[73, 75, 76] The transit time t_{tr} of photocarriers in our structure can be neglected since the Si channel is only 270 nm and the mean drift velocity for photocarrier in silicon under the high electric field gets close to 10^7 cm/s, leading to the t_{tr} as small as 2.7 ps. The RC time constant t_{RC} is much larger than t_{tr} because of the formation of large internal capacitance at the metal/semiconductor interface. Therefore, the relatively slow photoresponse of our structure is due to the presence of large internal capacitance formed at the M/S interface, which leads to a large resistance-capacitance (RC) time constant. The small difference between the measured t_r and t_f of our structure may be explained by the recombination effects and the presence of defect state in the structure.

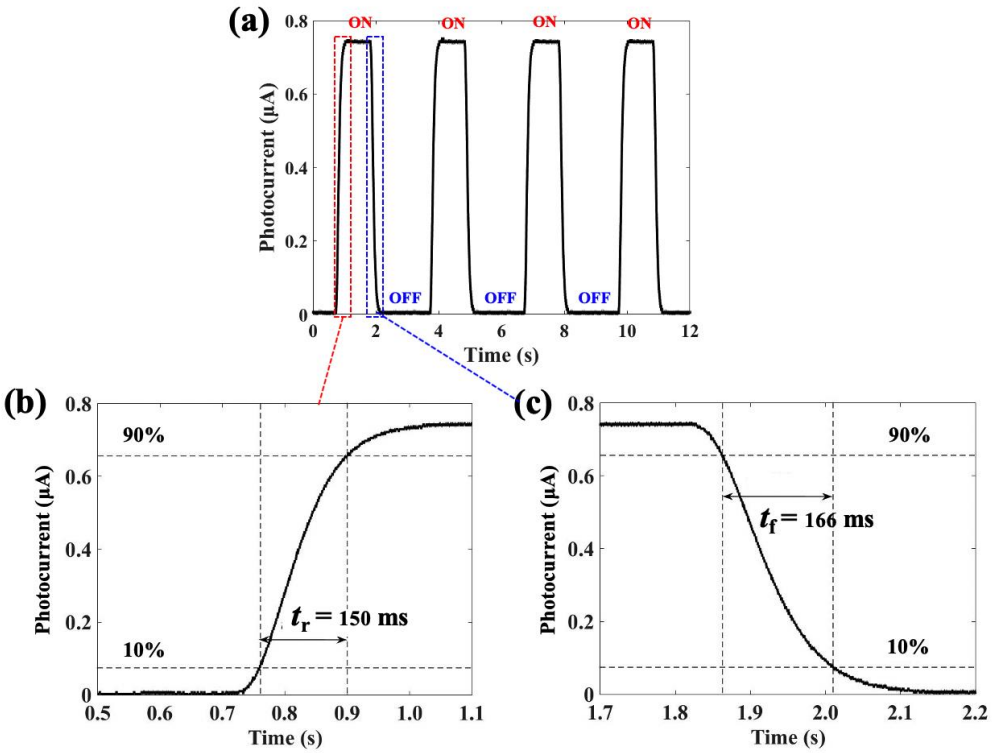

Figure 2.17 (a) The temporal photoresponse of the structure upon the periodic illumination. The period of the structure is 850 nm, and the light is TM polarized with an intensity of 12.7 mW/mm^2. The rise time (t_r) and fall time (t_r) upon the periodic illumination is shown in (b) and (c), respectively.

2.3 Discussion

In summary, we proposed a Si channel-separated parallel grating structure for refractive index sensing and spectrally selective photodetection in the C-band in this chapter. The structure owns a strong capacity to trap and focus the incident light by different plasmon resonance modes. The channel enhanced SPP mode can enhance the electric field at the Au/air interface at normal incidence, which makes the reflectance dip highly sensitive to the change of the refractive index of the surrounding medium. The linear fitting sensitivity reaches as high as 775 nm/RIU with the FOM value approaching 48, which is competitive with previously reported RI sensors with plasmonic nanostructures. The electric field at the

Au/air interface and the top-surface of Si channels are also strongly enhanced attributing to the coupling of SPP mode and channel mode when the incident light is tilted, exhibiting a high sensitivity to the variation of refractive index of the surrounding medium. The linear fitting sensitivity at the incident angle of 3° reaches 753 nm/RIU with a FOM of 13. The SPP mode that propagates along the Au/Si interface confines light at the corners of the Au nanoslab and the Au/Si interface. But the reflectance dip shows no shift to the change of the surrounding medium due to the weak enhancement at the Au/air interface. However, by taking advantages of the SPP-induced hot electrons, the structure overcomes the native limitations from the bandgap of semiconductors and achieves sub-bandgap photodetection with relative high responsivity. The measured responsivity for the structure with a period of 850 nm shows the spectral selectivity in the C-band. The peak responsivity reaches 72.5 nA/mW at the resonant wavelength of 1538 nm, suggesting that the responsivity variation in the C-band is a result of hot electrons that are excited by SPPs coupled at the resonant wavelength. The measured responsivity for the structure with a period of 840 nm steadily decreases across the C-band as the wavelength increases. The responsivity variation within the C-band reaches as high as 70.5%, demonstrating the excellent spectral selectivity in the C-band. With these outstanding properties, the proposed structure is promising for numerous applications that require narrowband and spectrally selective detection.

References

[1] C. Clavero, "Plasmon-induced hot-electron generation at nanoparticle/metal-oxide interfaces for photovoltaic and photocatalytic devices," *Nat. Photonics* **8**, 95 (2014)

[2] X. Zhang, Y. L. Chen, R. S. Liu and D. P. Tsai, "Plasmonic photocatalysis," *Rep. Prog. Phys.* **76,** 046401 (2013)

[3] P. Narang, R. Sundararaman and H. A. Atwater, "Plasmonic hot carrier dynamics in solid-state and chemical systems for energy conversion," *Nanophotonics* **5**, 96-111 (2016)

[4] S. Foroutan and H. Baghban, "Theory of plasmonic quantum-dot-based intermediate band solar cells," *Appl. Opt.* **55** 3405-3412 (2016)

[5] Y. H. Chou, Y. M. Wu, K. B. Hong, B. T. Chou, J. H. Shih, Y. C. Chung and T. C. Lu, "High-operation-temperature plasmonic nanolasers on single-crystalline aluminum," *Nano Lett.* **16**, 3179-3186 (2016)

[6] Y. J. Lu, J. Kim, H. Y. Chen, C. Wu, N. Dabidian, C. E. Sanders and W. H. Chang, "Plasmonic nanolaser using epitaxially grown silver film," *Science* **337**, 450-453 (2012)

[7] Y. L. Ho, L. C. Huang and J. J. Delaunay, "Spectrally selective photocapacitance modulation in plasmonic nanochannels for infrared imaging," *Nano Lett.* **16**, 3094-3100 (2016)

[8] Y. L. Ho, Y. H. Tai, J. K. Clark, Z. Wang, P. K. Wei and J. J. Delaunay, "Plasmonic Hot-Carriers in Channel-Coupled Nanogap Structure for Metal–Semiconductor Barrier Modulation and Spectral-Selective Plasmonic Monitoring," *ACS Photonics* **5** 2617-2623 (2018)

[9] J. Wang, M. S. Gudiksen, X. Duan, Y. Cui and C. M. Lieber, "Highly polarized photoluminescence and photodetection from single indium phosphide nanowires," *Science* **293**, 1455-7 (2001)

[10] Y. Zhai, G. Chen, J. Ji, X. Ma, Z. Wu, Y. Li and Q. Wang, "Large-scale, broadband absorber based on three-dimensional aluminum nanospike arrays substrate for surface plasmon induced hot electrons photodetection," *Nanotechnology* **30**, 37 (2019)

[11] T. Gong and J. N. Munday, "Angle-independent hot carrier generation and collection using transparent conducting oxides," *Nano Lett.* **15**, 147-152 (2014)

[12] B. Feng, J. Zhu, B. Lu, F. Liu, L. Zhou and Y. Chen, "Achieving Infrared Detection by All-Si Plasmonic Hot-Electron Detectors with High Detectivity," *ACS Nano* **13**, 8433-8441 (2019)

[13] I. Goykhman, B. Desiatov, J. Khurgin, J. Shappir and U. Levy, "Locally oxidized silicon surface-plasmon Schottky detector for telecom regime," *Nano Lett.* **11**, 2219-2224 (2011)

[14] Y. Xie, L. Wei, G. Wei, Q. Li, D. Wang, Y. Chen and J. Jiao, "A self-powered UV photodetector based on TiO_2 nanorod arrays," *Nanoscale. Res. Lett.* **8**, 188 (2013)

[15] S. Mubeen, G. Hernandez-Sosa, D. Moses, J. Lee and M. Moskovits, "Plasmonic photosensitization of a wide band gap semiconductor: converting plasmons to charge carriers," *Nano Lett.* **11**, 5548-5552 (2011)

[16] H. Chalabi, D. Schoen and M. L. Brongersma, "Hot-electron photodetection with a plasmonic nanostripe antenna," *Nano Lett.* **14**, 1374-1380 (2014)

[17] Z. Burshtein and J. Levinson, "Photo-induced tunnel currents in Al-Al_2O_3-Au structures," *Phys. Rev. B* **12**, 3453 (1975)

[18] F. Wang and N. A. Melosh, "Plasmonic energy collection through hot carrier extraction," *Nano Lett.* **11**, 5426-5430 (2011)

[19] S. Grover and G. Moddel, "Applicability of metal/insulator/metal (MIM) diodes to solar rectennas," *IEEE J. Photovolt.* **1**, 78-83 (2011)

[20] B. Zhu, M. Chen, Q. Zhu, G. Zhou, N. M. Abdelazim, W. Zhou and H. K. Tsang, "Integrated Plasmonic Infrared Photodetector Based on Colloidal HgTe Quantum Dots," *Adv. Mater. Technol.* **4**, 1900354 (2019)

[21] M. W. Knight, H. Sobhani, P. Nordlander and N. J. Halas, "Photodetection with active optical antennas," *Science* **332**, 702-704 (2011)

[22] K. T. Lin, H. L. Chen, Y. S. Lai and C. C. Yu, "Silicon-based broadband antenna for high responsivity and polarization-insensitive photodetection at telecommunication wavelengths," *Nat. Commun.* **5**, 3288 (2014)

[23] W. Li and J. Valentine, “Metamaterial perfect absorber based hot electron photodetection,” *Nano Lett.* **14**, 3510-3514 (2014)

[24] A. Sobhani, M. W. Knight, Y. Wang, B. Zheng, N. S. King, L. V. Brown and N. J. Halas, “Narrowband photodetection in the near-infrared with a plasmon-induced hot electron device,” *Nat. Commun.* **4**, 1643 (2013)

[25] B. Y. Zheng, H. Zhao, A. Manjavacas, M. McClain, P. Nordlander and N. J. Halas, “Distinguishing between plasmon-induced and photoexcited carriers in a device geometry,” *Nat. Commun.* **6**, 7797 (2015)

[26] M. W. Knight, Y. Wang, A. S. Urban, A. Sobhani, B. Y. Zheng, P. Nordlander and N. J. Halas, “Embedding plasmonic nanostructure diodes enhances hot electron emission,” *Nano Lett.* **13**, 1687-1692 (2013)

[27] H. Kind, H. Yan, B. Messer, M. Law and P. Yang, “Nanowire ultraviolet photodetectors and optical switches,” *Adv. Mater.* **14**, 158-160 (2002)

[28] B. Feng, J. Zhu, C. Xu, J. Wan, Z. Gan, B. Lu, and Y. Chen, “All-Si Photodetectors with a Resonant Cavity for Near-Infrared Polarimetric Detection,” *Nanoscale Res. Lett.* **14**, 39 (2019)

[29] H. Kwon, J. B. You, Y. Jin, and K. Yu, “Ultra-compact silicon waveguide-integrated Schottky photodetectors using perfect absorption from tapered metal nanobrick arrays,” *Opt. Express* **27**, 16413-16424 (2019)

[30] I. Goykhman, B. Desiatov, J. Khurgin, J. Shappir and U. Levy, “Waveguide based compact silicon Schottky photodetector with enhanced responsivity in the telecom spectral band,” *Opt. Express* **20**, 28594-28602 (2012)

[31] T. Y. Lin, K. T. Lin, C. C. Lin, Y. W. Lee, L. T. Shiu, W. Y. Chen, and H. L. Chen, “Magnetic fields affect hot electrons in silicon-based photodetectors at telecommunication wavelengths,” *Mater. Horiz.* **6**, 1156 (2019)

[32] S. S. Mousavi, A. Stöhr, and P. Berini, “Plasmonic photodetector with terahertz electrical bandwidth,” *Appl. Phys. Lett.* **104**, 143112 (2014)

[33] M. Casalino, M. Iodice, L. Sirleto, I. Rendina, and G. Coppola, "Asymmetric MSM sub-bandgap all-silicon photodetector with low dark current," *Opt. Express* **21**, 28072-28082 (2013)

[34] K. Wu, Y. Zhan, C. Zhang, S. Wu and X. Li, "Strong and highly asymmetrical optical absorption in conformal metal-semiconductor-metal grating system for plasmonic hot-electron photodetection application," *Sci. Rep.* **5**, 14304 (2015)

[35] W. D. Wilson, "Analyzing biomolecular interactions," *Science* **295**, 2103-2105 (2002)

[36] A. G. Brolo, "Plasmonics for future biosensors," *Nat. Photonics* **6**, 709 (2012)

[37] Y. Shen, J. Zhou, T. Liu, Y. Tao, R. Jiang, M. Liu and C. Jin, "Plasmonic gold mushroom arrays with refractive index sensing figures of merit approaching the theoretical limit," *Nat. Commun.* **4**, 2381 (2013)

[38] Y. L. Ho, A. Portela, Y. Lee, E. Maeda, H. Tabata and J. J. Delaunay, "Hollow Plasmonic U−Cavities with High−Aspect−Ratio Nanofins Sustaining Strong Optical Vortices for Light Trapping and Sensing," *Adv. Opt. Mater* **2**, 522-528 (2014)

[39] E. Maeda, Y. Lee, Y. Kobayashi, A. Taino, M. Koizumi, S. Fujikawa and J. J. Delaunay, "Sensitivity to refractive index of high-aspect-ratio nanofins with optical vortex," *Nanotechnology* **23**, 505502 (2012)

[40] K. Lodewijks, R. W. Van, G. Borghs, L. Lagae and D. P. Van, "Boosting the figure-of-merit of LSPR-based refractive index sensing by phase-sensitive measurements," *Nano Lett* **12**, 1655–1659 (2012)

[41] M. A. Schmidt, D. Y. Lei, L. Wondraczek, V. Nazabal, and S. A. Maier, "Hybrid nanoparticle–microcavity-based plasmonic nanosensors with improved detection resolution and extended remote-sensing ability," *Nat. Commun.* **3**, 1108 (2012)

[42] S. P. Zhang, K. Bao, N. J. Halas, H. X. Xu, and P. Nordlander, "Substrate-induced Fano resonances of a plasmonic nanocube: a route to increased-sensitivity localized surface plasmon resonance sensors revealed," *Nano Lett.* **11**, 1657–1663 (2011)

[43] R. Ameling, L. Langguth, M. Hentschel, M. Mesch, P. V. Braun, and H. Giessen, "Cavity-enhanced localized plasmon resonance sensing," *Appl. Phys. Lett.* **97**, 253116 (2010)

[44] I. M. Pryce, Y. A. Kelaita, K. Aydin and H. A. Atwater, "Compliant metamaterials for resonantly enhanced infrared absorption spectroscopy and refractive index sensing," *ACS Nano* **5**, 8167–8174 (2011)

[45] N. Verellen, D. P. Van, C. Huang, K. Lodewijks, G. A. Vandenbosch, L. Lagae, and V. V. Moshchalkov, Plasmon line shaping using nanocrosses for high sensitivity localized surface plasmon resonance sensing. *Nano Lett.* **11**, 391–397 (2011)

[46] R. Ameling, L. Langguth, M. Hentschel, M. Mesch, P. V. Braun, and H. Giessen, "Cavity-enhanced localized plasmon resonance sensing," *Appl. Phys. Lett.* **97**, 253116 (2010)

[47] Y. Shen, J. Zhou, T. Liu, Y. Tao, R. Jiang, M. Liu and C. Jin, "Plasmonic gold mushroom arrays with refractive index sensing figures of merit approaching the theoretical limit," *Nat. Commun.* **4**, 2381 (2013)

[48] G. Vecchi, V. Giannini and R. J. Gomez, "Surface modes in plasmonic crystals induced by diffractive coupling of nanoantennas," *Phys. Rev. B* **80**, 201401(R) (2009)

[49] V. G. Kravets, F. Schedin, and A. N. Grigorenko, "Extremely narrow plasmon resonances based on diffraction coupling of localized plasmons in arrays of metallic nanoparticles," *Phys. Rev. Lett.* **101**, 087403 (2008)

[50] W. Zhou, and T. W. Odom, "Tunable subradiant lattice plasmons by out-of-plane dipolar interactions," *Nat. Nanotech.* **6**, 423–427 (2011)

[51] A. Dmitriev, C. Hagglund, S. Chen, H. Fredriksson, T. Pakizeh, M. Kall and D. S. Sutherland, "Enhanced Nanoplasmonic Optical¨Sensors with Reduced Substrate Effect," *Nano Lett.* **8**, 3893−3898 (2008)

[52] M. Svedendahl, S. Chen, A. Dmitriev and M. Kall, "Refractometric sensing using propagating versus localized surface plasmons: a direct comparison," *Nano Lett.* **9**, 4428-4433 (2009)

[53] S. J. Zalyubovskiy, M. Bogdanova, A. Deinega, Y. Lozovik, A. D. Pris, K. H. An, and R. A. Potyrailo, "Theoretical limit of localized surface plasmon resonance sensitivity to local refractive index change and its comparison to conventional surface plasmon resonance sensor," *JOSA A* **29**, 994-1002 (2012)

[54] K. Tiwari and C. S. Suresh, “Surface plasmon based sensor with order-of-magnitude higher sensitivity to electric field induced changes in dielectric environment at metal/nematic liquid-crystal interface,” *Sensors and Actuators A: Physical* **216**, 128-135 (2014)

[55] A. Paliwal, T. Monika and G. Vinay, “Refractive index sensor using long-range surface plasmon resonance with prism coupler,” *Plasmonics* **14**, 375-381. (2019)

[56] A. K. Mishra, K. M. Satyendra, and K. V. Rajneesh, “An SPR-based sensor with an extremely large dynamic range of refractive index measurements in the visible region,” *Journal of Physics D: Applied Physics* **48**, 435502 (2015)

[57] C. Liao, K. Yang, J. Wang, Z. Bai, Z. Gan, and Y. Wang, “Helical Microfiber Bragg Grating Printed by Femtosecond Laser for Refractive Index Sensing,” *IEEE Photonics Technology Letters* **31**, 971-974 (2019)

[58] F. Shen, C. Wang, Z. Sun, K. Zhou, L. Zhang and X. Shu, “Small-period long-period fiber grating with improved refractive index sensitivity and dual-parameter sensing ability,” *Opt. Lett.* **42**, 199-202 (2017)

[59] X. Chen, J. Xu, X. Zhang, T. Guo and B. O. Guan, “Wide range refractive index measurement using a multi-angle tilted fiber Bragg grating,” *IEEE. Photonic. Tech. L.* **29**, 719-722 (2017)

[60] Y. Dai, H. Xu, H. Wang, Y. Lu, and P. Wang, “Experimental demonstration of high sensitivity for silver rectangular grating-coupled surface plasmon resonance (SPR) sensing,” *Opt. Commun.* **416**, 66-70 (2018)

[61] L. Li, Y. Liang, M. Lu and W. Peng, “Fano resonances in thin metallic grating for refractive index sensing with high figure of merit,” *Plasmonics* **11**, 139-49 (2016)

[62] D. Cai, Y. Lu, K. Lin, P. Wang and H. Ming, “Improving the sensitivity of SPR sensors based on gratings by double-dips method (DDM),” *Opt. Express* **16**, 14597-602 (2008)

[63] W. Su, G. Zheng, and X. Li, “Design of a highly sensitive surface plasmon resonance sensor using aluminum-based diffraction grating,” *Opt. Commun.* **285**, 4603-4607 (2012)

[64] T. Iqbal, and S. Afsheen, "One dimensional plasmonic grating: high sensitive biosensor," *Plasmonics* **12**, 19-25 (2017)

[65] J. Homola, I. Koudela and S. S. Yee, "Surface plasmon resonance sensors based on diffraction gratings and prism couplers: sensitivity comparison," *Sensors Actuat. B-Chem.* **54**, 16-24 (1999)

[66] J. Homola, S. Y. Sinclair, and G. Günter, "Surface plasmon resonance sensors: review," *Sensors and Actuators B: Chemical* **54**, 3-15 (1999)

[67] A. I. Kuznetsov, A. B. Evlyukhin, M. R. Gonçalves, C. Reinhardt, A. Koroleva, M. L. Arnedillo and B. N. Chichkov, "Laser fabrication of large-scale nanoparticle arrays for sensing applications," *ACS Nano* **5**, 4843-4849 (2011)

[68] J. B. Lassiter, H. Sobhani, J. A. Fan, J. Kundu, F. Capasso, P. Nordlander, and N. J. Halas, "Fano resonances in plasmonic nanoclusters: geometrical and chemical tunability," *Nano Lett.* **10**, 3184-3189 (2010)

[69] K. Lodewijks, R. W. Van, G. Borghs, L. Lagae and D. P. Van, "Boosting the figure-of-merit of LSPR-based refractive index sensing by phase-sensitive measurements," *Nano Lett.* **12**, 1655-1659 (2012)

[70] J. Chen, Q. Zhang, C. Peng, C. Tang, X. Shen, L. Deng and G. S. Park, "Optical cavity-enhanced localized surface plasmon resonance for high-quality sensing," *IEEE. Photonic. Tech. L.* **30**, 728-731 (2018)

[71] X. Lu, T. Zhang, R. Wan, Y. Xu, C. Zhao, and S. Guo, "Numerical investigation of narrowband infrared absorber and sensor based on dielectric-metal metasurface," *Opt. Express* **26**, 10179-10187 (2018)

[72] W. H. Yang, C. Zhang, S. Sun, J. Jing, Q. Song, and S. Xiao, "Dark plasmonic mode based perfect absorption and refractive index sensing," *Nanoscale* **9**, 8907-8912 (2017)

[73] K. L. Hsiung, "A Note on Response Time Minimization for Planar MSM Photodetectors," *Thirty-Ninth Southeastern Symposium on System Theory IEEE*. 236-237 (2007)

[74] L. K. Wang, Z. G. Ju, C. X. Shan, J. Zheng, D. Z. Shen, B. Yao, and J. Y. Zhang, "MgZnO metal–semiconductor–metal structured solar-blind photodetector with fast response," Solid State Commun. **149**, 2021 (2009)

[75] S. V. Averine, Y. C. Chan, and Y. L. Lam, "Optimization of high-speed MSM-photodiode structures," *Proceedings. Conference on Optoelectronic and Microelectronic Materials and Devices. IEEE.* 515-518 (2000)

[76] Z. Shi, H. Ding, H. Hong, D. Cheng, K. Rajabi, J. Yang, and X. Sheng, "Ultrafast and l ow-power optoelectronic infrared-to-visible upconversion devices," *Photonics Res.* **7**, 1161 (2019)

[77] J. Lu, R. Surridge, G. Pakulski, K. van Driel, and J. M. Xu, "Studies of high-speed metal-semiconductor-metal photodetector with a GaAs/AlGaAs/GaAs heterostructure," *IEEE T. Electron. Dev.* **40**, 1087 (1993)

Chapter 3 : Spectrally selective and high responsivity photodetection in the near infrared using a Si channel-separated interdigitated grating structure

3.1 Introduction

Surface plasmons (SPs), the coherent oscillations of free electrons in metals that can be excited with electromagnetic waves, play a key role in routing and manipulating light at nanoscale volumes [1-3]. Relying on the properties of high-field concentrations and resonant scattering, SPs have been widely used in a variety of applications, such as surface-enhanced spectroscopy and sensing devices [4,5], solar energy harvesting devices [6,7], medical devices [8,9], imaging devices [10], monitoring devices [11] and photodetectors [12-17]. The main advantage of SPs-based photodetectors over conventional photodetectors is their ability to facilitate the generation of photoexcited hot electrons or generate plasmon-induced hot electrons at high efficiencies [14,16], which leads them also being referred to as hot electron photodetectors. In hot electron photodetectors, a metallic nanostructure is commonly located at the active region to effectively collect light and enhance the electromagnetic field intensity. The electromagnetic energy can then be transferred to the hot electrons and ensure them to possess enough momentum to cross the M/S barrier before thermalization. After that, the hot electrons will be injected into the conduction band of the semiconductor, resulting in a photocurrent that can be detected with an external circuit. This enables the selective detection of photons whose energies ($h\nu$) are higher than the barrier height (φ_b) but lower than the bandgap (E_g) of a semiconductor (i.e., $\varphi_b < h\nu < E_g$).

Hot electron photodetectors have been investigated in a variety of architectures, including antennas [18-21], nanorods [22,23], nanowires [24-26], waveguides [27-29], metal gratings [30-32], and gratings with deep trench cavities [33]. Among them, grating based

structures exploit an efficient approach for strong light confinements through exciting surface plasmon polaritons (SPPs), leading to a resonant and narrowband photocurrent response. In this chapter, we propose a Si channel-separated interdigitated grating structure, reshaping the Au grating from a traditionally parallel structure to an interdigitated structure and separating the Au grating with U-shaped Si channels. The structure takes advantage of strongly resonant and narrowband optical response and the generation of hot electrons, realizing the spectrally selective photodetection in the C-band.

3.2 Experiment and simulation results

3.2.1 Structure diagram and fabrication process

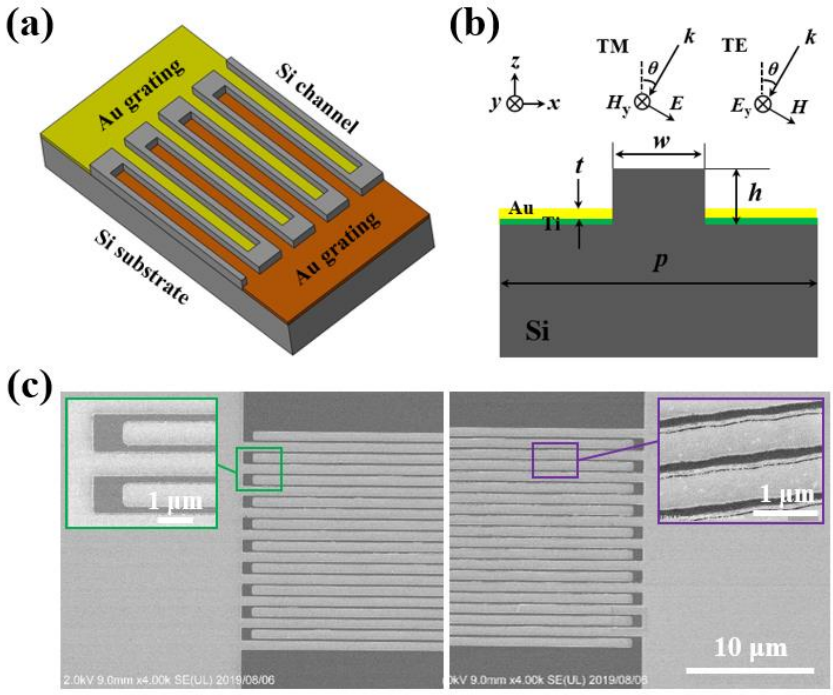

Figure 3.1 (a) The schematic diagram of the Si channel-separated interdigitated grating structure. (b) The cross section of one periodic unit of the structure. TM and TE represent the polarizations of light. *k* represents the Poynting vector of incident light, *E* represents electric field and *H* represents magnetic field. (c) The SEM image of the fabricated sample which

clips the middle part and shows the left and right sides of the structure. The insets show the magnified views of the structure.

The schematic diagram of the Si channel-separated interdigitated grating structure is illustrated in figure 3.1(a). The structure is made up of two interdigitated Au gratings separated by U-shaped Si channels. The cross section of one periodic unit of the structure is shown in figure 3.1(b). The width (w) and height (h) of the Si channel, the thickness (t) of the Au slab, the period (p) of the structure and the incident angle (θ) of light are all defined in the figure. The illustrations for TM- (transverse magnetic) and TE-polarized (transverse electric) light are also displayed in the figure. Unless otherwise noted, the light is TM-polarized and normally incident in this chapter. The dimensions of the structure are w = 280 nm, h = 200 nm, t = 40 nm. p ranges from 820 to 890 nm, and the thickness of Ti layer is 2 nm. Figure 3.1(c) displays the scanning electron microscope (SEM) image of the fabricated sample with the center of the structure cropped out. The insets display the magnified views of the structure.

The fabrication process for the Si channel-separated interdigitated grating structure is the same with the Si channel-separated grating structure, as illustrated in figure 3.2. The fabrication process includes the electron-beam (EB) resist coating, EB lithography, reactive ion etching (RIE) of Si, EB evaporation of Ti and Au, and lift-off.

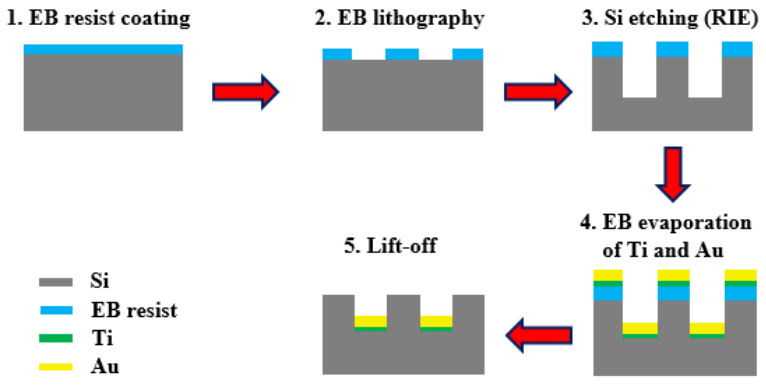

Figure 3.2 The fabrication process for the Si channel-separated interdigitated grating structure.

Due to the complicated nanofabrication techniques, some samples with different imperfections are also fabricated. The two main issues come from the non-uniform deposition of Au layers (this issue has been clearly clarified in chapter 2), and the unsuccessful lift-off. As shown in figures 3.3(a)-(b), some Au layers are not deposited or uniformly deposited between Si channels. Since the bias voltage is applied to the adjacent Au layers when measuring the photocurrent under light illumination, this non-uniform deposition of Au layer leads to no electrical connection problem. The unsuccessful lift-off also brings in big imperfections to the sample, such as the Au cladding on Si channels as shown in figure 3.3(c) and the Au layers are residual on the sample after lift-off as shown in figure 3.3(d). The Au cladding and residual Au layers on Si channels lead to short circuit during the photocurrent measurements as the bias voltage is applied to the adjacent Au layers.

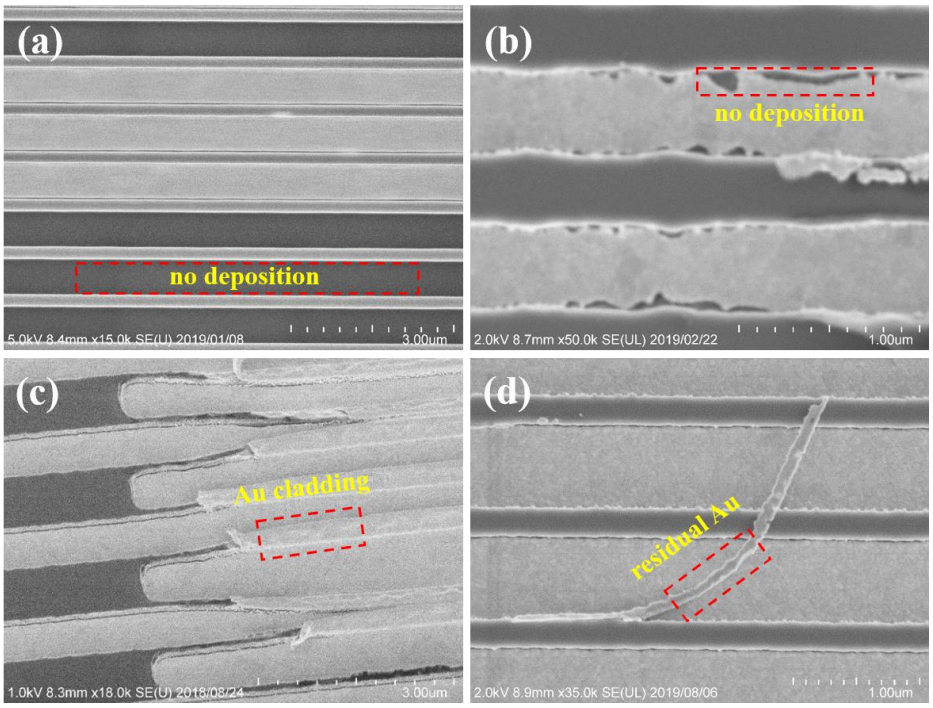

Figure 3.3 The fabricated samples with different imperfections. (a)-(b) Au layers are not uniformly deposited between Si channels. (c) Au cladding occurs after the unsuccessful lift-off. (d) residual Au layer is left after unsuccessful lift-off.

The samples with more than 100 Si channels are difficult to achieve the perfect lift-off without Au cladding and residual Au on the structure, which leads to a short circuit problem. To deal with this problem, the Si channel number (*N*) is reduced which efficiently decreased the short circuit probability. SEM images for the fabricated samples with the Si channel number of 80, 50 and 20 are shown in figure 3.4 (a)-(c), respectively. To clearly show the structure of the sample, the left part and right part of the sample are presented and the middle part of the structure is cropped out.

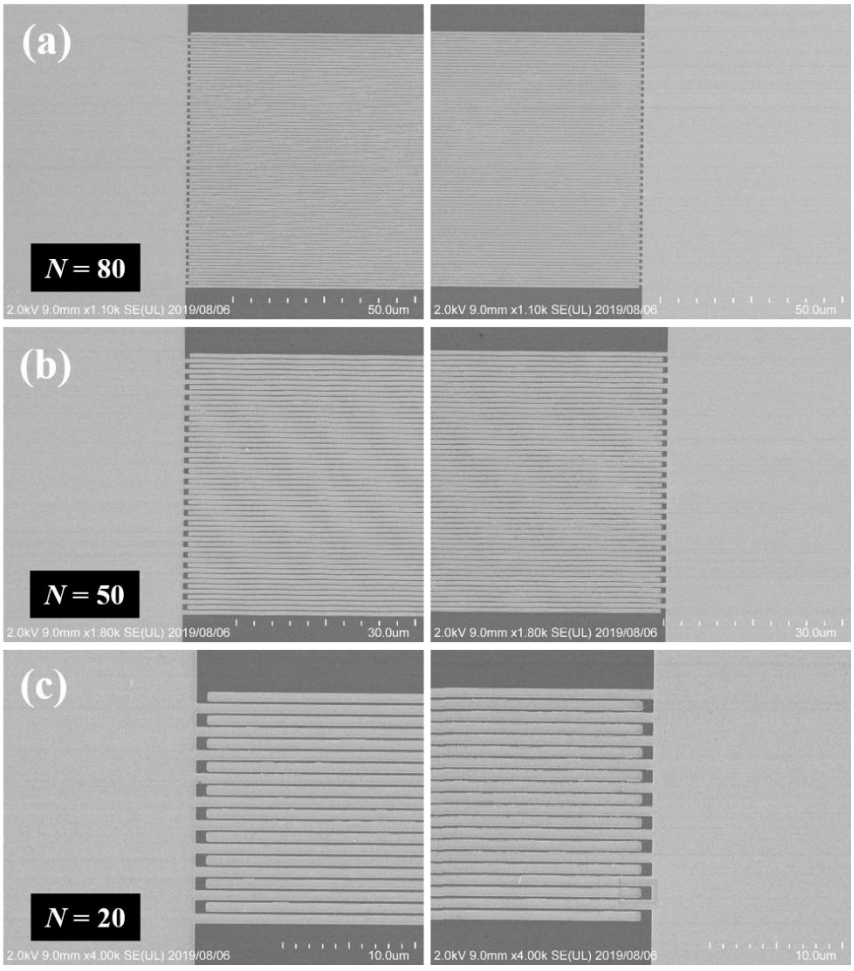

Figure 3.4 The fabricated samples with different Si channel numbers (*N*). (a) *N* = 80, (b) *N* = 50, (c) *N* = 20.

3.2.2 Optical properties

The optical properties of the Si channel-separated interdigitated grating structure are first evaluated through examining the simulated reflectance (R_{sim}), transmittance (T_{sim}) and absorptance (A_{sim}) spectra of the structure, as shown in figure 3.5(a). The period of the structure is 850 nm. The absorptance spectrum exhibits a sharp peak (point P_2) with a modulation of 0.81 (relative to the incident wave) at the resonant wavelength of 1538 nm. Around the resonant wavelength, a reflectance dip also occurs in the simulated and measured (R_{meas}) reflectance spectra, showing an opposite variation to the absorptance spectrum in the C-band. The FWHM of the measured reflectance spectrum reaches as narrow as 23 nm. The facile tunability of the resonant wavelength is demonstrated through changing the period (p) of the structure and the incident angle (θ) of light, as shown in figure 3.5(b). With the increase of p (from 830 to 890 nm) or θ (from 0° to 9°), the resonant wavelength both show a steady redshift. The resonant wavelength is also found to split when θ exceeds 3°, suggesting a strong angular dependence.

To clarify the origin of the strongly resonant and narrowband optical response of the structure, the simulated electric field ($|E|$) distribution at the resonant wavelength (point P_2) is provided in figure 3.5(c). For comparison purpose, the simulated electric field distribution at a non-resonant wavelength (point P_1) is also given in the figure. Points P_1 and P_2 are both defined in figure 3.5(a). The electric field is quite weak at point P_1. In contrast, at point P_2, the electric field enhancement not only occurs at the corners of Au slabs but also appears at the M/S interface, indicating the presence of SPPs. The electric field phase distributions in the x (phase E_x) and z (phase E_z) directions at point P_2 are further investigated, as shown in (iii) and (iv) of figure 3.5(c). The distribution of phase E_z exhibits an antisymmetric behavior between the left and right parts of the structure. While the distribution of phase E_x exhibits a symmetric behavior between the left and right parts, revealing a coupling of surface plasmons between the adjacent Au slabs. The distributions of the time-averaged Poynting vector field (i) and absorption (ii) at point P_2 are shown in figure 3.5(d). The Poynting vector field distribution shows the direction of the light flow and reveals the ability of the structure to

guide and confine light inside the nanoscale volume. The distribution of absorption shows that the light is predominantly absorbed by the Au slabs, and the absorption is much higher near the M/S interface due to the excitation of SPPs.

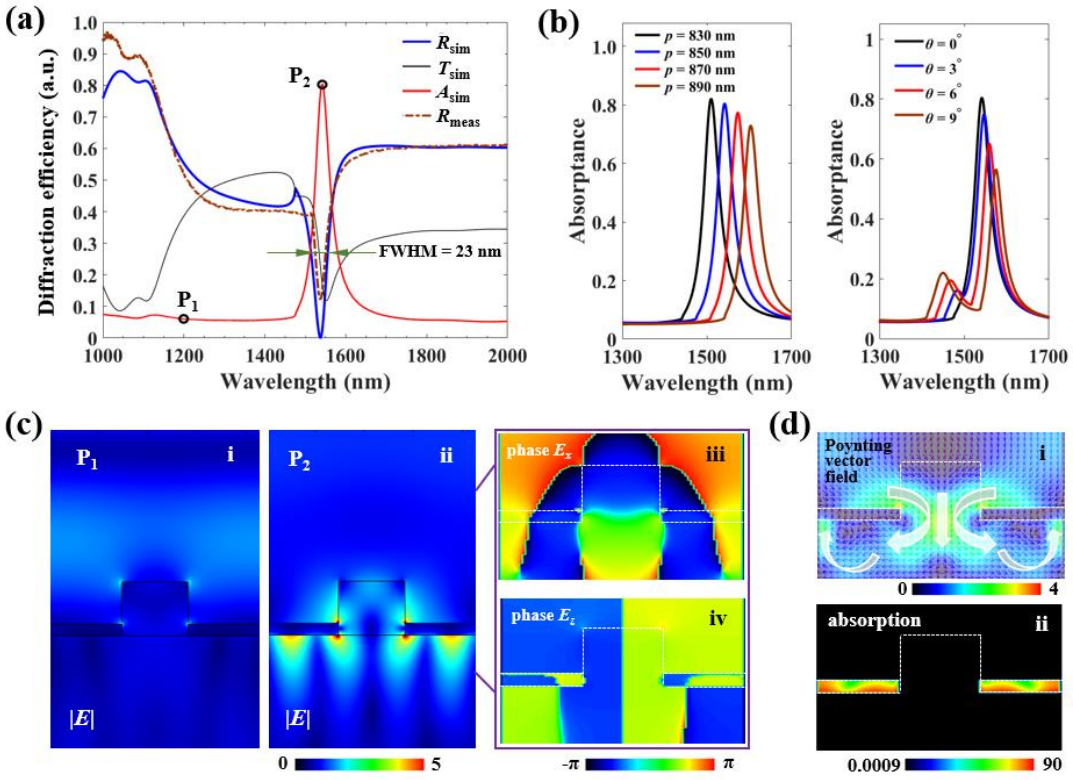

Figure 3.5 The optical properties of the Si channel-separated interdigitated grating structure. (a) The simulated reflectance (R_{sim}), transmittance (T_{sim}) and absorptance (A_{sim}) spectra of the structure. The measured reflectance (R_{meas}) is represented by the brown dashed line. The period of the structure is 850 nm. (b) The simulated absorptance spectra under different periods (p) of the structure and different incident angles (θ) of light. (c) The distributions of electric field ($|E|$) at i: point P_1 and ii: point P_2. Points P_1 and P_2 are defined in (a). The electric field phase distributions in the iii: x and iv: z directions at point P_2. (d) The distributions of i: the time-averaged Poynting vector field and ii: absorption at point P_2.

The measured reflectance spectra for different periods (p) of structure is shown in figure 3.6. The light is normally incident with TM-polarization. It can be seen that the reflectance

dip exhibits a redshift when *p* increases from 820 to 880 nm. The reflectance variation with the period and light wavelength, as shown in the inset, demonstrates that the linearly redshift of the reflectance dip is due to the excitation of SPP mode.

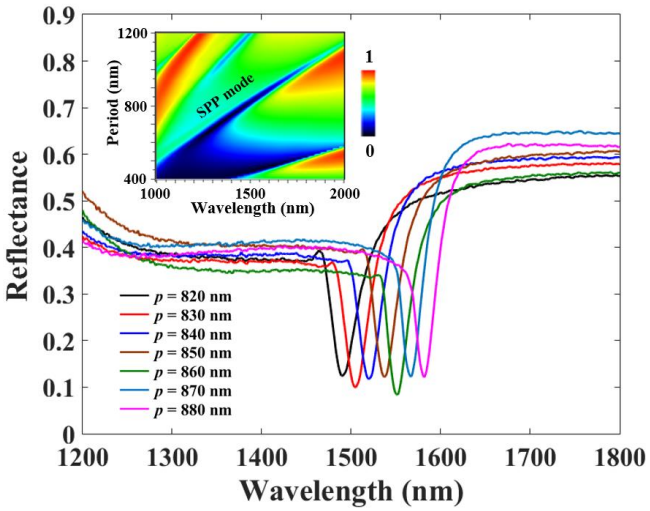

Figure 3.6 The measured reflectance spectra for different periods (*p*) of structure. The light is normally incident with TM-polarization.

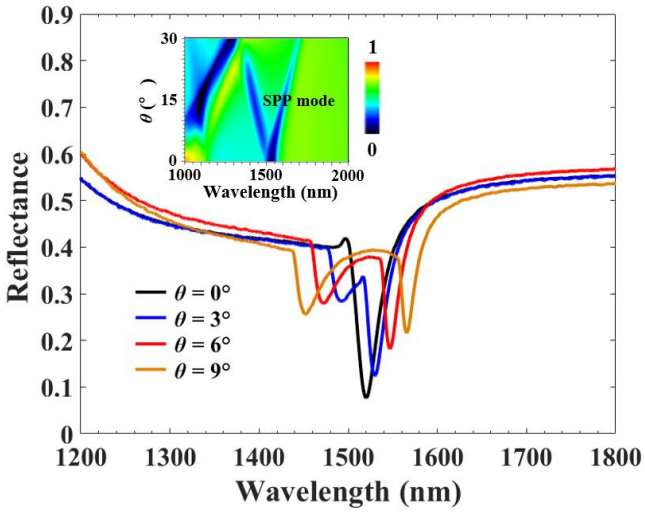

Figure 3.7 The measured reflectance spectra for different periods (*p*) of structure. The period is 840 nm and the light is at TM polarization.

Figure 3.7 shows the measured reflectance spectra for different incident angles (θ) of light. The period of structure is 840 nm, and the light is TM-polarized. The reflectance spectrum exhibits a single dip when the light is normally incident (θ = 0°). While two dips occur in the reflectance spectrum when the incident angle increases from 3° to 9°, and the left dip shows a blueshift with θ and the right dip shows a redshift with θ. This splitting phenomenon is also due to the presence of SPP mode, which is demonstrated by the simulated reflectance variation with incident angle and light wavelength, as shown in the inset.

3.2.3 Photocurrent response

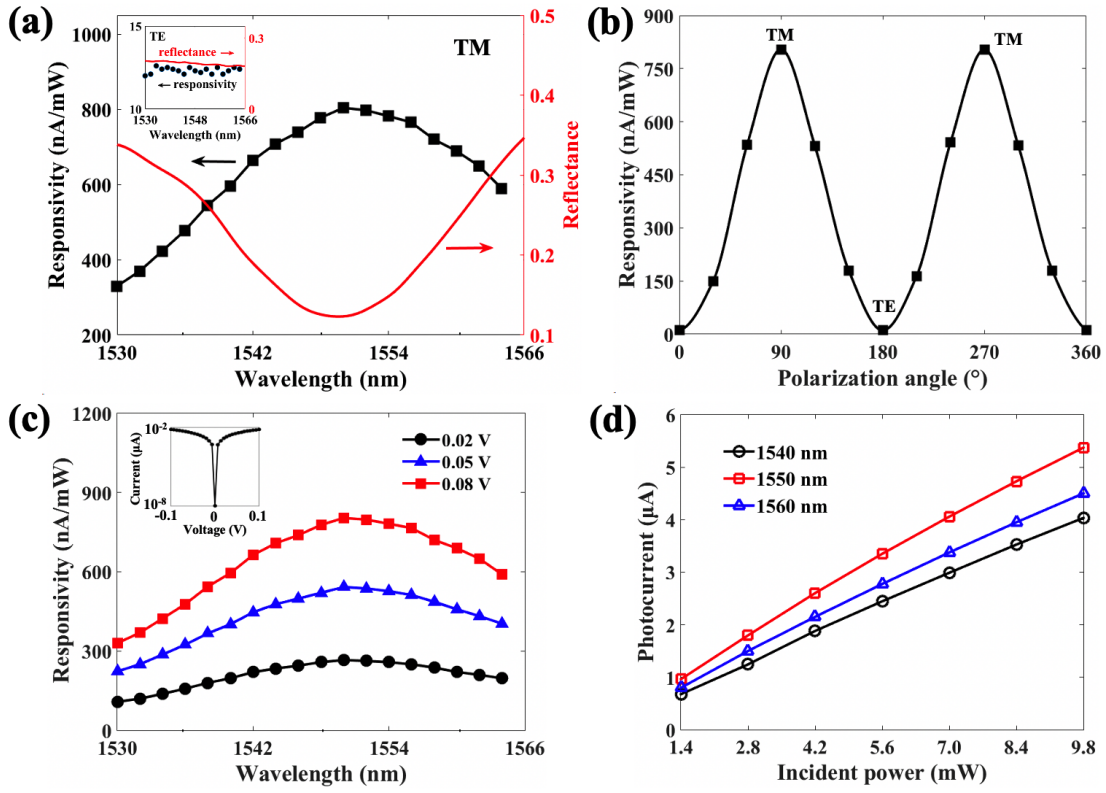

Figure 3.8 The electrical properties of the Si channel-separated interdigitated grating structure under illumination. The period of the structure is 860 nm. Unless otherwise noted, the incident power of light illuminated on the structure is 10 mW. (a) Comparison between the measured responsivity and the measured reflectance spectrum for TM-polarized light. The inset shows the measured responsivity and reflectance for TE-polarized light. The bias

voltage applied on the interdigitated Au gratings is 0.08 V. (b) Dependence of the measured responsivity on the polarization angle of light. 0º is defined as the electric field direction pointing along the Au grating. The bias voltage is 0.08 V. (c) The spectral dependence of measured responsivity under the bias voltages of 0.02, 0.05 and 0.08 V. The inset shows the logarithmic current-voltage curve under dark condition. (d) The relationship between the measured photocurrent and the incident power of light illuminated on the structure for the wavelengths of 1540, 1550 and 1560 nm. The bias voltage is 0.05 V.

In order to evaluate the photocurrent response of photodetectors under illumination, the responsivity (R) is calculated by $R = (i_{ph} - i_d) / P_{in}$, where i_{ph} represents the photocurrent, i_d represents the dark current and P_{in} represents the effective power of light illuminated on the structure. Figure 3.8(a) shows the measured photocurrent responsivity and the measured reflectance spectrum of the structure. The bias voltage applied on the interdigitated Au gratings is 0.08 V. Unless otherwise noted, the incident power of light illuminated on the structure is 10 mW with an effective area of 0.785 mm^2 in this chapter. The measured responsivity exhibits spectral selectivity in the C-band with a peak value of 804 nA/mW that decreases by 59% when the light wavelength is varied by only 20 nm (from 1550 to 1530 nm). The responsivity of our proposed structure is dozens of times of that of the optical antennas [18], planar Tamm plasmonic structure [34], surface plasmon waveguide [35], and Fabry-Perot microcavity [36]. It is also several times of that of the silicon microring resonator [37], deep-trench/thin metal Ni-Si device [38] and traditional Au grating structure [30]. The detail about the comparisons of responsivity among the reported Si-based NIR photodetectors is shown in Table 3.1. The variation in the responsivity is opposite to that in the reflectance spectrum, which indicates that the photocurrent is directly proportional to the absorptance of the structure. It is noted that the absorptance and reflectance spectra of the structure exhibit opposite variations in the C-band, as indicated in figure 3.3(a). In contrast to TM-polarized light, the measured responsivity and reflectance for TE-polarized light are nearly constant over the C-band, as shown in the inset of figure 3.8(a). Figure 3.8(b) further investigates the dependence of responsivity on the polarization angle (β) of light. The responsivity reaches a maximum when the light is TM-polarized (90°, 270°) and drops to a

minimum when the light is TE-polarized (0°, 180°, 360°), exhibiting a $\cos^2\beta$ angular dependence. The ratio of responsivity at TM-polarization to that at TE-polarization almost reaches as high as 64:1.

The spectral dependence of responsivity under different bias voltages is presented in figure 3.8(c). The measured responsivity increases with the bias voltage. The peak value of responsivity is 266 nA/mW for a bias voltage of 0.02 V, but it rapidly reaches 804 nA/mW when the bias voltage rises to 0.08 V. The inset shows a logarithmic current-voltage curve under dark condition. The dark current is as small as 0.01 pA at 0 V and it is still less than 10 nA even the bias voltage increases to 0.1 V. Figure 3.8(d) shows the relationship between the photocurrent and the incident power of light illuminated on the structure for the wavelengths of 1540, 1550 and 1560 nm. The photocurrent linearly increases with the incident power, confirming that the generation of hot electrons predominantly results from the single photon-hot electron interaction [17].

Table 3.1 Comparisons of responsivity among reported Si-based NIR photodetectors

Photodetectors	Wavelength (nm)	Bias Voltage (V)	Responsivity (nA/mW)	Reference
striped waveguides on silicon	1550	0	0.046	[39]
optical antennas	1250	0	~9.7	[18]
Planar Tamm plasmonic structure	1581	0	8.26	[34]
surface plasmon waveguide	1550	-0.1	20.4	[35]
Fabry-Perot microcavity	1550	0	63	[36]
embedding plasmonic nanostructure	1500	0	64	[40]
Cu/p-Si Schottky photodetector	1550	1	80	[41]
plasmonic-crystal-hot-electron structure	900	0	50	[42]
		-4	1.1×10^4	
silicon microring resonator	1550	0	120	[37]
		-15	250	
Silicon Schottky photodetector	1550	-0.45	226	[43]
silicon surface-plasmon Schottky photodetector	1550	0.1	250	[44]
deep-trench/thin-metal Ni-Si device	1550	0	330	[38]

Au grating-Schottky photodetector	1460	0	600	[30]
metamaterial perfect absorber photodetector	1250	0	3.37×10^3	[45]
sub-bandgap hot-hole photodetector	1550	-0.1	1.3×10^4	[46]
all-Si based photoelectronic detector	1150	0	9.45×10^4	[47]
porous silicon photodetector	1550	-6	1.8×10^5	[48]
resonant cavity based photodetector	860	-2	3.86×10^5	[49]
highly doped p-type Si photodetector	1375	0.275	$>10^6$	[50]
Si channel-separated interdigitated grating structure	**1550**	**0.08**	**804**	**this work**

The time-dependent photoresponse of the structure is shown in figure 3.9(a). The light is switched on/off by using a mechanical shutter. To evaluate the photoresponse speed, the rise time (t_r) is defined as the time required for responsivity to increase from 10% to 90% of the saturation value, and the fall time (t_f) is the time required for responsivity to decrease from 90% to 10% of the saturation value [39]. As shown in figures 3.9(b) and (c), the calculated t_r and t_f of the structure are 150 and 155 ms, respectively.

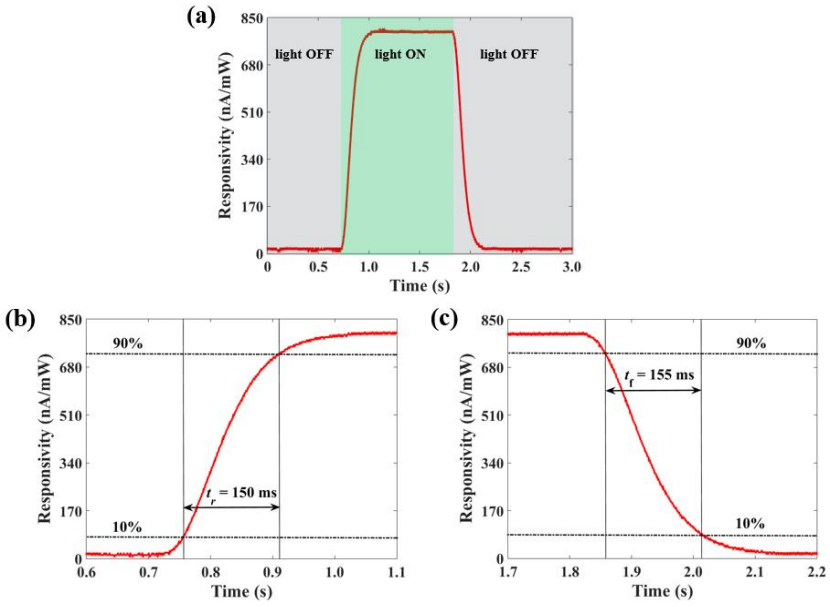

Figure 3.9 (a) The time-dependent photoresponse of the structure. The rise time (t_r) and fall time (t_f) of the structure are shown in (b) and (c), respectively. The period of the structure is 860 nm.

The simulated electric potential distribution in the structure at the bias voltage of V_a and the equivalent circuit diagram are shown in figure 3.10(a). The arrow indicates the direction of the electric field and the arrow length represents its intensity. Since the bias voltage is applied on the adjacent Au slabs, the electric field points horizontally from the positive Au slab to the negative Au slab, and the electric field directions in the adjacent periods are opposite. The equivalent circuit for the structure is a parallel connection, including the resistances of R_{Au}, $R_{Schootky}$ ($R_{Schootky}$ is formed at the M/S interface) and R_{Si} in one period. Figure 3.10(b) shows the simulated current density distribution in the structure and an enlarged view of one periodic unit. The arrow indicates the direction of current flow and the arrow length represents its intensity. Seen from the enlarged view, there are many paths for the current flow. However, the effective current flows horizontally in the structure, from the positive Au slab to the negative Au slab. The current flowing in other paths makes no contribution to the photocurrent due to the inelastic collision and thermalization loss.

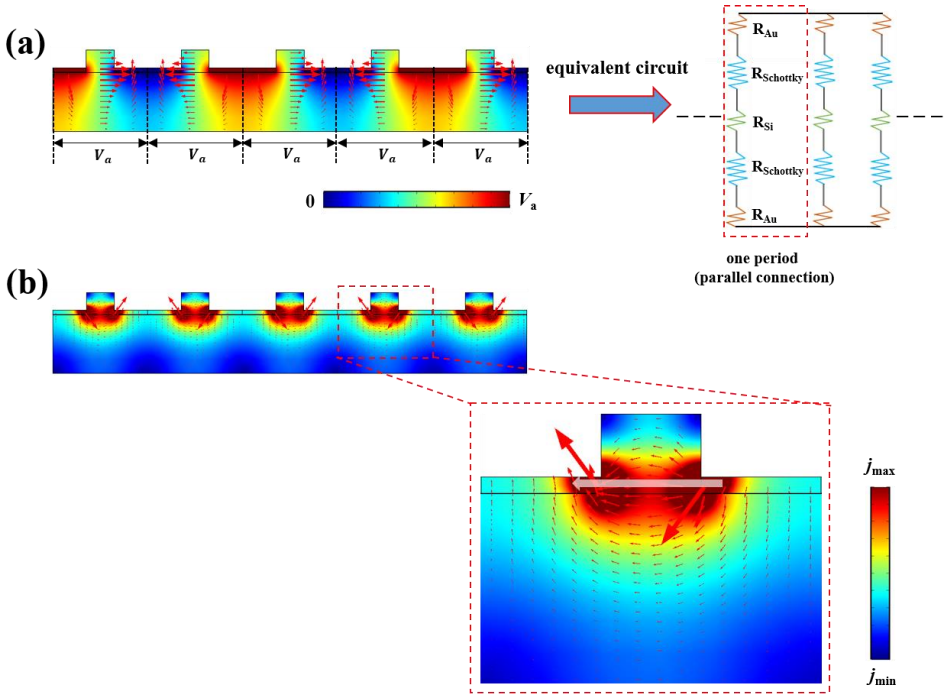

Figure 3.10 (a) The simulated electric potential distribution in the structure at the bias voltage of V_a and the equivalent circuit diagram. The bias voltage is applied on the adjacent Au slabs.

The arrow indicates the direction of the electric field and the arrow length represents its intensity. (b) The simulated current density distribution in the structure and an enlarged view of one periodic unit. The arrows indicate the directions of the current flow and the arrow length represents its intensity.

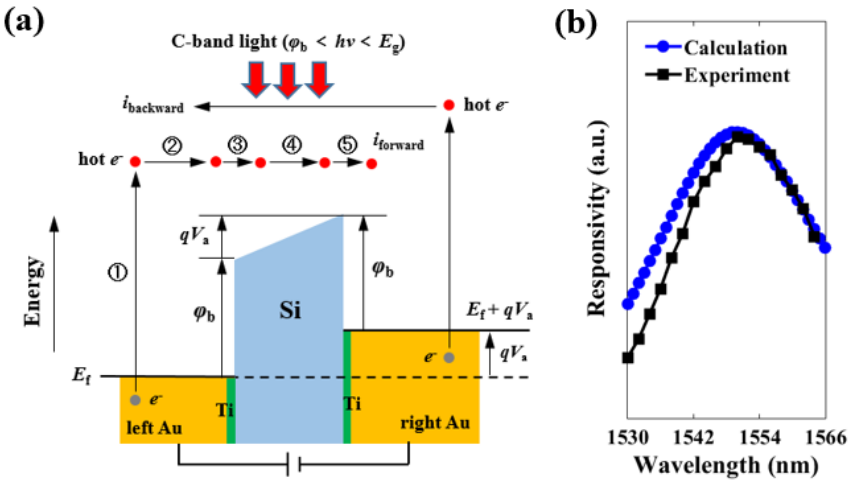

Figure 3.11 (a) The band diagram of one periodic unit of the structure according to Chalabi's model [20]. The Fermi level of the left Au slab is E_f and the Fermi level of the right Au slab is $E_f + qV_a$ upon the application of a bias voltage V_a on the Au slabs. The transports (①②③④⑤) of hot electrons across the M/S/M junctions generate $i_{forward}$ and $i_{backward}$, and the net photocurrent (i_{ph}) is $i_{ph} = i_{forward} - i_{backward}$. (b) The comparison between the calculated and measured responsivities with light wavelength.

To further clarify the generation process of photocurrent in the structure, the band diagram for one periodic unit of the structure is studied according to Chalabi's model [20], as illustrated in figure 3.11(a). Since the photon energy (hv) within the C-band is higher than the Ti/Si barrier height (φ_b = 0.17 eV [11]) and lower than the bandgap of Si (E_g = 1.12 eV), electron-hole pairs cannot be generated in the Si and therefore only hot electrons generated in the Au slabs contribute to photocurrent. Hot electrons transport across the M/S/M junctions generate a forward ($i_{forward}$) and a backward ($i_{backward}$) photocurrent in five consecutive steps, and the net photocurrent (i_{ph}) is calculated by $i_{ph} = i_{forward} - i_{backward}$. As an example of the

generation of $i_{forward}$, the five transport steps of hot electrons are: ① generation in the Au slab, ② movement to the first M/S interface, ③ crossing of the first M/S barrier, ④ transport through the Si channel and ⑤ crossing of the second M/S barrier and injection into the adjacent Au slab. The details about how to calculate the transport probability for each step and the photocurrent responsivity of the structure are clarified in the theoretical calculation section. Since the structure is highly symmetrical, hot electrons transports generate an equal $i_{forward}$ and $i_{backward}$ at the bias voltage of 0 V and this leads i_{ph} = 0 A. However, the M/S/M junctions and the Fermi levels of the adjacent Au slabs become asymmetrical upon the application of a bias voltage V_a on the Au slabs, thus generating an unequal $i_{forward}$ and $i_{backward}$ and producing a net photocurrent i_{ph}. According to this model, the theoretical calculation reproduces the spectral dependence of responsivity and exhibits the same spectral selectivity with the experiment in the C-band, as shown in figure 3.11(b).

3.3 Theoretical calculation of photocurrent response

Hot electron generation and transport in each periodic unit of the Si channel-separated interdigitated grating structure is the same. For one periodic unit, since hot electrons are simultaneously generated in the left and right Au slabs after receiving the incident photon energy, both forward and backward photocurrents that flow in the opposite directions are generated. According to Chalabi's model [20], the transports of hot electrons during the generation of forward and backward photocurrents can be separated into five steps with specific probabilities (P): ① generation in the Au slab, ② movement to the first M/S interface (P_1), ③ crossing of the first M/S barrier (P_2), ④ transport through the Si channel (P_3) and ⑤ crossing of the second M/S barrier and injection into the adjacent Au slab (P_4). The theoretical calculation for the generation of forward photocurrent is clarified in the following, and the same procedure can be used to calculate the backward photocurrent.

(1) Generation in left Au slab

We use an optical model to calculate the hot electron generation rate in the Au slabs of the structure. The electric field distribution is first simulated using the Finite Element Method (COMSOL) technique. The absorbed power density ($abs(\vec{r},\omega)$) is then linked to the local Ohmic loss in the metal, which can be expressed as [52,53]

$$abs(\vec{r},\omega) = \frac{\varepsilon_i \omega \left|\vec{E}(\vec{r},\omega)\right|^2}{2}, \tag{1}$$

where $\vec{r}$ represents the position, ω represents the angular frequency of light, ε_i represents the imaginary part of the permittivity for Au, and $\vec{E}(\vec{r},\omega)$ represents the electrical field. Assuming one absorbed photon of light generates one hot electron-hole pair, the density of hot electrons is expressed as

$$N_e(\vec{r},\omega) = N_h(\vec{r},\omega) = N_{\mathrm{ph}}(\vec{r},\omega) = \frac{abs(\vec{r},\omega)}{\hbar\omega}. \tag{2}$$

The hot electron generation rate $G(\vec{r},\omega)$ can be then calculated by [52,53]

$$G(\vec{r},\omega) = \frac{abs(\vec{r},\omega)}{\hbar\omega} = \frac{\varepsilon_i \left|\vec{E}(\vec{r},\omega)\right|^2}{2\hbar}. \tag{3}$$

where $\hbar$ represents the reduced Planck constant. The initial energy distribution $D(E)$ of the generated hot electrons is described by the multiplication of the joint density of states (DOS) at the initial and final energies, as given by [53,54]

$$D(E) = \frac{\rho(E-h\nu)f(E-h\nu)\rho(E)[1-f(E)]}{\int_0^\infty \rho(E-h\nu)f(E-h\nu)\rho(E)[1-f(E)]dE}, \tag{4}$$

$$\rho(E) = a\sqrt{E}, \tag{5}$$

$$f(E) = \frac{1}{1+\exp\left(\frac{E-E_F}{k_B T}\right)}, \tag{6}$$

where E represents hot electron's energy ($0 < E < h\nu$), $\rho(E\text{-}h\nu)$ represents the parabolic electron DOS at the initial energy level, $\rho(E)$ represent the parabolic electron DOS at the final energy level, $f(E\text{-}h\nu)$ and $f(E)$ represents their corresponding Fermi distribution functions, a is a constant, E_F represents the Fermi level at thermal equilibrium, k_B represents the Boltzmann constant, and T represents the temperature.

(2) Movement to the left M/S interface

The probability P_1 for hot electrons successfully reaching the M/S interface without losing energy through the inelastic collision is expressed as [53,55]

$$P_1 = \frac{1}{2\pi}\int_{\theta_1}^{\theta_2} \exp\left(-\frac{d}{\lambda_e \cos\theta}\right) d\theta, \tag{7}$$

where θ represents hot electron's moving angle, θ_1 represents the minimum accepting angle, θ_2 represents the maximum accepting angle, λ_e represents the mean free path of hot electrons in Au, and d represents the distance between the position of hot electrons and the M/S interface. With hot electron generation rate $G(\vec{r},\omega)$, the initial energy distribution $D(E)$, and the probability for hot electrons reaching the M/S interface P_1, the flux $F(\vec{r},\omega,E)$ of hot electrons that successfully reach the M/S interface can be expressed as

$$F(\vec{r},\omega,E) = G(\vec{r},\omega)D(E)P_1. \tag{8}$$

(3) Crossing of the left M/S barrier

The kinetic energy $E_{Au,l}$ of the hot electron that is generated in the left Au slab ($E_{Au,l}$) is expressed as

$$E_{Au,l} = E_{F,l} + E, \tag{9}$$

where $E_{F,l}$ represents the Fermi level for the left Au slab and E ($0 < E < h\nu$) represents hot electron's energy above the Fermi level. Hot electron's momentum for the left Au slab $k_{Au,l}$ can be expressed as

$$k_{\mathrm{Au},l} = \frac{\sqrt{E_{\mathrm{Au},l} \cdot 2m_e^*}}{\hbar} = \frac{\sqrt{\left(E_{\mathrm{F},l} + E\right) \cdot 2m_e^*}}{\hbar}, \tag{10}$$

where m_e^* represents the effective mass of an electron and $\hbar$ represents the reduced Planck constant. After crossing the first M/S barrier, hot electron's kinetic energy in the left side of the semiconductor $E_{\mathrm{Si},l}$ is expressed as

$$E_{\mathrm{Si},l} = E - \varphi_{\mathrm{b}}, \tag{11}$$

where φ_{b} represents the barrier height. Hot electron's momentum in the left side of the semiconductor $k_{\mathrm{Si},l}$ can be calculated as

$$k_{\mathrm{Si},l} = \frac{\sqrt{E_{\mathrm{Si},l} \cdot 2m_e^*}}{\hbar} = \frac{\sqrt{(E - \varphi_{\mathrm{b}}) \cdot 2m_e^*}}{\hbar}. \tag{12}$$

As shown in figure 3b, the hot electron that successfully reaches the M/S interface can cross the Schottky barrier only if its momentum component in the x direction $k_{\mathrm{Au},x}$ is larger than the threshold k_{es}, which defines an escape cone. The probability P_{esc} for hot electrons being in the escape cone can be expressed as

$$P_{\mathrm{esc}} = \frac{d\Omega}{4\pi} = \frac{2\pi \sin\theta d\theta}{4\pi} = \frac{k_y}{2k_{\mathrm{Au},l}\sqrt{k_{\mathrm{Au},l}^2 - k_y^2}}, \tag{13}$$

where k_y represents the momentum component in the y direction. Since the momentum of hot electrons in the y direction is reserved, it can be obtained that $k_{\mathrm{Au},y} = k_{\mathrm{Si},y} = k_y$. The probability P_{ref} for hot electrons crossing the Schottky barrier without reflection is given by

$$P_{\mathrm{ref}} = \frac{4k_{(\mathrm{Au},l)_x}k_{(\mathrm{Si},l)_x}}{\left(k_{(\mathrm{Au},l)_x} + k_{(\mathrm{Si},l)_x}\right)^2} = \frac{4\sqrt{\left(k_{\mathrm{Au},l}^2 - k_y^2\right)\left(k_{\mathrm{Si},l}^2 - k_y^2\right)}}{\left(\sqrt{k_{\mathrm{Au},l}^2 - k_y^2} + \sqrt{k_{\mathrm{Si},l}^2 - k_y^2}\right)^2}, \tag{14}$$

where $k_{(\mathrm{Si},l)x}$ represents the x-component of $k_{\mathrm{Si},l}$ and $k_{(\mathrm{Au},l)x}$ represents the x-component of $k_{\mathrm{Au},l}$. The transmission probability P_2 for hot electrons crossing the first Schottky barrier is expressed as

$$P_2 = \int_0^{K_{\mathrm{Si},l}(E)} P_{\mathrm{esc}} P_{\mathrm{ref}} dk_y = \int_0^{K_{\mathrm{Si},l}(E)} \frac{2\sqrt{k_{\mathrm{Si},l}^2 - k_y^2}}{\left(\sqrt{k_{\mathrm{Au},l}^2 - k_y^2} + \sqrt{k_{\mathrm{Si},l}^2 - k_y^2}\right)^2} \frac{k_y}{k_{Au,l}} dk_y \,, \tag{15}$$

where $K_{\mathrm{Si},l}(E)$ represents the maximum of $k_{\mathrm{Si},l}$ and it can be expressed as

$$K_{\mathrm{Si},l}(E) = \left(k_{\mathrm{Si},l}\right)_{max} = \frac{\sqrt{\left(E_{\mathrm{Si},l}\right)_{max} \cdot 2m_e^*}}{\hbar} = \frac{\sqrt{(\hbar\nu - \varphi_{\mathrm{b}}) \cdot 2m_e^*}}{\hbar}. \tag{16}$$

(4) Transport through the Si channel

After crossing the left M/S barrier, hot electrons will transport from one side to the other side of the semiconductor. The probability P_3 for hot electrons transporting through the semiconductor without scattering and successfully reaching the other side of semiconductor is given by [52]

$$P_3 = e^{-\frac{w}{\lambda_m}} \tag{17}$$

where w represents the width of the Si channel, λ_m represents the mean free path of hot electrons in Si.

(5) Crossing of the right M/S barrier

The hot electron's kinetic energy $E_{\mathrm{Si},r}$ that reaches the right side of the semiconductor is expressed as

$$E_{\mathrm{Si},r} = E - \varphi_{\mathrm{b}} + eV, \tag{18}$$

where e represents the electron charge and V represents the bias voltage. The momentum of hot electrons in the right side of the semiconductor $k_{\mathrm{Si},r}$ is expressed as

$$k_{\mathrm{Si},r} = \frac{\sqrt{E_{\mathrm{Si},r} \cdot 2m_e^*}}{\hbar} = \frac{\sqrt{(E - \varphi_{\mathrm{b}} + eV) \cdot 2m_e^*}}{\hbar}, \tag{19}$$

The kinetic energy of hot electrons in the right Au slab ($E_{\mathrm{Au},r}$) is given by

$$E_{\mathrm{Au},r} = E_{\mathrm{F},r} + E + eV, \tag{20}$$

where $E_{\mathrm{F},r}$ represents the Fermi level of the right Au slab. The momentum of hot electrons in the right Au represents ($k_{\mathrm{Au},r}$) is given by

$$k_{\mathrm{Au},r} = \frac{\sqrt{E_{\mathrm{Au},r} \cdot 2m_e^*}}{\hbar} = \frac{\sqrt{\left(E_{\mathrm{F},r} + E + eV\right) \cdot 2m_e^*}}{\hbar}. \tag{21}$$

The probability P_4 for hot electrons crossing the second Schottky barrier is calculated analogously to Eq. 15,

$$P_4 = \int_0^{K_{\mathrm{Si},r}(E)} \frac{2\sqrt{k_{\mathrm{Au},r}^2 - k_y^2}}{\left(\sqrt{k_{\mathrm{Si},r}^2 - k_y^2} + \sqrt{k_{\mathrm{Au},r}^2 - k_y^2}\right)^2} \frac{k_y}{k_{\mathrm{Si},r}} dk_y, \tag{22}$$

where $K_{\mathrm{Si},r}(E)$ represents the maximum of $k_{\mathrm{Si},r}$ and it can be given by

$$K_{\mathrm{Si},r}(E) = \left(k_{Si,r}\right)_{max} = \frac{\sqrt{\left(E_{\mathrm{Si},r}\right)_{max} \cdot 2m_e^*}}{\hbar} = \frac{\sqrt{(\hbar\nu - \varphi_{\mathrm{b}} + eV) \cdot 2m_e^*}}{\hbar}. \tag{23}$$

With the total transport probability ($P_2P_3P_4$), we can calculate the internal quantum efficiency (IQE, defined as η) for the generation of the forward photocurrent [52,53]

$$\eta_{\mathrm{forward}} = \frac{1}{E_{\mathrm{ph}}} \int_{\varphi_{\mathrm{b}}}^{E_{\mathrm{ph}}} P_2 P_3 P_4 dE, \tag{24}$$

where E_{ph} represents the photon energy of light. The internal quantum efficiency for the generation of backward photocurrent can be derived in an analogous manner. The net photocurrent (i_{ph}) can be given by [52,53,57]

$$i_{\mathrm{ph}} = eN|F(\vec{r},\omega,E)_{\mathrm{forward}}\eta_{\mathrm{forward}} - F(\vec{r},\omega,E)_{\mathrm{backward}}\eta_{\mathrm{backward}}|, \quad (25)$$

where N represents the period number. The responsivity R is calculated by $R = i_{ph} / P_{inc}$, where P_{inc} represents the incident power of light illuminated on the structure. The responsivity and photocurrent can also be calculated by [58]: $R = eA|\eta_{\mathrm{farward}} - \eta_{\mathrm{backward}}|/\hbar\omega$ and $i_{\mathrm{ph}} = RP_{\mathrm{inc}}$, where A represents the optical absorptance.

According to this model, we can theoretically calculate the photocurrent responsivity of the structure. Figure 3.12(a) shows the calculated normalized hot electron generation rate in one periodic unit of the structure. As expected, hot electrons are generated in the Au slabs and predominantly generated near the Au/Si interface due to the excitation of SPPs. Figure 3.12(b) shows the calculated initial energy distribution $D(E)$ of hot electrons that are generated in the Au slabs with a light wavelength of 1530 nm. The shaded area represents the proportion of hot electrons with energy above the Au/Si barrier height (φ_b). Figure 3.12(c) shows the probability (P_1) for hot electrons reaching the Au/Si interface after their generations, which depends on the moving angle of hot electron, the distance between the hot electrons and the Au/Si interface and the mean free path of hot electrons in Au. Since the acceptance angle range (θ_2 -θ_1) at the bottom corner (close to the Au/Si interface) of the Au slab in the structure is as large as 270°, the corresponding P_1 reaches a peak with a value of 0.75. The value of P_1 for the inner edges close to the Au/Si interface is 0.5 (acceptance angle range θ_2 -θ_1 = 180°) and decreases gradually with the distance away from the interface.

Figure 3.12(d) depicts the hot electrons states on a constant energy contour in the Au slab and the Si channel, showing the allowed terminations of hot electron momentum at a certain energy [14,21]. The escape momentum k_{es} (minimum momentum that is required for crossing the Schottky barrier) is shown as $k_{\mathrm{es}} = \sqrt{2m_e^*\varphi_{\mathrm{b}}}/\hbar$. The hot electron that reaches

the Au/Si interface can cross the Schottky barrier only if their x-component momenta $k_{Au,x}$ is larger than k_{es}, which defines an escape cone as indicated by the shaded area. Ω is defined as the maximum angle for the momentum k_{Au} within the escape cone. The maximum momentum component in the y-direction of hot electrons in the Si channel is noted $(k_{Si,y})_{max}$ and can be expressed as $(k_{Si,y})_{max} = (k_{Au})_{\Omega} \cdot \sin\Omega$.

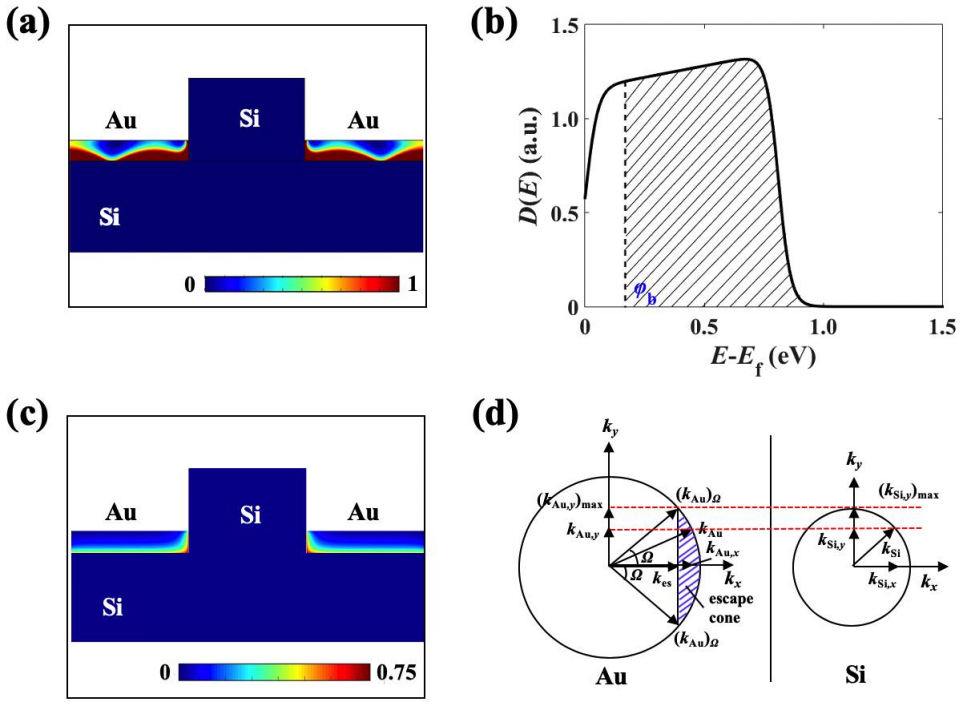

Figure 3.12 (a) The calculated normalized hot electron generation rate in one periodic unit of the structure. (b) The initial energy distribution $D(E)$ of hot electrons that are generated in the Au slab with a light wavelength of 1530 nm. (c) The probability (P_1) for the generated hot electrons reaching the Au/Si interface. (d) Schematic illustration of the constant energy contours for hot electrons in the Au slab and the Si channel. The circles indicate the outlines of the allowed hot electron momenta at a certain energy E. Only hot electrons whose momenta are comprised within the escape cone (the shaded area) can be injected into the Si.

The calculated internal quantum efficiency (IQE) for the generation of the forward and backward photocurrents in the structure is shown in figure 3.13(a). Due to the symmetry of

the structure, the variations of the forward and backward IQEs show a symmetric behavior. The total IQE ($IQE_{forward}$ - $IQE_{backward}$) is 0 at the bias voltage of 0 V, but it rapidly increases with the bias voltage. When IQE reaches the maximum ($IQE_{forward}$ reaches the maximum and $IQE_{backward}$ falls to 0 or vice versa) at a certain voltage, the responsivity obtains the maximum value. The calculated spectral dependence of responsivity for the structure is shown in figure 3.13(b), which also exhibits spectral selectivity in the C-band. The calculated responsivity reaches the peak with a value of 813 nA/mW at the resonant wavelength of 1550 nm, matching well with the experiment result (804 nA/mW).

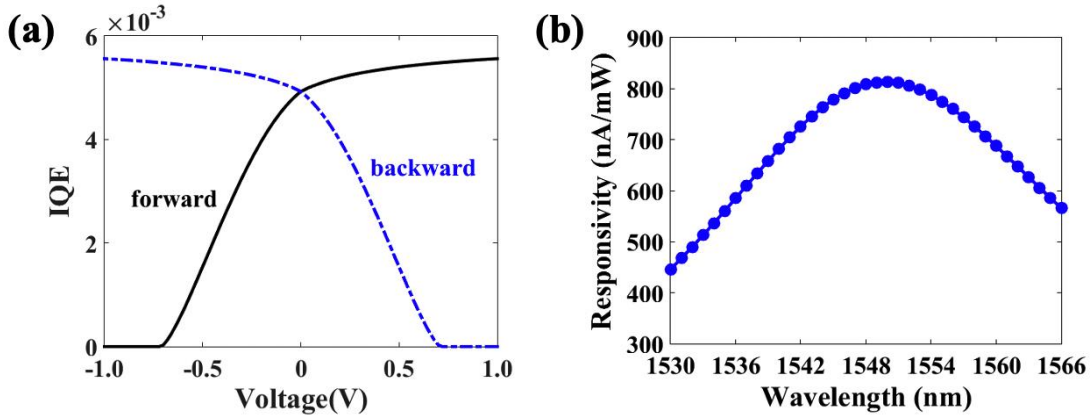

Figure 3.13 (a) The dependence of calculated IQE on the bias voltage for the generation of the forward and backward photocurrents. (b) The calculated responsivity variation with light wavelength. The structure dimensions are w = 280 nm, h = 200 nm, t = 40 nm and p = 860 nm. The light is normally incident with TM-polarization and the incident power illuminated on the structure is 10 mW with an effective area of 0.785 mm^2. The bias voltage is 0.08 V.

3.4 Discussion

In summary, a Si channel-separated interdigitated grating structure is investigated both theoretically and experimentally in this paper. The structure efficiently guides and confines light in the structure through the excitation of SPPs at the M/S interface, leading to strongly resonant and narrowband optical response and strong field enhancements. By taking

advantage of the optical response and the generation of hot electrons, the structure achieves spectrally selective photodetection in the C-band. The measured FWHM reaches as narrow as 23 nm and the measured responsivity reaches as high as 804 nA/mW at the resonant wavelength of 1550 nm and the bias voltage of 0.08 V, showing a competitive performance with previously reported Si-based NIR photodetectors.

References

[1] J. A. Schuller, E. S. Barnard, W. Cai, Y. C. Jun, J. S. White, and M. L. Brongersma, "Plasmonics for extreme light concentration and manipulation," *Nat. Mater*. **9**, 193 (2010)

[2] D. K. Gramotnev, and S. I. Bozhevolnyi, "Plasmonics beyond the diffraction limit," *Nat. Photonics* **4**, 83 (2010)

[3] M. I. Stockman, "Nanoplasmonics: past, present, and glimpse into future," *Opt. Express* **19**, 22029 (2011)

[4] J. P. Camden, J. A. Dieringer, J. Zhao, and R. P. Van Duyne, "Controlled plasmonic nanostructures for surface-enhanced spectroscopy and sensing," *Accounts. Chem. Res.* **41**, 1653 (2008)

[5] E. J. R. Vesseur, R. de Waele, M. Kuttge, and A. Polman, "Direct observation of plasmonic modes in Au nanowires using high-resolution cathodoluminescence spectroscopy," *Nano Lett.* **7**, 2843 (2007)

[6] P. Narang, R. Sundararaman, and H. A. Atwater, "Plasmonic hot carrier dynamics in solid-state and chemical systems for energy conversion," *Nanophotonics* **5**, 96 (2016)

[7] S. Foroutan, and H. Baghban, "Theory of plasmonic quantum-dot-based intermediate band solar cells" *Appl. Opt.* **55**, 3405 (2016)

[8] Y. T. Lim, M. Y. Cho, J. K. Kim, S. Hwangbo, and B. H. Chung, "Plasmonic magnetic nanostructure for bimodal imaging and photonic-based therapy of cancer cells" *ChemBioChem* **8**, 2204 **(**2007)

[9] X. Huang, I. H. El-Sayed, W. Qian, and M. A. El-Sayed, "Cancer cell imaging and photothermal therapy in the near-infrared region by using gold nanorods," *J. Am. Chem. Soc.* **128**, 2115 (2006)

[10] Y. L. Ho, L. C. Huang, and J. J. Delaunay, "Spectrally selective photocapacitance modulation in plasmonic nanochannels for infrared imaging," *Nano Lett*. **16**, 3094 (2016)

[11] Y. L. Ho, Y. H. Tai, J. K. Clark, Z.Y. Wang, P. K. Wei, and J. J. Delaunay, "Plasmonic Hot-Carriers in Channel-Coupled Nanogap Structure for Metal–Semiconductor Barrier Modulation and Spectral-Selective Plasmonic Monitoring," *ACS Photonics* **5**, 2617 (2018)

[12] S. S. Mousavi, A. Stöhr, and P. Berini, "Plasmonic photodetector with terahertz electrical bandwidth," *Appl. Phys. Lett*. **104**, 143112 (2014)

[13] I. Goykhman, U. Sassi, B. Desiatov, N. Mazurski, S. Milana, D. de. Fazio, and A. C. Ferrari, "On-chip integrated, silicon–graphene plasmonic Schottky photodetector with high responsivity and avalanche photogain," *Nano Lett.* **16**, 3005 (2016)

[14] B. Y. Zheng, H. Zhao, A. Manjavacas, M. McClain, P. Nordlander, and N. J. Halas, "Distinguishing between plasmon-induced and photoexcited carriers in a device geometry," *Nat. Commun.* **6**, 7797 (2015).

[15] B. Feng, J. Zhu, B. Lu, F. Liu, L. Zhou, and Y. Chen, "Achieving Infrared detection by all-Si plasmonic hot-electron detectors with high detectivity," *ACS Nano* **13**, 8433 (2019)

[16] S. Mubeen, G. Hernandez-Sosa, D. Moses, J. Lee, and M. Moskovits, "Plasmonic photosensitization of a wide band gap semiconductor: converting plasmons to charge carriers," *Nano Lett.* **11**, 5548 (2011)

[17] T. Gong, and J. N. Munday, "Angle-independent hot carrier generation and collection using transparent conducting oxides," *Nano Lett.* **15**, 147 (2014)

[18] M. W. Knight, H. Sobhani, P. Nordlander, and N. J. Halas, "Photodetection with active optical antennas," *Science* **332**, 702 (2011)

[19] K. T. Lin, H. L. Chen, Y. S. Lai, and C. C. Yu, "Silicon-based broadband antenna for high responsivity and polarization-insensitive photodetection at telecommunication wavelengths," *Nat. Commun*. **5**, 3288 (2014)

[20] H. Chalabi, D. Schoen, and M. L. Brongersma, "Hot-electron photodetection with a plasmonic nanostripe antenna," *Nano Lett*. **14**, 1374 (2014)

[21] M. Fukuda, T. Aihara, K. Yamaguchi, Y. Y. Ling, K. Miyaji, and M. Tohyama, "Light detection enhanced by surface plasmon resonance in metal film," *Appl. Phys. Lett.* **96**, 153107 (2010)

[22] W. Li, and J. Valentine, "Metamaterial perfect absorber based hot electron photodetection," *Nano Lett*. **14**, 3510 (2014).

[23] Y. Xie, L. Wei, G. Wei, Q. Li, D. Wang, Y. Chen, and J. Jiao, "A self-powered UV photodetector based on TiO_2 nanorod arrays," *Nanoscale. Res. Lett.* **8**, 188 (2013)

[24] J. F. Wang, M. S. Gudiksen, X. Duan, Y. Cui, and C. M. Lieber, "Highly polarized photoluminescence and photodetection from single indium phosphide nanowires," *Science* **293**, 1455 (2001)

[25] H. Kind, H. Yan, B. Messer, M. Law, and P. Yang, "Nanowire ultraviolet photodetectors and optical switches," *Adv. Mater*. **14**, 158 (2002)

[26] M. W. Knight, Y. Wang, A. S. Urban, A. Sobhani, B. Y. Zheng, P. Nordlander, and N. J. Halas, "Embedding plasmonic nanostructure diodes enhances hot electron emission," *Nano Lett.* **13**, 1687 (2013)

[27] I. Goykhman, B. Desiatov, J. Khurgin, J. Shappir, and U. Levy, "Locally oxidized silicon surface-plasmon Schottky detector for telecom regime," *Nano Lett*. **11**, 2219 (2011)

[28] I. Goykhman, B. Desiatov, J. Khurgin, J. Shappir, and U. Levy, "Waveguide based compact silicon Schottky photodetector with enhanced responsivity in the telecom spectral band," *Opt. Express* **20**, 28594 (2012)

[29] M. Casalino, M. Iodice, L. Sirleto, I. Rendina, and G. Coppola, "Asymmetric MSM sub-bandgap all-silicon photodetector with low dark current," *Opt. Express* **21**, 28072 (2013)

[30] A. Sobhani, M. W Knight, Y. Wang, B. Zheng, N. S. King, L. V. Brown, Z. Fang, P. Nordlander, and N. J. Halas, "Narrowband photodetection in the near-infrared with a plasmon-induced hot electron device," *Nat. Commun*. **4**, 1643 (2013)

[31] H. Chalabi, D. Schoen, and M. L. Brongersma, "Hot-electron photodetection with a plasmonic nanostripe antenna," *Nano Lett.* **14**, 1374 (2014)

[32] K. Wu, Y. Zhan, C. Zhang, S. Wu, and X. Li, "Strong and highly asymmetrical optical absorption in conformal metal-semiconductor-metal grating system for plasmonic hot-electron photodetection application," *Sci. Rep*. **5**, 14304 (2015)

[33] K. T. Lin, H. L. Chen, Y. S. Lai, and C. C. Yu, "Silicon-based broadband antenna for high responsivity and polarization-insensitive photodetection at telecommunication wavelengths," *Nat. Commun*. **5**, 3288 (2014).

[34] Z. Wang, J. K. Clark, Y. L. Ho, and J. J. Delaunay, "Hot-electron photodetector with wavelength selectivity in near-infrared via Tamm plasmon," *Nanoscale* **11**, 17407 (2019)

[35] A. Akbari, R. N. Tait, and P. Berini, "Surface plasmon waveguide Schottky detector," *Opt. Express* **18**, 8505 (2010)

[36] M. Casalino, G. Coppola, M. Iodice, I. Rendina, and L. Sirleto, "Critically coupled silicon Fabry-Perot photodetectors based on the internal photoemission effect at 1550 nm," *Opt. Express* **20**, 12599 (2012)

[37] H. Chen, X. Luo, and A. W. Poon, "Cavity-enhanced photocurrent generation by 1.55 μm wavelengths linear absorption in a pin diode embedded silicon microring resonator," *Appl. Phys. Lett*. **95**, 171111 (2009)

[38] T. Y. Lin, K. T. Lin, C. C. Lin, Y. W. Lee, L. T. Shiu, W. Y. Chen, and H. L. Chen, "Magnetic fields affect hot electrons in silicon-based photodetectors at telecommunication wavelengths," *Mater. Horiz.* **6**, 1156 (2019)

[39] S. Okahisa, K. Nakayama, Y. Nakayama, Y. Ishii, and M. Fukuda, "Guiding Properties of 1.31- and 1.55-μm-Wavelength Surface Plasmon Polaritons on Striped Waveguides on Silicon and Their Wavelength-Selective Detection," *J. Lightwave. Technol.* **35**, 2702-2711 (2017)

[40] M. W. Knight, Y. Wang, A. S. Urban, A. Sobhani, B. Y. Zheng, P. Nordlander, N. J. Halas, "Embedding plasmonic nanostructure diodes enhances hot electron emission," *Nano Lett.* **13**, 1687-1692 (2013)

[41] M. Casalino, L. Sirleto, M. Iodice, N. Saffioti, M. Gioffrè, I. Rendina, and G. Coppola, "Cu/p-Si Schottky barrier-based near infrared photodetector integrated with a silicon-on-insulator waveguide," *Appl. Phys. Lett.* **96**, 241112 (2010)

[42] F. P. García de Arquer, A. Mihi, and G. Konstantatos, “Large-area plasmonic-crystal–hot-electron-based photodetectors,” *ACS photonics* **2**, 950-957 (2015)

[43] Y. P. Huang, and L. A. Wang, “In-line silicon Schottky photodetectors on silicon cored fibers working in 1550 nm wavelength regimes,” *Appl. Phys. Lett*. **106**, 191106 (2015)

[44] I. Goykhman, B. Desiatov, J. Khurgin, J. Shappir, and U. Levy, “Locally oxidized silicon surface-plasmon Schottky detector for telecom regime,” *Nano Lett*. **11**, 2219-2224 (2011)

[45] W. Li, and J. Valentine, “Metamaterial perfect absorber based hot electron photodetection,” *Nano Lett*. **14**, 3510-3514 (2014)

[46] M. Alavirad, A. Olivieri, L. Roy, and P. Berini, “High-responsivity sub-bandgap hot-hole plasmonic Schottky detectors,” *Opt. Express* **24**, 22544-22554 (2016)

[47] B. Feng, J. Zhu, B. Lu, F. Liu, L. Zhou, and Y. Chen, “Achieving Infrared Detection by All-Si Plasmonic Hot-Electron Detectors with High Detectivity,” *ACS Nano* **13**, 8433-8441 (2019)

[48] M. K. Lee, C. H. Chu, Y. H. Wang, and S. M. Sze, “1.55-μm and infrared-band photoresponsivity of a Schottky barrier porous silicon photodetector,” *Opt. Lett*. **26**, 160-162 (2001)

[49] B. Feng, J. Zhu, C. Xu, J. Wan, Z. Gan, B. Lu, and Y. Chen, “All-Si Photodetectors with a Resonant Cavity for Near-Infrared Polarimetric Detection,” *Nanoscale. Res. Lett*. **14**, 39 (2019)

[50] M. Tanzid, A. Ahmadivand, R. Zhang, B. Cerjan, A. Sobhani, S. Yazdi, P. Nordlander, and N. J. Halas, “Combining plasmonic hot carrier generation with free carrier absorption for high-performance near-infrared silicon-based photodetection,” *ACS Photonics* **5**, 3472-3477 (2018)

[51] A. A. Ahmed, M. Devarajan, and N. Afzal, “Fabrication and characterization of high performance MSM UV photodetector based on NiO film,” *Sensor Actuat A-Phys.* **262**, 78 (2017)

[52] H. Chalabi, D. Schoen, and M. L. Brongersma, “Hot-electron photodetection with a plasmonic nanostripe antenna,” *Nano Lett*. **14**, 1374 (2014)

[53] C. Zhang, K. Wu, V. Giannini, and X. Li, "Planar hot-electron photodetection with Tamm plasmons," *ACS Nano* **11**, 1719 (2017)

[54] C. Ng, J. J. Cadusch, S. Dligatch, A. Roberts, T. J. Davis, P. Mulvaney, and D. E. Gómez, "Hot carrier extraction with plasmonic broadband absorbers," *ACS Nano* **10**, 4704 (2016)

[55] T. Gong, and J. N. Munday, "Angle-independent hot carrier generation and collection using transparent conducting oxides," *Nano Lett*. **15**, 147 (2014)

[56] I. Goykhman, B. Desiatov, J. Shappir, J. B. Khurgin, and U. Levy, "Model for quantum efficiency of guided mode plasmonic enhanced silicon Schottky detectors," *arXiv preprint arXiv*, 1401.2624 (2014)

[57] F. Wang, and N. A. Melosh, "Plasmonic energy collection through hot carrier extraction," *Nano Lett.* **11**, 5426 (2011)

[58] C. Scales, and P. Berini, "Thin-film Schottky barrier photodetector models," *IEEE. J. Quantum Elect.* **46**, 633 (2010)

Chapter 4 : Narrowband and high responsivity photodetection in the near infrared using Tamm plasmons-based structures

4.1 Introduction

Hot electrons that are generated via photon absorption and plasmon decay in metals can be extracted for lots of applications, which includes photocatalysis [1,2], photovoltaics [3,4], surface imaging [5,6], sensors [7] and photodetectors [8–12]. In terms of hot electron photodetector, it enables efficient and direct below bandgap photodetection with tunable resonant wavelength through manipulating the structure dimensions instead of using novel materials (MoS_2, graphene, perovskite, etc). Hot electrons with energies higher than the M/S barrier height can cross the Schottky barrier and be injected into the semiconductor, leading to a photocurrent [13]. However, the internal photoemission efficiency for most hot electron photodetectors is too low for practical applications due to the inefficient hot electron generation rate, big thermalization loss during the transport, and large momentum mismatch at the M/S interface [14].

Surface plasmons (SPs) provide an efficient solution to improve the internal photoemission efficiency via: (1) strongly localizing the photon energy within the nanoscale region where a plenty of hot electrons can be generated [15-19], (2) facilitating the hot electron generation rate because the absorption cross section is larger than the physical cross section of the structures [20], (3) decreasing the thermalization loss of hot electrons due to the substantial generation of hot electrons close to the M/S interface [21], and (4) generating hot electrons with high energies and modifying their initial momentum distributions [22]. Up to now, a plenty of SPs-based metallic structures have been reported to improve the internal photoemission efficiency of hot electron photodetectors, which includes nanowires [23], nanorods [24], nanoholes [25], nanoparticles [26], gratings [27], etc. For example, the Si-based grating structure exhibits a high responsivity with a narrow bandwidth, and the internal

quantum efficiency (IQE) is approximately 20-fold of the plasmonic nanoantenna structure [27]. Through using an ultrathin Au film whose thickness is smaller than the mean free path (MFP) of hot electrons in Au, the disordered metamaterial nanoholes achieve a broadband and high absorption with the highest responsivity ever reported [25,28]. By placing an Au mirror beneath the Au nanodisk decorating with a TiO_2 film, the antenna/spacer/mirror structure results in a 10-fold enhancement to the responsivity compared to the identical structure without the mirror attributing to the coupling of SPs mode and Fabry–Pérot (FP) mode [29]. The plasmonic crystal based metallic nanorods exhibit a more than 30 times enhancement in the photoelectric conversion efficiency across the visible and near infrared (NIR) regime compared to the planar reference due to the high absorption, favorable hot electron distribution, and the formation of three-dimensional (3D) Schottky junction [24]. Nevertheless, most reported SPs-based hot electron photodetectors use hybrid or novel architectures with delicate design [30-36], which commonly have subwavelength patterns that ask for complicated and high-cost fabrication techniques [37].

Recently, another type of plasmons named Tamm plasmons (TPs) or optical Tamm states that is formed at the metal/distributed Bragg reflector (DBR) interface was reported [38-40]. The DBR consists of alternating multilayers with different refractive indexes, leading to periodic variation of refractive index in the structure. The optical wave is partially reflected at the boundary of each layer, and the multilayers can constitute a DBR if the optical thickness of each layer is a quarter of the central wavelength of the DBR. Through exciting TPs, the electromagnetic surface wave is strongly confined at the metal/dielectric interface, leading to high absorption of light in the metal [41]. In comparison to SPs, TPs can be excited without requiring for specific polarization of light and thus it is applicable in many fields [42], including photovoltaics [43], polariton lasers [44], sensors [45-47], optical switches [48] and photodetectors [49].

Zhang. et.al reports a TPs-based planar hot electron photodetector through introducing a DBR integrated with a collection layer in the metal/semiconductor/metal (M/S/M) configuration in 2017 [50]. The simulation results show that light can be strongly confined

at the metal/dielectric interface and the metal layer absorbs over 87% of light. The structure shows a resonant and narrowband photocurrent response with facile tunability and angle-independence. In 2019, Yu. et.al reports an Au/TiO_2 Schottky photodetector that consists of a thin Au film (20-40 nm) and a DBR made up of 9 pairs of alternating SiO_2/TiO_2 layers [51]. The structure can absorb about 93% of light by exciting TPs and the hot electron generation rate is more than 34 times of the reference without the DBR. Since the electric field increases with the penetration depth of light in the Au layer, hot electrons are substantially generated near the Au/TiO_2 interface. The calculated responsivity of the structure is more than 30 times of the conventional grating structure. Additionally, the resonant wavelength corresponding to TPs resonances of the structure exhibits a facile tunability across the visible and NIR ranges and independent of the incident angle of light. Wang. et. al reports a DBR-based metal/semiconductor/ITO (M/S/ITO) structure in 2019 [52]. For the first time, they experimentally demonstrated a wavelength-selective photodetector around the wavelength of 1550 nm. The structure exhibits a sharp and narrowband reflectance dip at the resonant wavelength of 1581 nm with the full-width at half-maximum (FWHM) of 43 nm due to the excitation of TPs. The photocurrent responsivity of the structure reaches the peak with a value of 8.26 nA/mW at the resonant wavelength of 1581 nm and the responsivity variation reaches more than 80% when the light wavelength changes within 52 nm (from 1529 to 1581 nm). However, the responsivities of the reported TPs-based structures are still too low for practical applications. The investigation on new TPs-based structures with high responsivity and facile tunability in the NIR range is urgently required. Here, we propose a DBR-film structure and a grating-on-DBR structure. The DBR-film structure generates substantial hot electrons in the Au film due to the excitation of TPs at the metal/DBR interface, and it exhibits a high photocurrent responsivity attributing to the low Ti/Si barrier height. The generation of hot electrons is further enhanced in the grating-on-DBR structure which is likely originating from the coupling of Fabry-Perot (FP) resonance and TP resonance due to the grating-on-DBR mode, leading to a much higher responsivity.

4.2 Structure diagram

Figure 4.1 shows the three-dimensional (3D) structure diagram and cross-sections for the DBR-film structure (A) and the grating-on-DBR structure (B). Structure A is made up of a DBR consisting of 5 pairs of alternating SiO_2/Si layers and an Au film. Structure B is made up of a DBR (5 pairs of alternating SiO_2/Si layers) and an Au grating. The substrates for the two structures are both quartzs. The thicknesses of SiO_2, Si and Au layers in the two structures are H_1, H_2 and H_3, respectively. The width of Au slab of the grating in structure B is D and the period of the structure is p.

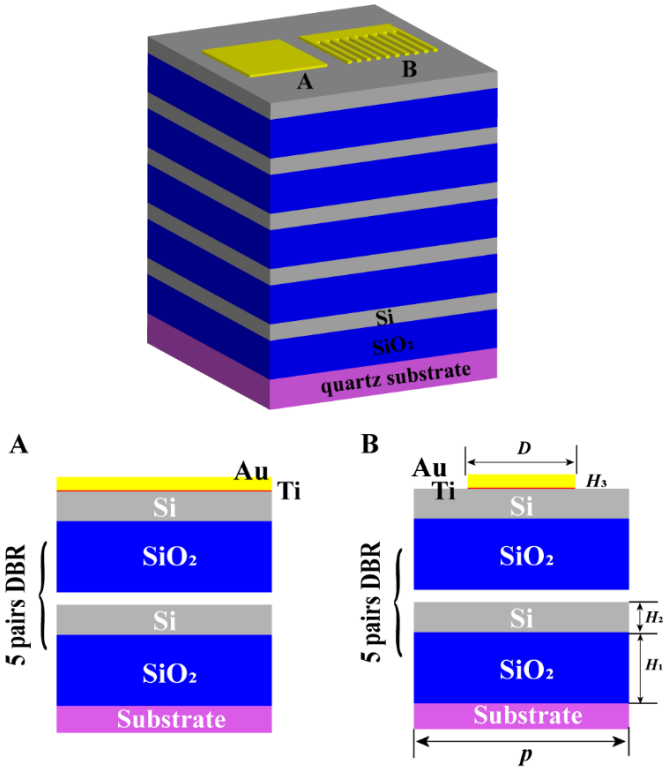

Figure 4.1 The 3D structure diagram (top) and cross-sections (bottom) for the DBR-film structure (A) and grating-on-DBR structure (B). The thicknesses of SiO_2, Si and Au layers are H_1, H_2 and H_3, respectively. The width of Au slab in structure B is D and the period of the structure is p.

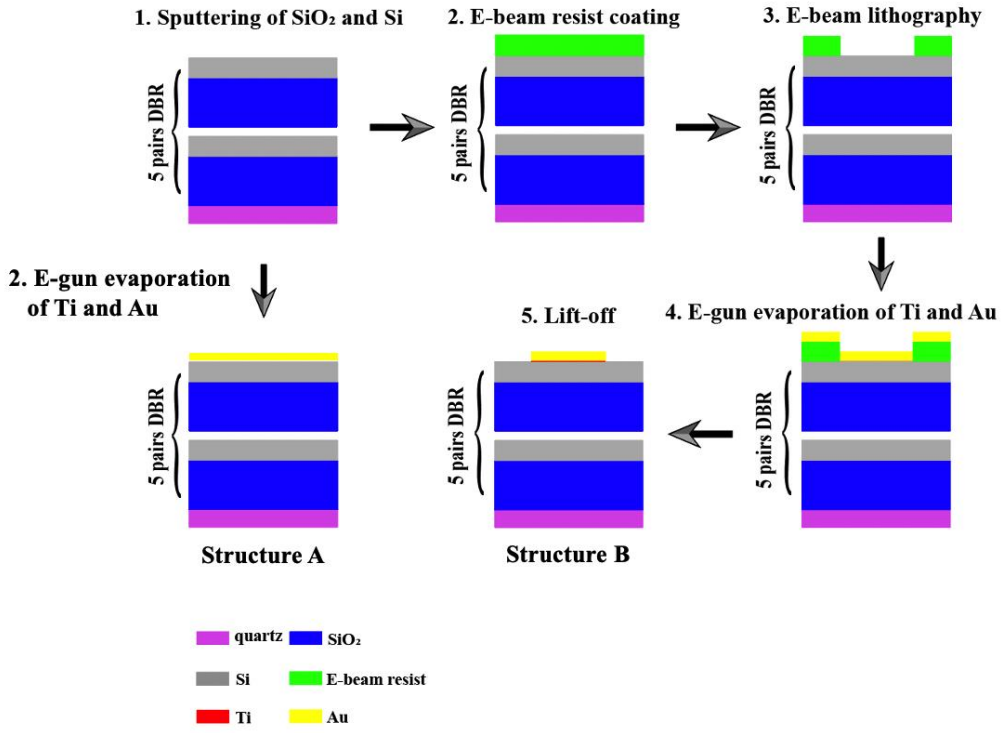

Figure 4.2 The fabrication processes for the DBR-film structure (structure A) and grating-on-DBR structure (structure B).

The recommended fabrication processes for the DBR-film structure (structure A) and grating-on-DBR structure (structure B) are shown in figure 4.2. For structure A, the fabrication process consists of two steps. First, 5 pairs of alternating SiO_2/Si layers are deposited on a quartz substrate using an RF-magnetron sputtering machine (CFS-4ES, Shibaura Engineering Works Co., Ltd, Yokohama, Japan). Subsequently, the Ti and Au film are deposited onto the DBR through electron-gun (E-gun) evaporation (Peva-400E, Advanced System Technology Co., Tokyo, Japan). The 3 nm thick Ti layer not only increases the adhesion between Si and Au but also decreases the barrier height ($\varphi(\mathrm{Ti/Au}) < \varphi(\mathrm{Si/Au})$, where $\varphi(\mathrm{Ti/Au})$ represents the barrier height between Ti and Au, and $\varphi(\mathrm{Si/Au})$ represents the barrier height between Si and Au). The fabrication process for the grating-on-DBR structure includes 5 steps, which is more complicated than the DBR-film structure. First, 5 pairs of alternating SiO_2/Si layers are deposited on a quartz substrate using the same RF-

magnetron sputtering machine. Second, the electron-beam (E-beam) resist (ZEP520A, Zeon Corporation, Tokyo, Japan) is coated onto the DBR. Following this, the E-beam resist is patterned using E-beam lithography (F7000S-VD02, Advantest, Tokyo, Japan). After that, the Ti and Au layer are deposited on the structure through E-gun evaporation. The function of the 3 nm thick Ti layer is to increase the adhesion between Si and Au and decrease the barrier height. Last, the E-beam resist and Au layer on the top are removed through lift-off in a dimethylacetamide ultrasonic bath.

4.3 Strong light absorption and field enhancement

Figure 4.3(a) shows the schematic diagrams of four different structures, which are DBR-film structure (A), grating-on-DBR structure (B), pure DBR structure (C) and traditional Si-based grating structure (D). Structure A consists of 5 pairs of DBR and an Au film, structure B consists of 5 pairs of DBR and an Au grating, structure C only consists of 5 pairs of DBR, and structure D consists of a Si substrate and an Au grating. The function of a 3 nm thick Ti layer in structure A, B and D is to increase the adhesion between Si and Au and decrease the barrier height. To generate TPs in structure A and B, the optical thickness (H_{opt}) for each alternating SiO_2/Si layer in the two structures is required to be a quarter of the central wavelength (λ_{DBR}) of the DBR, which is shown as $H_{opt} = \lambda_{DBR}/4$. Since the relationship between the physical thickness (H) and the optical thickness of the material is $H = H_{opt}/n$ (n represents the refractive index of the material), the thicknesses of SiO_2 (H_1) and Si (H_2) are calculated by $H_1 = \lambda_{DBR}/4n(SiO_2)$ and $H_2 = \lambda_{DBR}/4n(Si)$, respectively. To demonstrate the improved optical behaviors of structure A and B, the simulated reflectance and absorptance spectra of the four structures are compared, as shown in figure 4.3(b). In order to tune the resonant wavelength corresponding to TPs resonances into the C-band (1530-1565 nm), H_1 H_2 and H_3 are calculated to be 205 nm, 86 nm and 30 nm, respectively, in structure A and B. The width (D) of Au slab is 500 nm and the structure period (p) is 820 nm in structure B. The values of H_1 and H_2 in structure C are the same with that in structure A and B. The width of the Au slab and the period of structure D is 500 nm and 820 nm, respectively. The light is

normally incident with TM-polarization. Seen from the reflectance spectrum of structure A, a reflectance dip occurs in the forbidden band of the pure DBR structure (C), indicating the excitation of TPs. A reflectance dip also appears around the same resonant wavelength in structure B, exhibiting a much lower reflectance compared to that of structure A and a much narrower bandwidth than that of structure D. It is also seen that the DBR-film structure (A) and the grating-on-DBR structure (B) both have a much higher absorptance at the resonant wavelength than the traditional Si-based grating structure (D). The peak absorptance for structure B is a litter higher than that for structure A.

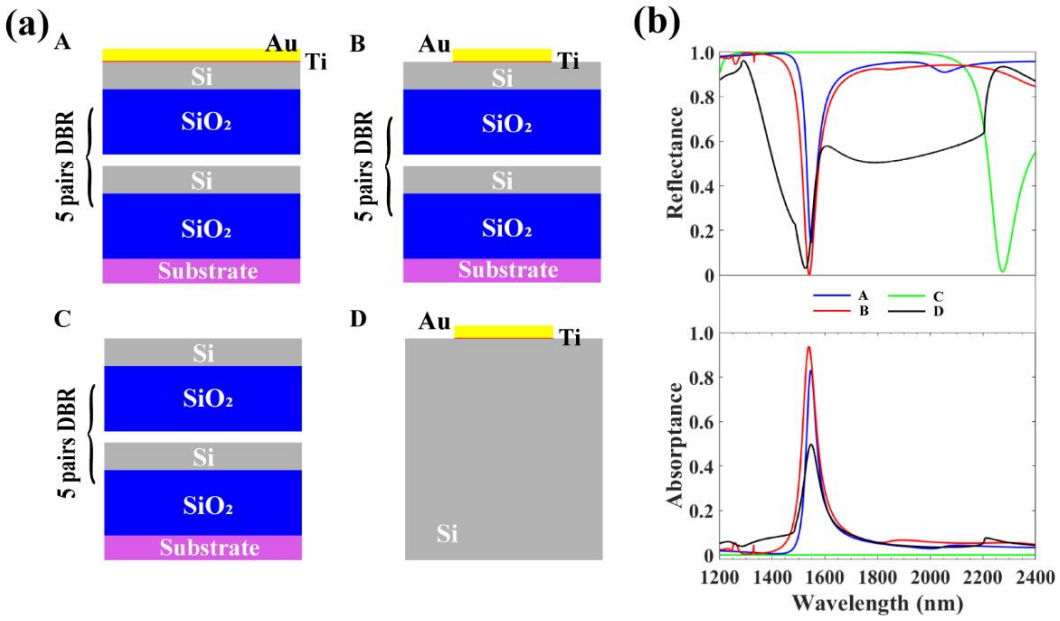

Figure 4.3 (a) Schematic diagrams of the DBR−film structure (A), the grating-on-DBR structure (B), the pure DBR structure (C) and the Si-based grating structure (D). (b) The simulated reflectance and absorptance spectra for structure A, B, C and D. The structure dimensions are H_1 = 205 nm, H_2 = 86 nm and H_3 = 30 nm in structure A, B and C. The width (D) of the Au slab is 500 nm and the period (p) is 820 nm in structure B. For structure D, the width of the Au slab and the period of the structure is 500 nm and 820 nm, respectively. The thickness of Ti layer is 3 nm in structure A, B and D. The light is normally incident with TM-polarization.

4.3.1 Optical properties for the DBR-film structure

The influence of the number (N) of the pair of DBR that is made up of alternating SiO_2/Si layers on the absorptance of the DBR−film structure is investigated, as shown in figure 4.4. The structure dimensions are H_1 = 205 nm, H_2 = 86 nm, H_3 = 30 nm, and the thickness of the Ti layer is 3 nm. The light is normally incident. It is seen that the absorptance is very low when N is 1. While the absorptance begins to increase and the spectrum exhibits spectral selectivity when N increases to 2. The peak absorptance reaches the maximum with a value of 0.83 at the resonant wavelength of 1547 nm when N increases to 5. Since the absorptance spectrum shows no changes when N is further increased, the optimized N is 5.

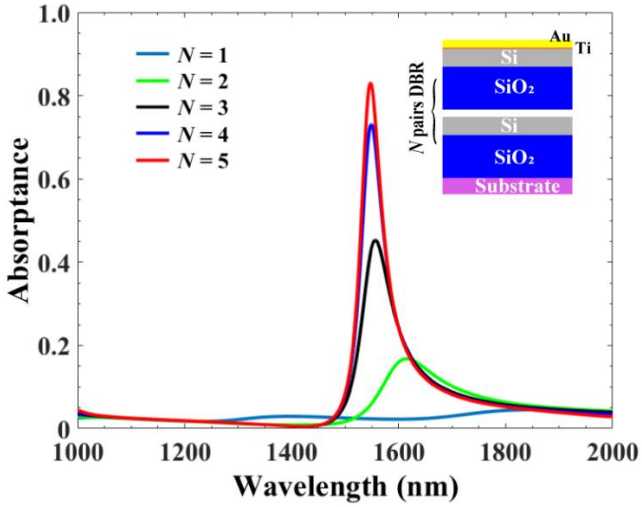

Figure 4.4 The simulated absorptance spectra for the DBR−film structure with different pairs of DBR. The structure dimensions are H_1 = 205 nm, H_2 = 86 nm and H_3 = 30 nm. The light is normally incident.

The simulated reflectance, transmittance and absorptance spectra for the DBR-film structure are shown in figure 4.5(a). The structure dimensions are H_1 = 205 nm, H_2 = 86 nm, H_3 = 30 nm, and the light is normally incident. Unless otherwise noted, N is 5 in this chapter. As shown in the figure, the absorptance spectrum reaches a peak (point P_2) with a value of 0.83 at the resonant wavelength of 1547 nm. The reflectance also drops to the minimum at

the same resonant wavelength. The transmittance always stays at a very low level (close to 0) within the wavelength range of 1000 to 2000 nm. To compare the optical behaviors of the structure at the non-resonant wavelength and resonant wavelength, the electric field ($|E|$) distributions at points P_1 and P_2 are investigated, as shown in figure 4.5(b). The electric filed is quite weak at the non-resonant wavelength (P_1). On the contrary, the electric field is much stronger at the resonant wavelength (P_2) compared to that at the non-resonant wavelength. The electric field is strongly enhanced at the fourth and last SiO_2/Si interfaces due to the generation of TPs and reaches the maximum at the last SiO_2/Si interface. Since the TPs decay with the distance away from the SiO_2/Si interface and the Ti/Si interface is close to the last SiO_2/Si interface (only 86 nm in distance), the electric field at the Ti/Si interface is still very strong.

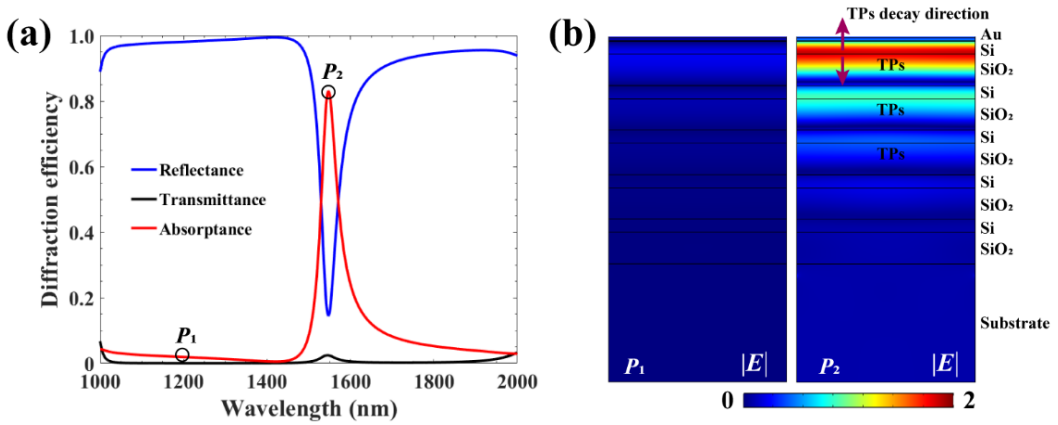

Figure 4.5 (a) The simulated reflectance, transmittance and absorptance spectra for the DBR-film structure. The structure dimensions are H_1 = 205 nm, H_2 = 86 nm, H_3 = 30 nm and N = 5. The thickness of the Ti layer is 3 nm, and the light is normally incident. (b) The simulated electric field distributions for points P_1 and P_2 in the structure.

The simulated absorptance variation with the Au layer thickness (H_3) and light wavelength in the DBR-film structure is shown in figure 4.6(a). The resonant wavelength corresponding to TPs resonances exhibits a blueshift with the increase of H_3 when H_3 is smaller than 40 nm. Once H_3 exceeds 40 nm, the TPs resonances begin to decay until

completely disappear which indicates the incident light is all reflected by the thick Au layer. The optimized thickness for the Au layer is between 10 to 30 nm. Since the thicknesses of the alternating SiO_2/Si layers are subject to the central wavelength (λ_{DBR}) of the DBR to excite TPs, it is of crucial importance to investigate the influence of λ_{DBR} on the structure absorptance. The simulated absorptance variation with λ_{DBR} and light wavelength is shown in figure 4.6(b). The resonant wavelength linearly increases with λ_{DBR}, indicating the facile tunability of TPs resonances in the NIR range. The angular dependence of the simulated absorptance of the structure is shown in figure 4.6(c). The resonant wavelength corresponding to the TPs resonances shows a blueshift with the incident angle of light. Moreover, the TPs resonances become weaker and weaker with the increase of the light angle.

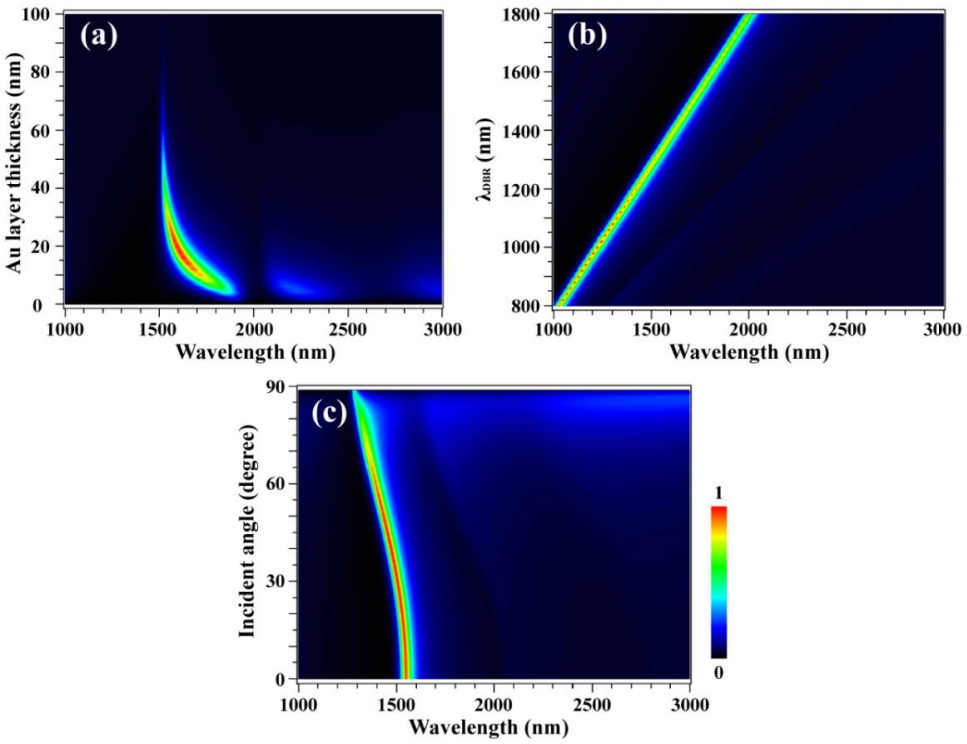

Figure 4.6 The simulated absorptance variation with different parameters of the structure. Unless otherwise noted, the structure dimensions are H_1 = 205 nm, H_2 = 86 nm, H_3 = 30 nm, N = 5, and the light is normally incident. (a) The simulated absorptance variation with the Au layer thickness (H_3) and light wavelength. (b) The simulated absorptance variation with the

central wavelength (λ_{DBR}) of the DBR and light wavelength. (c) The simulated absorptance variation with the incident angle of light and light wavelength.

4.3.2 Optical properties for the grating-on-DBR structure

The simulated reflectance, transmittance and absorptance spectra for the grating-on-DBR structure are shown in figure 4.7(a). Unless otherwise noted, the structure dimensions are D = 500 nm, p = 820 nm, H_1 = 205 nm, H_2 = 86 nm, H_3 = 30 nm, N = 5, and the light is normally incident with TM-polarization. The absorptance spectrum exhibits several peaks at points P_1, P_2 and P_3. The absorptance at point P_3 reaches as high as 0.95 at the resonant wavelength of 1547 nm. To check the optical behaviors of the structure at different resonant wavelengths, the electric field distributions at points P_1, P_2, P_3 and P_4 (non-resonant wavelength) are investigated, as shown in figure 4.7(b). At point P_1, the electric field is strongly enhanced in the first, third and last SiO_2 layers due to the FP resonance. On the contrary, the electric field is enhanced in the second and fourth SiO_2 layers for point P_2. For point P_3, the electric field is strongly enhanced at the last SiO_2/Si interface and Ti/Si interface, which is likely originating from the coupling of FP resonance and TP resonance due to the grating-on-DBR mode. The electric field at the non-resonant wavelength (point P_4) is very weak, which is used as a reference.

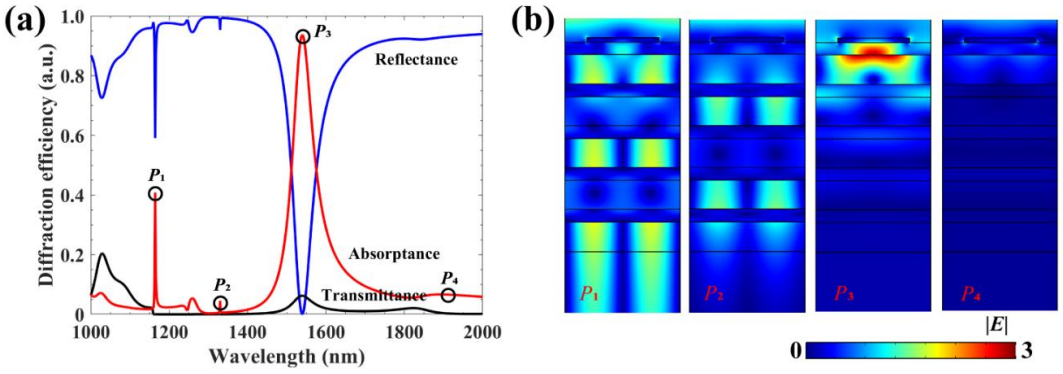

Figure 4.7 (a) The simulated reflectance, transmittance and absorptance spectra for the grating-on-DBR structure. The structure dimensions are D = 500 nm, p = 820 nm, H_1 = 205 nm, H_2 = 86 nm, H_3 = 30 nm and N = 5. The thickness of the Ti layer is 3 nm, and the light

is normally incident with TM-polarization. (b) The simulated electric field distributions for points P_1, P_2, P_3 and P_4, which are defined in (a).

The simulated reflectance variation with the width (D) of the Au slab and light wavelength is shown in figure 4.8(a). The resonant wavelength corresponding to point P_3, as defined in figure 4.7(a), shows a small blueshift when D increases from 200 to 700 nm. The influence of the thickness (H_3) of the Au slab on the reflectance is also investigated, as shown in figure 4.8(b). The resonant wavelength shows a blueshift and the resonance bandwidth becomes narrower and narrower when H_3 increases from 0 to 30 nm. The resonant wavelength and bandwidth almost keep stable when H_3 exceeds 50 nm. The reflectance variation with the period of the structure and light wavelength is shown in figure 4.8(c). The resonant wavelength corresponding to point P_3 exhibits a redshift with the increase of the period. The influence of the central wavelength (λ_{DBR}) of the DBR on the reflectance is given in figure 4.8(d). The resonant wavelength corresponding to point P_3 exhibits a linearly redshift with λ_{DBR}, demonstrating the presence of TPs resonances.

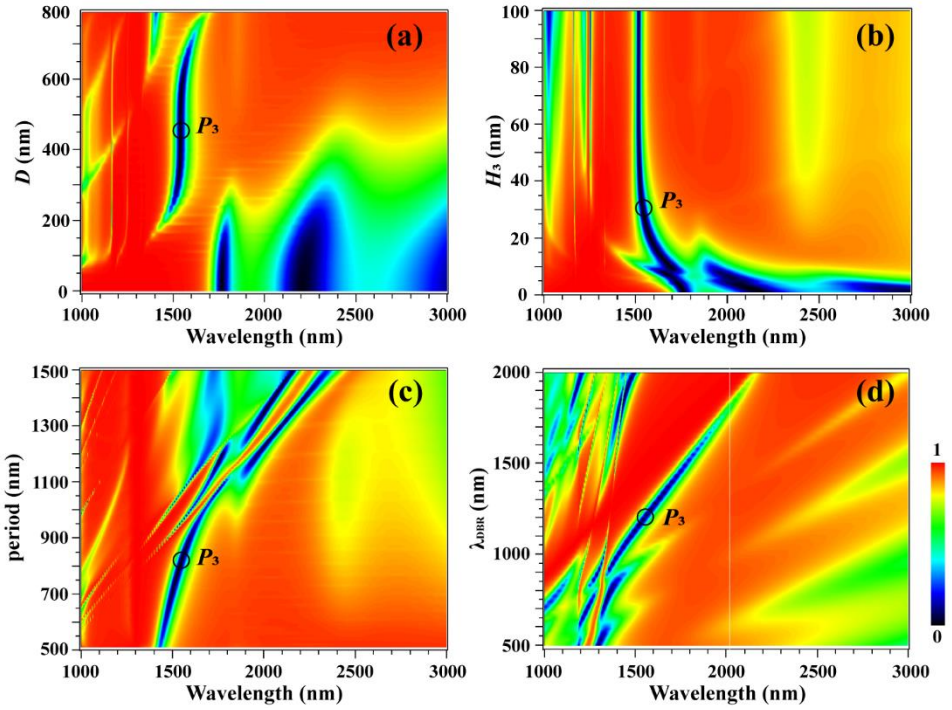

Figure 4.8 The simulated reflectance variation with different structure dimensions and light wavelength of the grating-on-DBR structure. Unless otherwise noted, the structure dimensions are D = 500 nm, p = 820 nm, H_1 = 205 nm, H_2 = 86 nm, H_3 = 30 nm and N = 5. The thickness of the Ti layer is 3 nm, and the light is normally incident with TM-polarization. (a) The simulated reflectance variation with the width (D) of the Au slab and light wavelength. (b) The simulated reflectance variation with the thickness (H_3) of the Au slab and light wavelength. (c) The simulated reflectance variation with the period (p) of the structure and light wavelength. (d) The simulated reflectance variation with the central wavelength (λ_{DBR}) of DBR and light wavelength.

4.4 Theoretical calculation of photocurrent responsivity

4.4.1 Generation, transport and collection of hot electrons

The formation of photocurrent in the DBR-film structure and grating-on-DBR structure is mainly attributed to the generation, transport and collection of hot electrons in the structures. The detailed calculation of the photocurrent responsivity in the two structures is clarified in the following.

(1) Generation of hot electrons

The absorbed power density ($abs(\vec{r},\omega)$) of the structure is first obtained linking to the local Ohmic loss in the Au layer

$$abs(\vec{r},\omega) = \frac{\varepsilon_i \omega \left|\vec{E}(\vec{r},\omega)\right|^2}{2}, \quad (1)$$

where $\vec{r}$ represents the position, ω represents the angular frequency of light, ε_i represents the imaginary part of the permittivity of Au, and $\vec{E}(\vec{r},\omega)$ represents the electrical field. The hot electron generation rate $G(\vec{r},\omega)$ can then be expressed as

$$G(\vec{r},\omega)=\frac{abs(\vec{r},\omega)}{\hbar\omega}=\frac{\varepsilon_i\left|\vec{E}(\vec{r},\omega)\right|^2}{2\hbar}, \tag{2}$$

where $\hbar$ represents the reduced Planck constant.

(2) Transport and collection of hot electrons

The generated hot electrons will transport to the metal/semiconductor (M/S) interface and be injected into the semiconductor after crossing the Schottky barrier with a specific probability (P). The kinetic energy of a hot electron that is generated in the Au layer E_{Au} is expressed as

$$E_{\mathrm{Au}}=E_F+E, \tag{3}$$

where E_{F} represents the Fermi level of the Au layer and E $(0<E<\hbar\omega)$ represents hot electron energy above the Fermi level. The hot electron momentum in the Au layer k_{Au} can be expressed as

$$k_{\mathrm{Au}}=\frac{\sqrt{2m_e^*E_{\mathrm{Au}}}}{\hbar}=\frac{\sqrt{2m_e^*(E_F+E)}}{\hbar}, \tag{4}$$

where m_e^* represents the effective mass of an electron. The hot electron kinetic energy after crossing the M/S barrier into the Si (E_{Si}) is expressed as

$$E_{\mathrm{Si}}=E-\varphi_{\mathrm{b}}, \tag{5}$$

where φ_{b} represents the barrier height. The hot electron momentum in the Si (k_{Si}) is expressed as

$$k_{\mathrm{Si}}=\frac{\sqrt{2m_e^*E_{\mathrm{Si}}}}{\hbar}=\frac{\sqrt{2m_e^*(E-\varphi_{\mathrm{b}})}}{\hbar}. \tag{6}$$

As discussed in chapter 3, the hot electron that successfully reaches the M/S interface can cross the Schottky barrier only if its momentum component in the x direction $(k_{\mathrm{Au}})_x$ is larger than the threshold k_{es}, which defines an escape cone. The probability P_{esc} for hot electrons being in the escape cone is shown as

$$P_{\mathrm{esc}} = \frac{d\Omega}{4\pi} = \frac{2\pi \sin\theta d\theta}{4\pi} = \frac{k_y}{2k_{\mathrm{Au}}\sqrt{k_{\mathrm{Au}}^2 - k_y^2}}, \tag{7}$$

where k_y represents the momentum component in the y direction. The probability P_{ref} for hot electrons crossing the Schottky barrier without reflection is expressed as

$$P_{\mathrm{ref}} = \frac{4(k_{\mathrm{Au}})_x (k_{\mathrm{Si}})_x}{((k_{\mathrm{Au}})_x + (k_{\mathrm{Si}})_x)^2} = \frac{4\sqrt{\left(k_{\mathrm{Au}}^2 - k_y^2\right)\left(k_{\mathrm{Si}}^2 - k_y^2\right)}}{\left(\sqrt{k_{\mathrm{Au}}^2 - k_y^2} + \sqrt{k_{\mathrm{Si}}^2 - k_y^2}\right)^2}, \tag{8}$$

where $(k_{\mathrm{Si}})_x$ represents the x-component of k_{Si}. The transmission probability P for hot electrons crossing the M/S Schottky barrier is expressed as

$$P = \int_0^{K_{\mathrm{Si}}(E)} P_{\mathrm{esc}} P_{\mathrm{ref}} dk_y = \int_0^{K_{\mathrm{Si}}(E)} \frac{2\sqrt{k_{\mathrm{Si}}^2 - k_y^2}}{\left(\sqrt{k_{\mathrm{Au}}^2 - k_y^2} + \sqrt{k_{\mathrm{Si}}^2 - k_y^2}\right)^2} \frac{k_y}{k_{\mathrm{Au}}} dk_y, \tag{9}$$

where $K_{\mathrm{Si}}(E)$ represents the maximum of k_{Si} and it is calculated by

$$K_{\mathrm{Si}}(E) = (k_{\mathrm{Si}})_{max} = \frac{\sqrt{2m_e^*(E_{\mathrm{Si}})_{max}}}{\hbar} = \frac{\sqrt{2m_e^*(\hbar\omega - \varphi_{\mathrm{b}})}}{\hbar}. \tag{10}$$

The internal quantum efficiency (IQE, defined as η) can be shown as

$$\eta = \frac{1}{E_{\mathrm{ph}}} \int_{\varphi_{\mathrm{b}}}^{E_{\mathrm{ph}}} P dE\,, \tag{11}$$

where E_{ph} represents the photon energy. The photocurrent responsivity R and photocurrent i_{ph} can then be expressed as

$$R = \frac{eA\eta}{h\omega}, \tag{12}$$

$$i_{\mathrm{ph}} = RP_{\mathrm{inc}}, \tag{13}$$

where A represents the optical absorptance and P_{inc} represents the incident power of light illuminated on the structure.

4.4.2 Narrowband and high responsivity photodetection in the near infrared

The calculated normalized hot electron generation rates G for the DBR-film structure and the grating-on-DBR structure are shown in figure 4.9(a) and (b), respectively. The structure dimensions are D = 500 nm, H_1 = 205 nm, H_2 = 86 nm, H_3 = 30 nm and N = 5. The thickness of the Ti layer is 3 nm, and the light is normally incident with TM-polarization. It is seen that the generation rate of hot electrons decreases from the M/S interface to the other side of the Au film in the DBR-film structure. Hot electrons are substantially generated in the middle part of the Au slab in the grating-on-DBR structure, which attributes to the strong field enhancement in the middle of the Au slab as shown in figure 4.7(b).

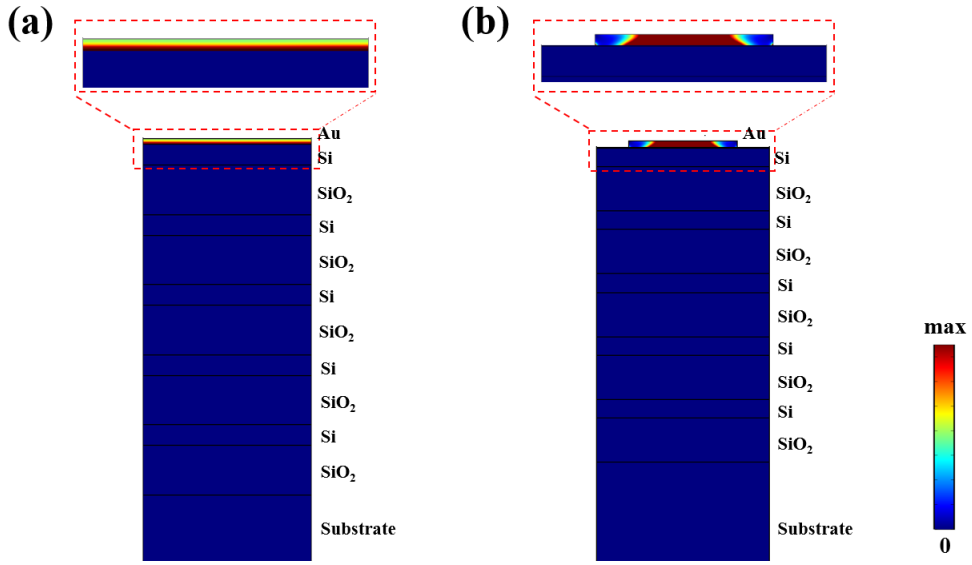

Figure 4.9 The normalized hot electron generation rates G for the (a) DBR-film structure, and (b) the grating-on-DBR structure. The structure dimensions are D = 500 nm, H_1 = 205 nm, H_2 = 86 nm, H_3 = 30 nm and N = 5. The thickness of the Ti layer is 3 nm, and the light is normally incident with TM-polarization.

The calculated photocurrent responsivity of the DBR-film structure for different Au film thicknesses (H_3) is shown in figure 4.10(a). The inset shows the electrical connection, where the photocurrent is measured between the Au film and the top Si layer. The responsivity spectrum exhibits a narrowband and resonant photocurrent response. With the increase of H_3 (from 20 to 50 nm), the resonant wavelength shows a blueshift and the peak responsivity and the bandwidth both decrease. Figure 4.10(b) shows the calculated responsivity for different incident angles (θ) of light. When θ increases from 0° to 45°, the responsivity spectrum exhibits a narrowband and tunable resonant wavelength with the variation of θ.

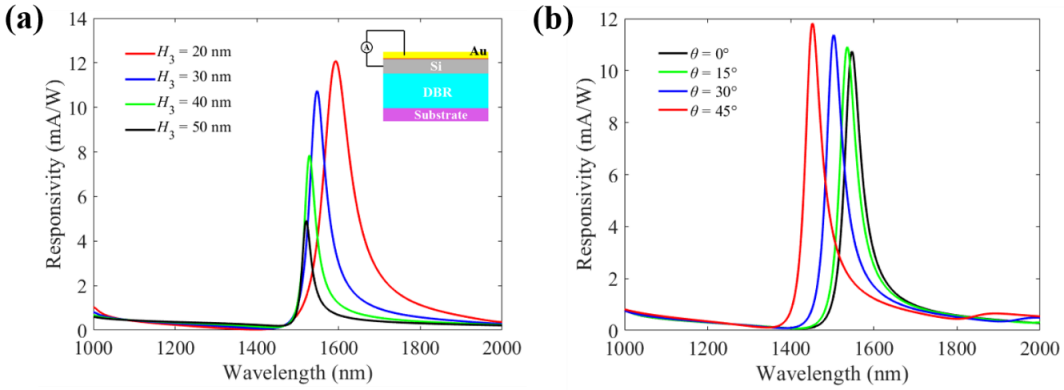

Figure 4.10 The calculated photocurrent responsivity of the DBR-film structure for (a) different Au film thicknesses (H_3), and (b) different incident angles (θ) of light. The inset in (a) shows the electrical connection for measuring the photocurrent. Unless otherwise noted, the structure dimensions are H_1 = 205 nm, H_2 = 86 nm, H_3 = 30 nm and N = 5. The thickness of the Ti layer is 3 nm, and the light is normally incident.

The calculated photocurrent responsivity of the grating-on-DBR structure for different thicknesses (H_3) of the Au slab is shown in figure 4.11(a). The inset shows the electrical connection, where the photocurrent is measured between the Au slab and the top Si layer. When H_3 increases from 20 nm to 50 nm, the responsivity spectrum shows a blueshift and the bandwidth becomes narrower and narrower. The tunability of the responsivity spectrum can also be controlled through changing the width (D) of the Au slab, as shown in figure 4.11(b). The responsivity spectrum exhibits a very small redshift when D increases from 400

to 600 nm, but it shows a large redshift when D increases to 700 nm and the peak responsivity decreases. The responsivity spectrum also shows a tunable resonant wavelength when the structure period (p) increases from 800 to 860 nm, as shown in figure 4.11(c). The appearance of the ultra-narrow and small peak around the wavelength of 1415 nm is due to the FP resonance which has been discussed in section 4.3.2. The calculated responsivity is strongly dependent on the incident angle of light (θ), as shown in figure 4.11(d). The responsivity spectrum shows a blueshift and splits when θ increases from 0° to 30°.

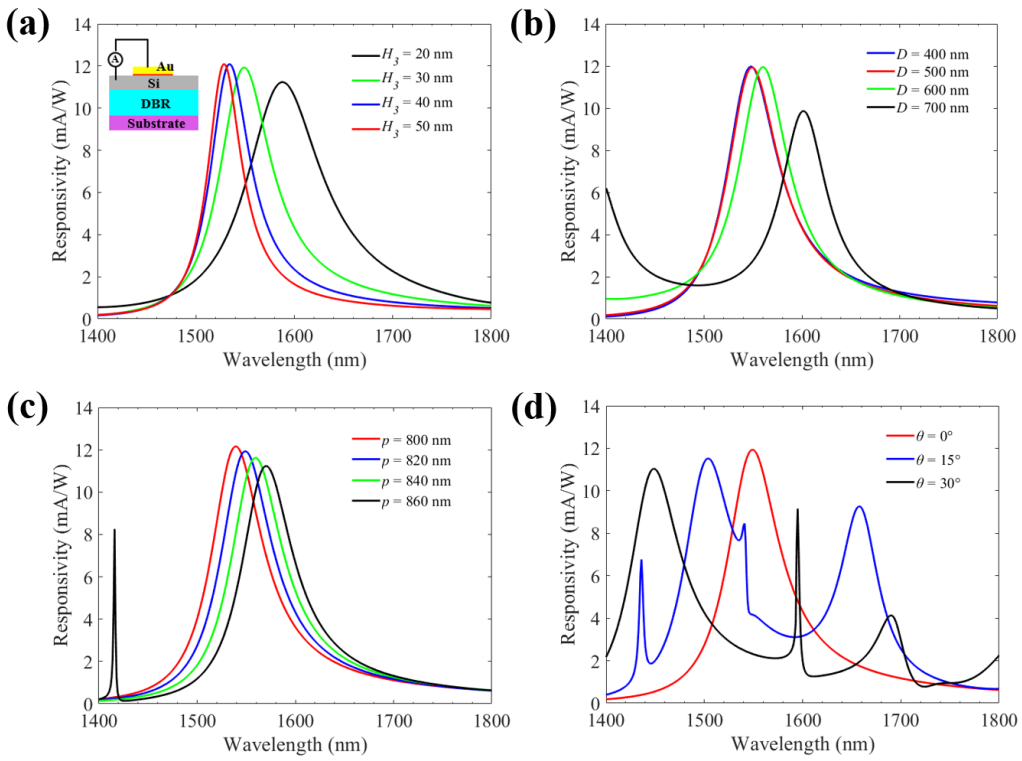

Figure 4.11 The calculated photocurrent responsivity of the grating-on-DBR structure for (a) different thicknesses (H_3) of the Au slab, (b) different widths (D) of the Au slab, (c) different periods (p) of the structure, and (d) different incident angles (θ) of light. The inset in (a) shows the electrical connection for measuring the photocurrent. Unless otherwise noted, the structure dimensions are D = 500 nm, p = 820 nm, H_1 = 205 nm, H_2 = 86 nm and H_3 = 30 nm. The thickness of the Ti layer is 3 nm, and the light is normally incident with TM-polarization.

The comparison of photocurrent responsivity among the reported TPs-based hot electron photodetectors is shown in Table 1. Seen from the comparison, the responsivities of our proposed DBR-film structure (10737 nA/mW) and grating-on-DBR structure (11933 nA/mW) are both in the highest level (> 10000 nA/mW), showing a competitive performance with previously reported TPs-based hot electron photodetectors. Moreover, the responsivities of our proposed two structures are more than 17 times of the Si-based grating structure (600 nA/mW) [56].

Table 1: Comparison of photocurrent responsivity among TPs-based hot electron photodetectors

Structure [reference]	Resonant wavelength (nm)	Bias (V)	Responsivity (nA/mW)
DBR-based MSM structure [50]	813	0	13.7 (cal.)
SiO_2/TiO_2-Au film structure [51]	892	0	750 (cal.)
M–S–ITO–DBR structure [52]	1581	0	8.26 (exp.)
microcavity integrated DBR M/S/TCO structure [53]	850	0	239 (cal.)
DBR-M-S structure [54]	1100	0	16000 (cal.)
DBR-film structure [this work]	**1547**	**0**	**10737 (cal.)**
grating-on-DBR structure [this work]	**1549**	**0**	**11933 (cal.)**

Note: cal. represents calculation result, and exp. represents experiment result.

4.5 Discussion

In this chapter, we propose a DBR-film structure and a grating-on-DBR structure. The DBR-film structure achieves a high absorptance of 0.83 at the resonant wavelength of 1547 nm. The generation of hot electrons in the Au film is enhanced by the excitation of TPs at the

metal/DBR interface, which facilitates the photocurrent responsivity. The grating-on-DBR structure further increases the absorptance at the resonant wavelength, and shows a larger modulation (0.95) compared with the DBR-film structure (0.83) and the traditional Si-based grating structure (0.5). The electric field distribution in the structure is strongly enhanced at the Ti/Si interface due to the grating-on-DBR mode. Therefore, the generation of hot electrons is significantly facilitated and a large photocurrent responsivity is obtained. The calculated responsivities of the proposed two structures both exhibit a narrowband and high responsivity photodetection in the near infrared. The calculated responsivities of the DBR-film structure (10737 nA/mW) and the grating-on-DBR structure (11933 nA/mW) are both among the highest level (> 10000 nA/mW), showing a competitive performance with previously reported TPs-based hot electron photodetectors.

References

(1) J. Li, S. K. Cushing, P. Zheng, F. Meng, D. Chu, and N. Wu, "Plasmon-Induced Photonic and Energy-Transfer Enhancement of Solar Water Splitting by a Hematite Nanorod Array," *Nat. Commun.* **4**, 2651 (2013)

(2) S. Mukherjee, F. Libisch, N. Large, O. Neumann, L. V. Brown, J. Cheng, J. B. Lassiter, E. A. Carter, P. Nordlander, and N. J. Halas, "Hot Electrons do the Impossible: Plasmon-Induced Dissociation of H_2 on Au," *Nano Lett.* **13**, 240-247 (2013)

(3) C. Clavero, "Plasmon-Induced Hot-Electron Generation at Nanoparticle/Metal-Oxide Interfaces for Photovoltaic and Photocatalytic Devices," *Nat. Photonics,* **8**, 95-103 (2014)

(4) J. G. Smith, J. A. Faucheaux, P. K. Jain, "Plasmon Resonances for Solar Energy Harvesting: A Mechanistic Outlook," *Nano Today* **10**, 67-80 (2015)

(5) P. J. Schuck, "Nanoimaging: Hot Electrons Go through the Barrier," *Nat. Nanotechnol.* **8**, 799-800 (2013)

(6) A. Giugni, B. Torre, A. Toma, M. Francardi, M. Malerba, A. Alabastri, R. P. Zaccaria, M. I. Stockman, and E. Di Fabrizio, "Hot Electron Nanoscopy Using Adiabatic Compression of Surface Plasmons," *Nat. Nanotechnol.* **8**, 845-852 (2013)

(7) L. Wen, L. Liang, X. Yang, Z. Liu, B. Li and Q. Chen, "Multiband and Ultrahigh Figure-of-Merit Nanoplasmonic Sensing with Direct Electrical Readout in Au-Si Nanojunctions," *ACS Nano* **13**, 6963–6972 (2019)

(8) M. W. Knight, H. Sobhani, P. Nordlander, and N. J. Halas, "Photodetection with Active Optical Antennas," *Science* **332**, 702-704 (2011)

(9) S. Mubeen, G. Hernandez-Sosa, D. Moses, J. Lee, and M. Moskovits, "Plasmonic Photosensitization of a Wide Band Gap Semiconductor: Converting Plasmons to Charge Carriers," *Nano Lett.* **11**, 5548-5552 (2011)

(10) Y. K. Lee, C. H. Jung, J. Park, H. Seo, G. A. Somorjai, and J. Y. Park, "Surface Plasmon-Driven Hot Electron Flow Probed with Metal Semiconductor Nanodiodes," *Nano Lett.* **11**, 4251-4255 (2011)

(11) F. Wang, and N. A. Melosh, "Power-Independent Wavelength Determination by Hot Carrier Collection in Metal-Insulator-Metal Devices," *Nat. Commun.* **4**, 1711 (2013)

(12) M. Moskovits, Hot Electrons Cross Boundaries. "Hot electrons cross boundaries," *Science* **332**, 676-677 (2011)

(13) B. Y. Zheng, H. Zhao, A. Manjavacas, M. McClain, P. Nordlander and N. J. Halas, "Distinguishing between plasmon-induced and photoexcited carriers in a device geometry," *Nat. Commun.* **6**, 7797 (2015)

(14) C. Zhang, G. Cao, S. Wu, W. Shao, V. Giannini, S. A. Maier and X. Li, "Thermodynamic loss mechanisms and strategies for efficient hot-electron photoconversion," *Nano Energy* **55**, 164–172 (2019)

(15) W. Li, and J. Valentine, "Metamaterial Perfect Absorber Based Hot Electron Photodetection," *Nano Lett.* **14**, 3510-3514 (2014)

(16) Moskovits, M. The Case for Plasmon-Derived Hot Carrier Devices. "The case for plasmon-derived hot carrier devices," *Nat. Nanotechnol.* **10**, 6-8 (2015)

(17) A. O. Govorov, H. Zhang, H. V. Demir, and Y. K. Gun'ko, "Photogeneration of Hot Plasmonic Electrons with Metal Nanocrystals: Quantum Description and Potential Applications," *Nano Today* **9**, 85-101 (2014)

(18) M. L. Brongersma, N. J. Halas, and P. Nordlander, "Plasmon Induced Hot Carrier Science and Technology," *Nat. Nanotechnol.* **10**, 25-34 (2015)

(19) R. Sundararaman, P. Narang, A. S. Jermyn, W. A. III. Goddard, and H. A. Atwater, "Theoretical Predictions for Hot-Carrier Generation from Surface Plasmon Decay," *Nat. Commun.* **5**, 5788 (2014)

[20] V. Giannini, A. I. Fernández-Domínguez, S. C. Heck and S. A. Maier, "Plasmonic nanoantennas: fundamentals and their use in controlling the radiative properties of nanoemitters," *Chem. Rev.* **111**, 3888–3912 (2011)

[21] A. Sobhani, M. W. Knight, Y. Wang, B. Zheng, N. S. King, L. V. Brown, Z. Fang, P. Nordlander and N. J. Halas, "Narrowband photodetection in the near-infrared with a plasmon-induced hot electron device," *Nat. Commun.* **4**, 1643 (2013)

[22] W. Li and J. G. Valentine, “Harvesting the loss: surface plasmon-based hot electron photodetection,” *Nanophotonics* **6**, 177–191 (2017)

[23] M. W. Knight, Y. Wang, A. S. Urban, A. Sobhani, B. Y. Zheng, P. Nordlander and N. J. Halas, “Embedding plasmonic nanostructure diodes enhances hot electron emission,” *Nano Lett.* **13**, 1687–1692 (2013)

[24] C. Zhang, Q. Qian, L. Qin, X. Zhu, C. Wang and X. Li, “Broadband light harvesting for highly efficient hot-electron application based on conformal metallic nanorod arrays,” *ACS Photonics* **5**, 5079–5085 (2018)

[25] L. Wen, Y. Chen, L. Liang and Q. Chen, “Hot electron harvesting via photoelectric ejection and photothermal heat relaxation in hotspots-enriched plasmonic/photonic disordered nanocomposites,” *ACS Photonics* **5**, 581–591 (2017)

[26] F. Tan, N. Wang, D. Y. Lei, W. Yu and X. Zhang, “Plasmonic Black Absorbers for Enhanced Photocurrent of Visible-Light Photocatalysis,” *Adv. Opt. Mater.* **5**, 1600399 (2017)

[27] A. Sobhani, M. W. Knight, Y. Wang, B. Zheng, N. S. King, L. V. Brown, Z. Fang, P. Nordlander and N. J. Halas, “Narrowband photodetection in the near-infrared with a plasmon-induced hot electron device,” *Nat. Commun.* **4**, 1643 (2013)

[28] W. Li and J. Valentine, “Metamaterial perfect absorber based hot electron photodetection,” *Nano Lett.* **14**, 3510–3514 (2014)

[29] Y. Fang, Y. Jiao, K. Xiong, R. Ogier, Z. J. Yang, S. Gao, A. B. Dahlin and M. Käll, “Plasmon Enhanced Internal Photoemission in Antenna-Spacer-Mirror Based Au/TiO2 Nanostructures,” *Nano Lett.* **15**, 4059–4065 (2015)

(30) K. Ueno, and H. Misawa, “Plasmon-Enhanced Photocurrent Generation and Water Oxidation from Visible to Near-Infrared Wavelengths,” *NPG Asia Mater.* **5**, e61 (2013)

(31) M. W. Knight, Y. Wang, A. S. Urban, A. Sobhani, B. Y. Zheng, P. Nordlander, N. J. Halas, “Embedding Plasmonic Nanostructure Diodes Enhances Hot Electron Emission,” *Nano Lett.* **13**, 1687-1692 (2013)

(32) K. T. Lin, H. L. Chen, Y.S. Lai, and C. C. Yu, “Silicon-Based Broadband Antenna for High Responsivity and Polarization-Insensitive Photodetection at Telecommunication Wavelengths,” *Nat. Commun.* **5**, 3288 (2014)

(33) I. Goykhman, B. Desiatov, J. Khurgin, J. Shappir, U. Levy, “Locally Oxidized Silicon Surface-Plasmon Schottky Detector for Telecom Regime,” *Nano Lett.* **11**, 2219-2224 (2011)

(34) K. Wu, Y. Zhan, C. Zhang, S. Wu, and X. Li, “Strong and Highly Asymmetrical Optical Absorption in Conformal Metal-Semiconductor-Metal Grating System for Plasmonic Hot-Electron Photodetection Application. *Sci. Rep*. **5**, 14304 (2015)

(35) Y. Fang, Y. Jiao, K. Xiong, R. Ogier, Z. J. Yang, S. Gao, A. B. Dahlin, and M. Kall, “Plasmon Enhanced Internal Photoemission in ̈Antenna-Spacer-Mirror Based Au/TiO_2 Nanostructures,” *Nano Lett.* **15**, 4059-4065 (2015)

(36) F. Wang, and N. A. Melosh, “Plasmonic Energy Collection through Hot Carrier Extraction,” *Nano Lett.* **11**, 5426-5430 (2011)

(37) K. T. Lin, H. L. Chen, Y. S. Lai, and C. C. Yu, “Silicon-Based Broadband Antenna for High Responsivity and Polarization-Insensitive Photodetection at Telecommunication Wavelengths,” *Nat. Commun.* **5**, 3288 (2014)

(38) L. Ferrier, H. S. Nguyen, C. Jamois, L. Berguiga, C. Symonds, J. Bellessa, and T. Benyattou, “Tamm plasmon photonic crystals: From bandgap engineering to defect cavity,” *APL Photonics* **4**, 106101 (2019)

(39) M. E. Sasin, R. P. Seisyan, M. A. Kalitteevski, S. Brand, R. A. Abram, J. M. Chamberlain, A. Yu. Egorov, A. P. Vasil’ev, V. S. Mikhrin, and A. V. Kavokin, “Tamm Plasmon Polaritons: Slow and Spatially Compact Light,” *Appl. Phys. Lett.* **92**, 251112 (2008)

(40) C. Grossmann, C. Coulson, G. Christmann, I. Farrer, H. E. Beere, D. A. Ritchie, and J. J. Baumberg, “Tuneable Polaritonics at Room Temperature with Strongly Coupled Tamm Plasmon Polaritons in Metal/Air-Gap Microcavities,” *Appl. Phys. Lett.* **98**, 231105 (2011)

(41) Y. Chen, D. Zhang, D. Qiu, L. Zhu, S. Yu, P. Yao, P. Wang, H. Ming, R. Badugu, and J. R. Lakowicz, "Back Focal Plane Imaging of Tamm Plasmons and Their Coupled Emission," *Laser Photon. Rev.* **8**, 933-940 (2014)

(42) X. F. Zhang, J. F. Song, X. B. Li, J. Feng, and H. B. Sun, "Optical Tamm States Enhanced Broad-Band Absorption of Organic Solar Cells," *Appl. Phys. Lett.* **101**, 243901 (2012)

(43) X. L. Zhang, J. F. Song, J. Feng, and H. B. Sun, "Spectral Engineering by Flexible Tunings of Optical Tamm States and Fabry-Perot Cavity Resonance," *Opt. Lett.* **38**, 4382-4385 (2013)

(44) A. Kavokin, I. Shelykh, and G. Malpuech, "Optical Tamm States for the Fabrication of Polariton Lasers," *Appl. Phys. Lett.* **87**, 261105 (2005)

(45) W. L. Zhang, F. Wang, Y. J. Rao, and Y. Jiang, "Novel Sensing Concept Based on Optical Tamm Plasmon," *Opt. Express* **22**, 14524-14529 (2014)

(46) R. Das, T. Srivastava, and R. Jha, "Tamm-Plasmon and Surface Plasmon Hybrid-Mode Based Refractometry in Photonic Bandgap Structures," *Opt. Lett.* **39**, 896-899 (2014)

(47) B. Auguie, M. C. Fuertes, P. C. Angelome´, N. L. Abdala, G. J. Soler´ Illia, and A. Fainstein, "Tamm Plasmon Resonance in Mesoporous Multilayers: toward a Sensing Application," *ACS Photonics* **1**, 775-780 (2014)

(48) T. C. H. Liew, A. V. Kavokin, and I. A. Shelykh, "Optical Circuits Based on Polariton Neurons in Semiconductor Microcavities," *Phys. Rev. Lett.* **101**, 016402 (2008)

(49) S. Azzini, G. Lheureux, C. Symonds, J. M. Benoit, P. Senellart, A. Lemaitre, A. Greffet, C. Blanchard, C. Sauvan, J. Bellessa, "Generation and Spatial Control of Hybrid Tamm Plasmon/Surface Plasmon Modes," *ACS Photonics*, **3**, 1776-1781 (2016)

(50) C. Zhang, K. Wu, V. Giannini, and X. Li, "Planar hot-electron photodetection with Tamm plasmons," *ACS Nano* **11**, 1719-1727 (2017)

(51) T. Yu, C. Zhang, H. Liu, J. Liu, K. Li, L. Qin, and X. Li, "Planar, narrowband, and tunable photodetection in the near-infrared with Au/TiO_2 nanodiodes based on Tamm plasmons," *Nanoscale* **11**, 23182-23187 (2019)

(52) Z. Wang, J. K. Clark, Y. L. Ho, and J. J. Delaunay, “Hot-electron photodetector with wavelength selectivity in near-infrared via Tamm plasmon,” *Nanoscale* **11**, 17407-17414 (2019)

(53) C. Zhang, K. Wu, Y. Zhan, V. Giannini, and X. Li, “Planar microcavity-integrated hot-electron photodetector,” *Nanoscale* **8**, 10323-10329 (2016)

(54) R. Li, C. Zhang, and X. Li, “Schottky hot-electron photodetector by cavity-enhanced optical Tamm resonance,” *Appl. Phys. Lett.* **110**, 013902 (2017)

(55) Y. L. Ho, Y. H. Tai, J. K. Clark, Z. Wang, P. K. Wei, and J. J. Delaunay, “Plasmonic Hot-Carriers in Channel-Coupled Nanogap Structure for Metal–Semiconductor Barrier Modulation and Spectral-Selective Plasmonic Monitoring,” *ACS Photonics* **5**, 2617-2623 (2018)

(56) A. Sobhani, M. W. Knight, Y. Wang, B. Zheng, N. S. King, L. V. Brown, Z Fang, P. Nordlander and N. J. Halas, “Narrowband photodetection in the near-infrared with a plasmon-induced hot electron device,” *Nat. Commun.* **4**, 1-6 (2013).

Chapter 5 : Conclusions and future work

Hot electron photodetectors are commonly made up of M/S architecture, M/I/M architecture and the derived architecture (M/S/M, M/I/TCO, M/S/TCO, etc.). The formation of photocurrent consists of a 3-step internal photoemission process (① photoexcitation, ② transport and ③ emission) in M/S architectures, or a 5-step photoemission process of hot electrons across the M/I/M and the derived architectures (eg, ① generation in one metal contact, ② reach the first M/I interface, ③ cross the first M/I barrier, ④ transport through the insulator, ⑤ cross the second M/I barrier and be collected by the opposing metal contact).

For all architectures, hot electrons can be generated in the metallic structure via either photoexcitation or the decay of plasmons. After the generation, only the hot electrons with the momentum inside the escape cone and higher energy than the barrier height can cross the barrier and be collected. The internal photoemission of hot electrons over a bulk Schottky junction (M/S, M/I, etc.) is usually a very inefficient process due to the poor light absorption, broad energy distribution of hot electrons and isotropic hot electron momentum distribution. To increase the photoelectric conversion efficiency and the photocurrent response of hot electron photodetectors, plasmonic structures that are capable of inducing surface plasmon resonances (SPRs) and further increasing the light absorption are deliberately designed. Both the broadband and narrowband high-absorption in the specific wavelength range (visible, near infrared, middle infrared) can be achieved through using different plasmonic structures and materials. For example, to achieve the spectrally selective and high-responsivity hot electron photodetection in the near infrared, we deliberately design a Si channel-separated parallel grating structure as shown in chapter 2 and a Si channel-separated interdigitated grating structure as shown in chapter 3 in this thesis. Due to excitation of SPP mode, these two structures strongly trap and confine light at the M/S interface and corners of the Au nanoslabs at the resonant wavelength within the near infrared, resulting in a narrowband and sharp absorption with a peak of 0.81 through controlling the structure period, incident angle

and polarization of light. The measured responsivity spectra of these two structures exhibit the same variation with the absorptance spectra (opposite to the variation of the reflectance spectra), showing a narrowband, spectral selectivity and high responsivity photodetection in the telecommunication C-band. The measured photocurrent responsivity of these two structures show a competitive performance with respect to the previously reported Si-based NIR photodetectors. Through changing the component material and structure dimensions, these grating-based channel structures are promising for achieving photodetection in the middle infrared (MIR) and even terahertz (THz) ranges. The theoretical calculation to quantify the photocurrent response in terms of the optical and electrical properties of hot electron photodetectors can also be performed using Scales's model (for M/S architecture) or Chalabi's model (for M/I/M architecture), which are both demonstrated to match well with the experimental results. On the other hand, due to the strong field enhancement at the metal/air interface and the spectrally-selective absorption of light at the resonant wavelength, the resonant wavelength of the proposed structure exhibits a highly sensitive shift with the minute change of the refractive index (RI) of the surrounding medium, showing a potential for the application of refractive index sensing in the near infrared region.

Apart from the plasmonic structures with the excitation of SPs, the currently proposed TPs-based planar structures have also drawn much attentions. TPs or optical Tamm states exist at the metal/DBR interface. At the resonant wavelength for TPs, the electromagnetic surface wave propagating along the metal/DBR interface can be highly confined around the interface, allowing for strong absorption by the metallic film. This kind of hot electron photodetectors consist of alternating multilayers (DBR) with different refractive indexes and metal film, generating TPs at the DBR/metal interface. The biggest advantage of the TPs-based planar structure is that even though it is free of complicated nanofabrication process (electron-beam lithography, etching, lift-off, etc.), it still exhibits a large photocurrent response, such as our proposed DBR-Au film structure as shown in chapter 4. The proposed DBR-film structure consists of alternating Si/SiO_2 layers and an Au film. Due to the generation of TPs, the proposed structure achieves narrowband and spectrally selective photodetection by only using planar Si/Au architecture. By generating the grating-on-DBR

mode, we propose a grating-on-DBR structure as shown in chapter 4. The structure is likely to couple the FP resonance and TP resonance, which further enhances the generation of hot electrons in the metal and facilitate the formation of photocurrent. The calculated photocurrent responsivity of the grating-on-DBR structure is larger than most of ever reported TPs-based hot electron photodetectors till now. Through changing the pair of DBR, the component material and the grating dimensions, this grating-on-DBR structure is promising to achieve photodetection in MIR and THz ranges.

To further explore and investigate hot electron photodetection, my plan for the future work is: (1) investigating the thermodynamic loss mechanisms in hot electron photodetectors and finding strategies to achieve efficient hot electron photoconversion. (2) continuing designing new structures with novel architectures to improve the photoelectric conversion efficiency, the photocurrent responsivity and the photoresponse time. (3) designing structures with 2D materials for broadband and high responsivity photodetection, such as graphene, perovskite, MoS_2, etc.

List of publications

(1) **H. B. Xiao**, S. C. Lo, Y. H. Tai, Y. L. Ho, J. K. Clark, P. K. Wei, and J. J. Delaunay, "spectrally selective photodetection in the near-infrared with a gold grating-based structure," *Appl. Phys. Lett.* **116**, 16 (2020)

(2) **H. B. Xiao**, S. C. Lo, Y. H. Tai, J. K. Clark, Y. L. Ho, Z. C. Deng, P. K. Wei, and J. J. Delaunay, "Hot electron photodetection with spectral selectivity in the C-band using a silicon channel-separated gold grating structure," *Nano Express* **1**, 010015 (2020)

(3) **H. B. Xiao**, S. C. Lo, Y. H. Tai, Y. L. Ho, J. K. Clark, P. K. Wei, and J. J. Delaunay, "Plasmonic silicon channel-separated gold grating structure coupled surface plasmon resonance for light trapping and refractive index sensing," in preparation.

Unaffiliated to The University of Tokyo

(4) **H. B. Xiao**, F. L. Wang, Y. Wang, H. He, and W. H. Zhu, "Effect of Ultrasound on Copper Filling of High Aspect Ratio Through-Silicon Via (TSV)," *J. Electrochem. Soc.* **164**, D126-D129 (2017)

(5) **H. B. Xiao**, H. He, X. Ren, P. Zeng, and F. Wang, "Numerical modeling and experimental verification of copper electrodeposition for through silicon via (TSV) with additives," *Microelectron. Eng.* **170**, 54-58 (2017)

(6) F. Wang, **H. B. Xiao**, and H. He, "Effects of applied potential and the initial gap between electrodes on localized electrochemical deposition of micrometer copper columns," *Sci. Rep.* **6**, 26270 (2016)

(7) **H. B. Xiao**, P. Zeng, X. Ren, and F. Wang, "Three-dimensional microfabrication of copper column by localized electrochemical deposition," *17th International Conference*

on Electronic Packaging Technology (ICEPT) IEEE, 69-72 (2016) (Won outstanding Paper Award)

(8) F. Wang, X. Ren, Y. Wang, P. Zeng, Z. Zhou, **H. B. Xiao**, and W. Zhu, "Parameter analysis on the ultrasonic TSV-filling process and electrochemical characters," *J. Micromech. Microeng.* **27**, 105003 (2017)

(9) F. Wang, P. Zeng, Y. Wang, X. Ren, **H. B. Xiao**, and W. Zhu, "High-speed and high-quality TSV filling with the direct ultrasonic agitation for copper electrodeposition," *Microelectron. Eng.* **180**, 30-34 (2017)